

NUMERICAL AND EXPERIMENTAL INVESTIGATION OF WALL SHEAR STRESS  
GENERATED BY A BERNOULLI PAD

By

Anshul Singh Tomar

A DISSERTATION

Submitted to  
Michigan State University  
in partial fulfillment of the requirements  
for the degree of

Mechanical Engineering—Doctor of Philosophy

2024

## ABSTRACT

Bernoulli pads can create a significant normal force on an object without contact, which allows them to be traditionally used for non-contact pick-and-place operations in industry. In addition to the normal force, the pad produces shear forces, which can be utilized in cleaning a workpiece without contact. The motivation for the present work has been to understand the flow physics of the Bernoulli pad such that they can be employed for non-contact biofouling mitigation of ship hulls. Numerical investigations have shown that the shear stress distribution generated by the action of the Bernoulli pad on the workpiece is concentrated and results in maximum shear stress very close to the neck of the pad. The maximum value of wall shear stress is an important metric for determining the cleaning efficacy of the Bernoulli pad. We use numerical simulations over a range of parameter space to develop a relationship between the inlet fluid power and the maximum shear stress obtained on the workpiece. To increase the shear force distribution, we explore the possibility of adding mechanical power to the system in addition to the fluid power. The flow field between the Bernoulli pad and the workpiece typically involves a recirculation region and transition between laminar and turbulent flow. The maximum shear stress occurs in the vicinity of the recirculation region and to gain confidence in the numerical solver's ability to estimate these stresses accurately, experiments were conducted with a hot-film sensor.

The main contributions of this work are as follows: a direct relationship is obtained between the maximum shear stress on the workpiece and inlet fluid power using dimensional analysis. A relationship between the maximum shear stress and the inlet Reynolds number is also obtained, and implications of these scaling relationships are studied. A direct relationship between the inlet fluid power and the shear losses motivates us to explore other methods of providing power to the system with the objective of increasing shear forces and thereby improving cleaning efficacy. We numerically investigate a Bernoulli pad in which additional mechanical power is added by rotating the pad. This additional power increases both the normal and shear forces on the workpiece for the same inlet fluid power. In the context of the rotating Bernoulli pad, it is found that for a given normal attractive force, a stable equilibrium configuration can exist for two different mass flow rates, with

the higher mass flow rate resulting in a higher stiffness of the flow field. This phenomenon has not been reported in the literature. The wall shear stress distribution, obtained using numerical simulations, is validated using experiments for the first time. A constant temperature anemometer is used with a hot-film sensor and water as the working fluid; the sensor is calibrated using a fully developed channel flow. An experimental setup is designed to calibrate and later measure the wall shear stress in a Bernoulli pad assembly. The maximum wall shear stress is observed very close to the neck of the pad due to flow constriction and separation; the hot-film experiments accurately capture the magnitude of the maximum shear stress and its location. This provides us with confidence in the numerical solver, which can be used to optimize the Bernoulli pad design to improve its cleaning efficacy.

Copyright by  
ANSHUL SINGH TOMAR  
2024

Dedicated to my wife Nikita Talukdar

## ACKNOWLEDGEMENTS

I want to express my sincere gratitude to my thesis advisor, Dr. Ranjan Mukherjee, for his invaluable guidance, support, and encouragement throughout the process of completing this thesis. His expertise, patience, and unwavering commitment have been instrumental in shaping the direction of my research and helping me navigate the challenges along the way. I am deeply thankful for his insightful feedback, constructive criticism, and dedication to excellence, which have significantly enriched the quality of this work. His mentorship has enhanced my academic skills and inspired me to strive for excellence in all my endeavors. Furthermore, I am grateful to him for his mentorship beyond academia, his willingness to share their knowledge and wisdom, and for serving as a role model of integrity and professionalism. I would also like to thank Dr. Aren Hellum for his guidance and contribution to this research work. Aren was always available whenever I needed suggestions and feedback. I will always be grateful for his patience; it has greatly helped me.

I would also like to thank Dr. Ricardo M. Alvarez for his continuous support throughout this journey. I have learned a lot from him, and his insights into my research work have helped me greatly. I would also like to take this opportunity to thank my thesis committee member, Dr. Andre Benard, for providing me with valuable suggestions for shaping this thesis.

My journey as a Ph.D. student was a roller coaster ride, but it had always had a constant catalyst for pacifying me - my wife, Nikita. I can not thank you enough for trusting me and making me what I am today. I can have a good or bad day, but when I am home, you make me forget about everything with that smile. Most days, we will go out for walks, and you will listen to my work and boost my morale without even saying a word. I know you don't need this, but thank you for being my best friend and a superb life partner.

I would also like to thank my parents and sisters. Your constant support and well-being ensured that I am always motivated to perform better. Your sacrifices have inspired me in more ways than one can imagine. You guys are the best. I am blessed to have wonderful in-laws who cheered for me throughout my journey. I am thankful for my wonderful friends here: Sai, Nikhil, Vipesh, Arjun, Revanth, and Mudita. Thank you all for being wonderful listeners and kind to me. This

journey was impossible without the support I got from my lab mates - Aakash, Shaede, Sanders, and Robert.

At last, I would like to acknowledge the Office of Naval Research, ONR Grant N00014220-1-2170 for funding this research work.

## TABLE OF CONTENTS

CHAPTER 1	INTRODUCTION . . . . .	1
CHAPTER 2	RELATIONSHIP BETWEEN INLET FLUID POWER AND WALL SHEAR STRESS . . . . .	6
2.1	Introduction . . . . .	6
2.2	Methodology . . . . .	6
2.3	Scaling Analysis . . . . .	13
2.4	Results . . . . .	16
2.5	Discussion . . . . .	18
2.6	Concluding Remarks . . . . .	23
CHAPTER 3	FLOW PHYSICS OF A ROTATING BERNOULLI PAD . . . . .	24
3.1	Introduction . . . . .	24
3.2	Approach . . . . .	26
3.3	Flow physics of a rotating pad . . . . .	30
3.4	Flow physics of a rotating Bernoulli Pad . . . . .	33
3.5	Rotating Bernoulli Pad: Variation of Normal Force with Gap Height . . . . .	39
3.6	Rotating Bernoulli Pad: Energy Balance and Advantages . . . . .	45
3.7	Conclusion . . . . .	53
CHAPTER 4	WALL SHEAR MEASUREMENT: HOT-FILM ANEMOMETRY AND MODEL TESTING . . . . .	55
4.1	Introduction . . . . .	55
4.2	Background . . . . .	56
4.3	Calibration of Hot-Film Sensor . . . . .	60
4.4	Bernoulli Pad Experimental Setup . . . . .	64
4.5	Wall Shear Stress Measurement . . . . .	69
4.6	Conclusion . . . . .	75
CHAPTER 5	SUMMARY AND FUTURE WORK . . . . .	77
5.1	Summary . . . . .	77
5.2	Future Scope . . . . .	78
BIBLIOGRAPHY	. . . . .	80
APPENDIX	. . . . .	84

## CHAPTER 1

### INTRODUCTION

Bernoulli pads or Bernoulli grippers are used widely to grip objects or surfaces without physically contacting them. In its simplest implementation, this device consists of an axial jet surrounded by a surface that is parallel to the exit of the jet - see Figure 1.1. Other implementations exist, which use a simple (Brun and Melkote (2009)) or complex (Wagner et al. (2008)) center body to redirect the axial flow as it exits the jet. Because of their ability to manipulate delicate parts in a clean environment, Bernoulli pads and similar technologies (Paivanas and Hassan (1981)) see widespread use in the semiconductor industry, and a rich patent literature focused on this application has also been developed (Logue (1970), Frey (1999), and McIlwraith and Christie (2003)). Because these devices are able to exert force to grip soft and pliable workpieces, they have also been explored in medical (Erturk and Erzincanli (2020)), apparel (Fantoni et al. (2014)), and meat processing (Misimi et al. (2016)) applications.

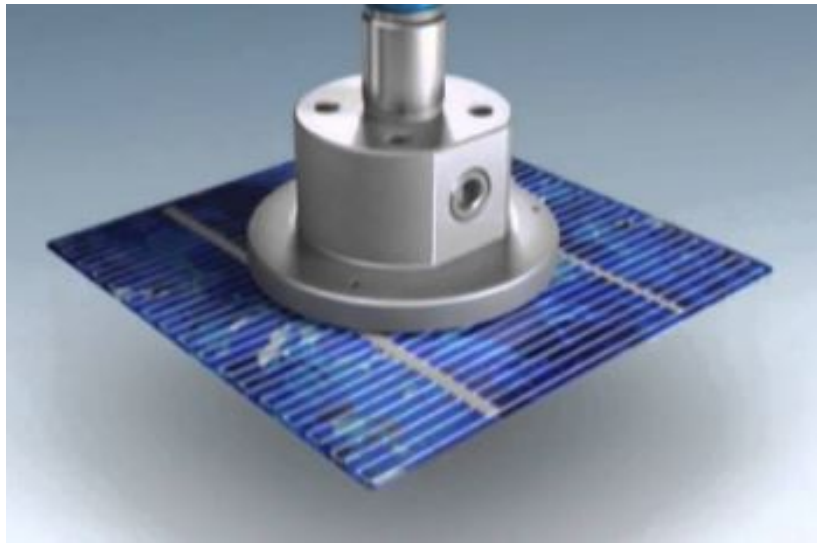


Figure 1.1 A typical Bernoulli gripper used in pick and place industries (P.C.: <https://youtu.be/phSlc8B4kFo>)

The direction and magnitude of the normal force produced by the pad depend on the distance between the pad and the opposite surface. In the limit where the pad contacts the surface, the repulsive force is equal to the product of the jet's area and feed pressure, whereas at very large

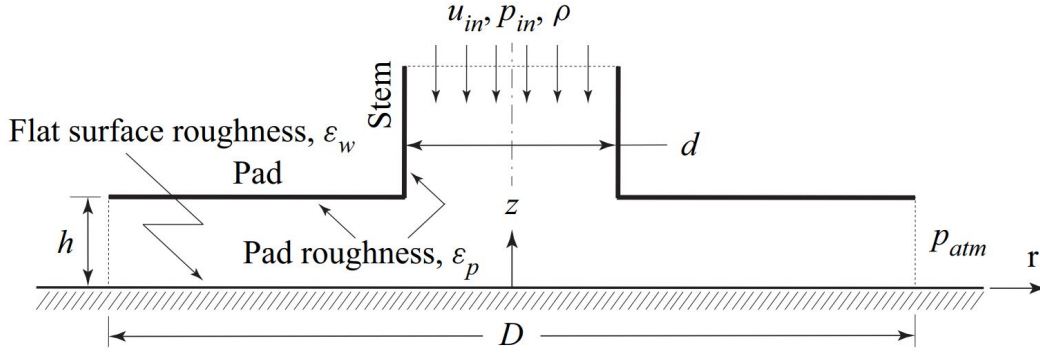


Figure 1.2 A Bernoulli pad showing the inlet and outlet flow parameters.

distances, the repulsive force scales with the jet momentum. An attractive force is produced at some intermediate distance, which can be understood, with an important caveat, in the context of the Bernoulli equation. By combining the Bernoulli equation with mass conservation, we find an expression for the local pressure for the geometry in Figure 1.2. For small values of the product  $hr$ , a net negative gage pressure results, which can produce a net attractive force integrated over the pad area. Because the force is repulsive in the limits of large and small  $h$  and attractive for intermediate values, the system has two equilibrium points, one stable and the other unstable (Li and Kagawa (2014), Kamensky et al. (2019)).

$$p(r) = p(0) - \frac{\rho}{2} \left( \frac{\pi d^2 u_{in}}{8\pi hr} \right) \quad (1.1)$$

Assuming a sufficient flow rate for the applied force, the system will operate at its stable equilibrium height  $h_{eq}$ , which dictates the distance between the pad and the opposing surface. This height is important in a variety of applications (Wagner et al. (2008), Olsson and Williams (1969)) and is also linked to the amount of fluid power required to operate the device (Kamensky et al. (2019)).

Kamensky et al. (2019) produced a scaling relationship between operating power and equilibrium height, the derivation of which indicates that work added to the system is primarily required to overcome shear at the wall. This wall shear is the reason that the inviscid analysis in (1.1) is not fully correct (Wark and Foss (1984)). For most applications, the wall shear is a by-product of the



Figure 1.3 The colonization of microorganisms, plants, algae, or animals affecting the ships life  
(Pic Credit: <https://safety4sea.com/cm-understanding-marine-biofouling-how-anti-fouling-systems-prevent-growth/>)

normal force that supports the workpiece. Although the effect of pressure distribution on delicate (Brun and Melkote (2009)) and flexible (Dini et al. (2009)) workpieces has been examined, shear is less well-studied. Typically, deformation or destruction of the opposing surface due to shear forces is not a substantial concern because the maximum normal stresses are much larger.

The present work is motivated by a grooming application in which a Bernoulli pad is moved around the submerged hull of a marine vessel to remove biofouling. In this application, the pad keeps itself close to the surface of the vessel using the attractive normal forces generated and simultaneously uses the wall shear forces for biofouling mitigation (Kamensky et al. (2020)). This method of cleaning is consistent with the operation of commercially available fouling-release coatings (Hu et al. (2020)), which use boundary-layer shear while the vessel is underway to slough fouling organisms. Biofouling colonization on a ship's hull is most problematic in port, where these forces are not present- see Figure 1.3. For the grooming device to keep the vessel clean, it is necessary for the local shear stress imposed at the hull to be large enough to dislodge fouling organisms, a value which depends on the organism and settling time (Menesses et al. (2017)). Therefore, the maximum shear stress created by the flow field is a parameter of interest for this application.

This work aims to understand the flow physics involving a Bernoulli pad and employ them as

a non-contact shear-based grooming tool. A power law relation between the power available at the inlet and the maximum shear stress produced on the workpiece is obtained. This relation will enable us to explore the other ways of providing inlet power to the Bernoulli pad. The study aims to increase the wall shear stress value for better grooming efficacy of biofouling mitigation and increase normal suction force for better adhering capacity. The CFD simulations in the present work are carried out using commercial solvers such as ANSYS Fluent and COMSOL. The flow domain is relatively simple, but the flow field involves a circulation region and a transition from a laminar to a turbulence regime. Hence, to accurately resolve the flow field, the numerical solver used for the simulations requires validation from experiments. We have designed an experimental setup to calibrate the hot-film sensor in the present work. Further, we have designed a setup that uses a Bernoulli pad and proximally kept workpiece to measure the wall shear stress using the calibrated sensor.

In chapter 2, we simulate a large number of Bernoulli pad geometries using water as the working fluid. The methods used in these simulations are validated by a Particle Tracking Velocimetry (PTV) experiment performed on one of the geometries. These simulations indicate that the maximum shear stress increases as the equilibrium height decreases and the inlet fluid power increases. We present a scaling analysis to obtain a power-law relation for the inlet fluid power based on the maximum shear stress and equilibrium height. The CFD data also indicate a power-law relationship between the maximum shear stress and the inlet Reynolds number. The empirical form found for the relationship between maximum shear stress and inlet power in Appendix also indicates a direct relationship between the inlet Reynolds number and the length scale which characterizes the dissipation of power by wall shear.

In chapter 3, we provide rotational motion to the Bernoulli pad. The solver used for the numerical simulation is validated against the Particle Tracking Velocimetry (PTV) experiment performed for one of the geometries and the angular speed of zero rad/s. The working fluid is water for all the simulations. The effect of rotation on the computational domain is presented with and without inlet fluid power. The effect of rotation on the pressure profile on the workpiece and force

variation with gap height is discussed. Later, work analysis is carried out, and the work available at the inlet, outlet, and mechanical work is tabulated. The effect of angular speed on the force and shear stress on the workpiece is also presented.

In chapter 4, hot-film experiments are discussed to measure the wall shear stress obtained on the workpiece. We have used a fully developed flow through a channel to calibrate the hot-film probe. The design of the channel for achieving an early, fully developed flow is presented. Later, the sensor is mounted on the channel based on the location of the fully developed regime. The readings from the pressure transducers connected with the channel and hot-film probes are used to obtain the calibration coefficient.

In chapter 5, we have summarized the findings of the present work, and a brief discussion is presented about the future work to be carried out. The future scope involves studies with cavitation effects, rigid curved Bernoulli pads and experiments for rotating Bernoulli pad.

## CHAPTER 2

### RELATIONSHIP BETWEEN INLET FLUID POWER AND WALL SHEAR STRESS

#### 2.1 Introduction

A large part of this chapter was used to publish an article in the Flow journal Tomar et al. (2022). The motivation for the present work is to employ the Bernoulli pad for non-contact biofouling mitigation on the ship hulls. The axial flow from the inlet of the Bernoulli pad strikes the workpiece and passes radially in the outward direction through a constricted passage. The gap between the pad and the workpiece is very small, and due to the sharp curvature of the pad, a recirculation region is formed very close to the neck of the pad. The velocity gradients under the recirculation regions are very high, and therefore, below the belly of the recirculation region, the maximum value of wall shear stress is observed.

The maximum value of wall shear stress is an essential parameter for the application of non-contact biofouling mitigation of ship hulls. Hence, the focus of this work revolves around the quantification of wall shear stress. The wall shear stress generated on the workpiece depends upon the gap height, pad dimensions, and the inlet fluid power provided to the system. The inlet fluid power is easily measurable for real-life problems. Therefore, in this chapter, we have used CFD simulations to obtain a power-law relationship between the inlet fluid power and the maximum shear stress generated on the workpiece.

#### 2.2 Methodology

##### 2.2.1 Computational domain

The Bernoulli pad is axially symmetric, and therefore, the fluid dynamics is investigated using a two-dimensional axisymmetric computational model; this significantly reduces the computational time. The computational domain is defined by the inner diameter  $d$ , outer diameter  $D$ , and gap height  $h$  - see Figure 1.2. An axial flow is provided at the inlet; assuming incompressibility, the flow parameters include the inlet velocity  $u_{in}$ , the inlet pressure  $p_{in}$ , and fluid density  $\rho$ . After impinging the wall, the fluid flows radially outward through the gap; the pressure at the outlet is atmospheric,

$p_{atm}$ . The surface roughness of the pad and the wall are  $\varepsilon_p$  and  $\varepsilon_w$ , respectively, and no-slip boundary conditions are imposed on both surfaces. Following the work by Kamensky Kamensky et al. (2019), a four equation-based transition-SST model is used for turbulence modeling. As discussed therein, there exists a stable equilibrium gap height  $h_{eq}$ , where the net normal force on the wall is zero. In this study, the same model is used to determine the inlet velocities that correspond to different configurations of stable equilibrium gap,  $h_{eq}$ . It should be noted that although  $h_{eq}$  is an imposed condition for the CFD model, in a physical system,  $h_{eq}$  is the result of the imposed flow conditions and pad geometry. In this study, we investigate the relationship between inlet fluid power and maximum wall shear stress at  $h_{eq}$ .

### 2.2.2 Equilibrium height

The constricted flow of the fluid in the gap introduces a net normal force  $F$  on the wall; the magnitude and direction of this force depend on the gap height  $h$ . As discussed by Kamensky et al. Kamensky et al. (2019), the pad and the wall repel each other ( $F$  is positive) when the gap is small

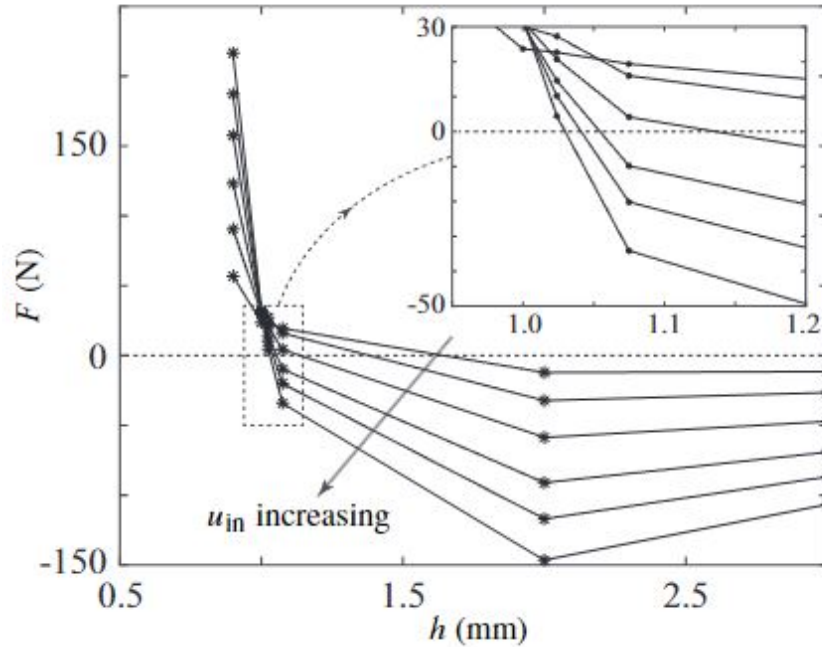


Figure 2.1 Variation of force  $F$  with gap height  $h$  for a Bernoulli pad with  $d = 31.75$  mm and  $D = 300$  mm for six different inlet velocities  $u_{in} = \{1.0, 1.5, 2.0, 2.5, 2.847, 3.187\}$  m/s.



Figure 2.2 (a) Experimental setup for PTV and (b) CAD model of Bernoulli pad (Kamensky, Kamensky (2020))

and attract ( $F$  is negative) when the gap is increased beyond a certain value. There exists a critical gap height for which the net normal force on the wall is zero ( $F = 0$ ); this gap height is referred to as the equilibrium height  $h_{eq}$ . The plot in Figure 2.1 shows the variation of  $F$  with  $h$  for six different values of inlet velocity  $u_{in}$  for a specific Bernoulli pad. It is evident that  $F$  is positive for small values of  $h$  and becomes negative when  $h$  is increased; for each inlet velocity, it is possible to find a value of  $h = h_{eq}$  where the net normal force is equal to zero.

In this chapter, we investigate the relationship between inlet fluid power and maximum wall shear stress; this relationship will be investigated at the stable equilibrium point where  $h = h_{eq}$ . For a given Bernoulli pad, the value of  $h_{eq}$  depends completely on the inlet velocity. To reduce the computational time associated with continuous re-meshing of the computational domain due to change in  $h$ , we keep  $h$  constant and vary  $u_{in}$  till we reach the equilibrium point, *i.e.*,  $F = 0$ . This allows us to determine the inlet velocity for a desired  $h_{eq}$ .

### 2.2.3 Validation with PTV

The CFD simulations were carried out using an element size of  $6 \times 10^{-5}$  m; this resulted in 61,302 elements and a maximum  $y^+$  value of 7.5. A smaller element size of  $5 \times 10^{-5}$  m resulted in 75,315 elements but the percentage change in the maximum wall normal and maximum wall shear stresses (0.11% and 0.87%, respectively) did not justify the additional computational cost.

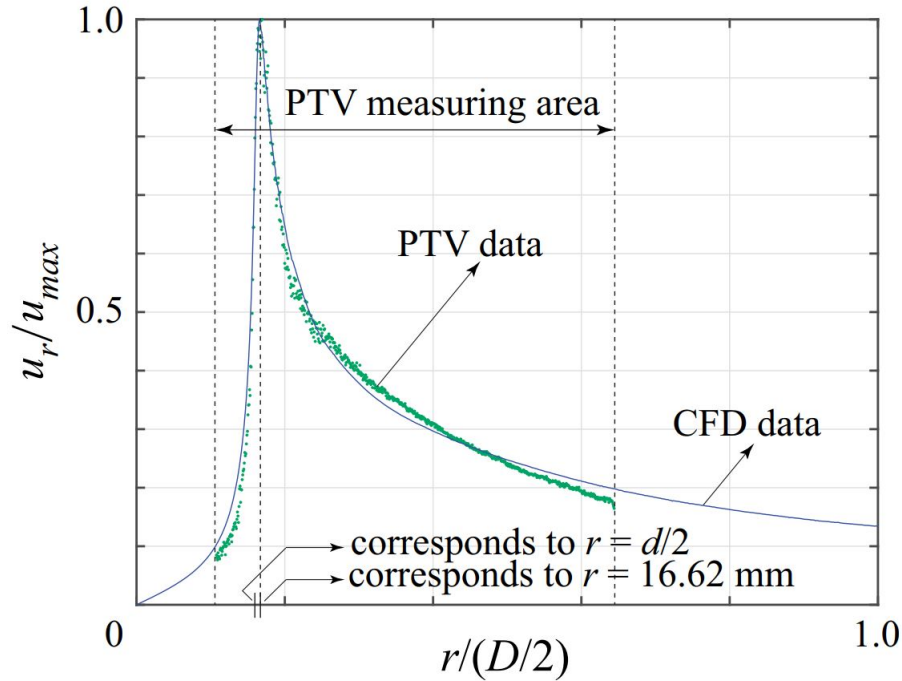


Figure 2.3 Comparison of PTV and CFD data: plot of nondimensional radial velocity at  $z = h/2$  with respect to nondimensional radial position

To gain confidence in our CFD results, we compare them with experimental results obtained using 3D Particle Tracking Velocimetry (PTV). The experimental setup consists of four ultra high-speed cameras (Phantom v2512) placed in an arc-like pattern; these cameras focus on a volume of rectangular cross-section between the pad and tank wall. A dual-head laser is placed between the four cameras; it is used to illuminate the particles in the flow - see Figure 2.2 (a).

A CAD model of the Bernoulli pad showing the volume in which the particles are imaged is shown in Figure 2.2 (b). The camera view is masked to this region to reduce the disk space and memory requirement. The region includes a portion of axial flow through the stem and radial flow extending beyond half of the outer radius of the Bernoulli pad. Further details of the experimental setup can be found in Kamensky Kamensky (2020)).

The PTV data is used to determine the ensemble-averaged velocity on an  $r$ - $z$  plane of the flow domain (refer to Figure 1.2) and is compared with CFD results in Figure 2.3 for  $z = h/2$ : The radial velocity was nondimensionalized with respect to its maximum value  $u_{max}$ , and the radial position

was nondimensionalized with respect to the outer radius of the pad. There is a good agreement between the velocity profiles obtained using CFD simulations and PTV experiments; the location of the maximum peak is also observed at the same value of  $r$  ( $r = 16.62$  mm), which is very near to the entrance of the fluid in the radial direction ( $r = d/2 = 15.875$  mm). This provides us with confidence to proceed with the analysis of CFD data.

## 2.2.4 CFD data

The nominal parameter values used for the CFD simulations are

$$d = 31.75 \text{ mm}, \quad D = 200 \text{ mm}, \quad h_{eq} = 1.5 \text{ mm}, \quad \varepsilon_p = \varepsilon_w = 0.04 \text{ mm}$$

CFD simulations are carried out for a Bernoulli pad with the nominal dimensions using ANSYS Fluent. The radial velocity and total pressure contours obtained are shown in Figure 2.4 and 2.5. The gap between the pad and the workpiece is very small; therefore, to provide a better view of the contours, the contour plots in Figure 2.4 and 2.5 are presented on a magnified and smaller portion of the complete computational domain. The radial velocity very close to the neck of the pad is

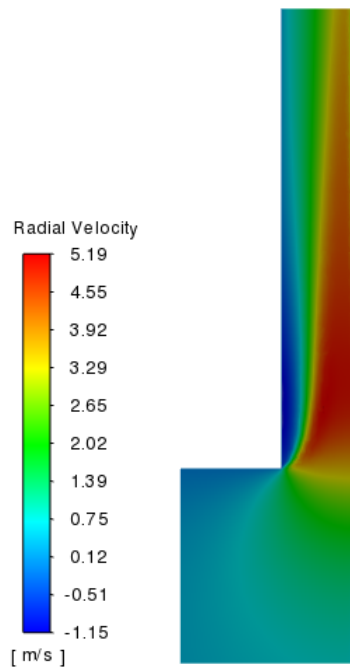


Figure 2.4 Radial velocity contour for the nominal pad

negative, which represents the recirculation region, and the maximum velocity is observed below the recirculation bubble.

The total pressure is maximum at the inlet due to the inlet fluid power provided to the system, which, after striking the workpiece, reduces in the impinging region. After the flow enters the gap between the pad and the workpiece, the flow area increases, and therefore, the flow velocity reduces. This, in turn, implies that the pressure magnitude will increase in the gap. The pressure boundary condition at the outlet is atmospheric, which implies that the pressure at the neck of the workpiece is negative. The negative pressure at the neck of the workpiece is responsible for the suction force generation on the workpiece.

A total of 45 design points were generated using three values of  $d$  (0.5, 0.707, and 1 times the nominal value), five different values of  $D$  (0.5, 0.707, 1, 1.414 and 2 times the nominal value) and three different values of  $h_{eq} = \{1.4, 1.5, 1.6\}$  mm. The value of  $\varepsilon_p$  and  $\varepsilon_w$  used is consistent with Material. A brief discussion of the hydraulic roughness can be found in the Discussion section.

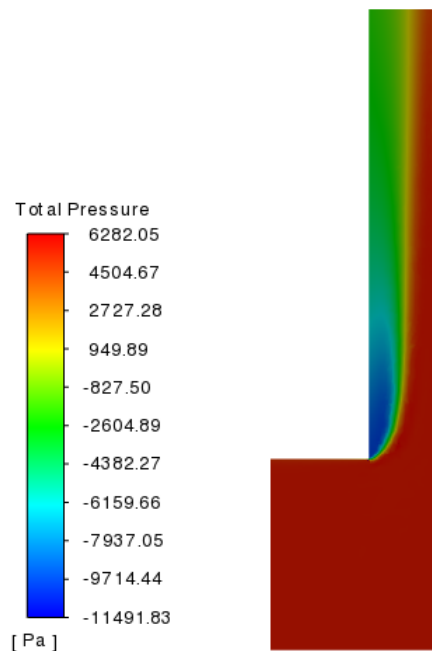


Figure 2.5 Total pressure contour for the nominal pad

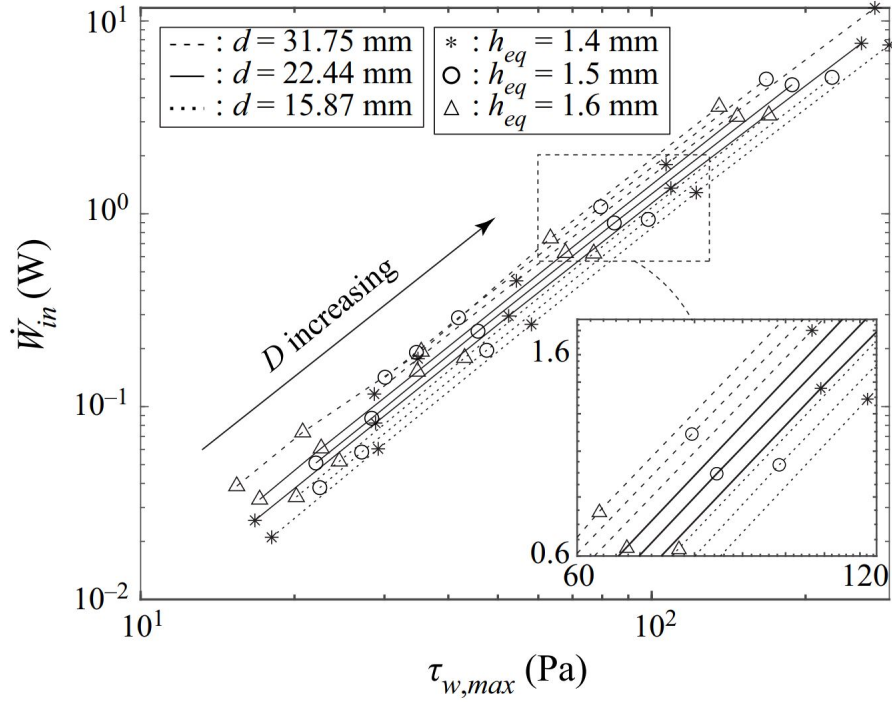


Figure 2.6 Plot of inlet fluid power versus maximum wall shear stress

The inlet fluid power  $\dot{W}_{in}$ , defined in Kamensky et al. Kamensky et al. (2019) as

$$\dot{W}_{in} = 2\pi \int_0^{d/2} \left[ \frac{1}{2}\rho [U(r)]^2 + p(r) \right] U(r) r dr$$

and the maximum shear stress on the wall  $\tau_{w,max}$  are obtained for all these design points; they are plotted in Figure 2.6 in log-log scale. The 45 data points are grouped into nine sets of five points. Each set of five points is joined by straight line segments and corresponds to the five different values of  $D$  for specific values of  $d$  and  $h_{eq}$ ; the direction in which  $D$  increases is shown in the figure. The data points shown with \*, o, and  $\Delta$  symbols correspond to specific values of  $h_{eq}$ , shown in the figure.

For clarity, a magnified image of a portion of the plot is shown inset; the top three lines (dashed) correspond to  $d = 31.75$  mm, the middle three lines (solid) correspond to  $d = 31.75 \times 0.707 = 22.44$  mm, and the bottom three lines (dotted) correspond to  $d = 31.75 \times 0.5 = 15.875$  mm. It is evident that maximum wall shear stress varies linearly with inlet fluid power for a given value of  $d$  and  $h_{eq}$ ; furthermore, as expected, the maximum wall shear stress increases as  $h_{eq}$  decreases for the same

level of inlet power.

### 2.3 Scaling Analysis

In a physical system like the one considered in this study, the gap between the pad and wall is not imposed. Rather, the system reaches the equilibrium gap  $h_{eq}$  as the result of the imposed pad geometry (inner and outer diameters,  $d$  and  $D$  respectively), and inlet flow conditions (inlet velocity  $u_{in}$ , characteristic length  $d$ , and fluid physical properties). Also as a result of those imposed conditions, the flow will exhibit a maximum wall-shear  $\tau_{w,max}$  somewhere along the radius of the gap, and consequently will demand a certain amount of power  $\dot{W}_{in}$  to sustain the inlet flow conditions.

With this in mind, the independent variables governing the flow through a Bernoulli pad in equilibrium conditions are the geometric parameters  $d$  and  $D$  and the inlet flow parameters  $\rho$ ,  $\mu$  and  $u_{in}$ , because those are the only variables controlled by the experimentalist; and in consequence  $\dot{W}_{in}$ ,  $h_{eq}$ , and  $\tau_{w,max}$  are the dependent variables because they result from the imposed geometric conditions and inlet flow conditions. Therefore, the dependent variables can be expressed as a function of the independent variables as follows:

$$\dot{W}_{in} = f(\mu, u_{in}, D, d, \rho), \quad h_{eq} = g(\mu, u_{in}, D, d, \rho), \quad \tau_{w,max} = h(\mu, u_{in}, D, d, \rho) \quad (2.1)$$

After choosing the inlet diameter  $d$ , dynamic viscosity  $\mu$ , and inlet velocity  $u_{in}$  as repeating variables, a dimensional analysis over each one of the above functional forms provide the following set of dimensionless parameters:

$$\tilde{W}_{in} = \frac{\dot{W}_{in}}{\mu u_{in}^2 d}, \quad h^* = \frac{h_{eq}}{d}, \quad \tilde{\tau}_{w,max} = \frac{\tau_{w,max} d}{\mu u_{in}}, \quad D^* = \frac{D}{d}, \quad Re_{in} = \frac{\rho u_{in} d}{\mu} \quad (2.2)$$

The nondimensional maximum shear stress  $\tilde{\tau}_{w,max}$  is the ratio between the maximum wall-shear stress and a combination of parameters that together also have the dimension of stress:  $\mu u_{in}/d$ . This combination of parameters is however representative of a shear scale in the inlet pipe rather

than in the pad gap. A more appropriate shear scaling would be of the form  $\mu u_c/h_{eq}$ , where  $u_c$  is the characteristic velocity at the inlet of the pad gap (since the maximum shear occurs in this region), and can be determined from the volumetric flow rate  $\dot{V}$  and the inlet cross-section of the pad gap as follows:

$$\dot{V} \triangleq \left(\frac{\pi}{4}d^2\right)u_{in} \quad \Rightarrow \quad u_c = \frac{\dot{V}}{\pi dh_{eq}} = \frac{1}{4} \cdot \frac{u_{in} d}{h_{eq}} \quad (2.3)$$

Hence, the shear scaling for the inlet region of the pad gap is:

$$\mu \frac{u_c}{h_{eq}} = \frac{1}{4} \cdot \frac{\mu u_{in} d}{h_{eq}^2} \sim \frac{\mu u_{in} d}{h_{eq}^2} \quad (2.4)$$

The factor 1/4 can be ignored because it will be ultimately absorbed by a fitting coefficient. The nondimensional shear stress  $\tilde{\tau}_{w,max}$  can now be manipulated based on this shear scaling as follows:

$$\tilde{\tau}_{w,max} = \frac{\tau_{w,max} d}{\mu u_{in}} = \frac{\tau_{w,max} d}{\mu u_{in} (d/h_{eq}^2)} \cdot \frac{d}{h_{eq}^2} = \frac{\tau_{w,max}}{\mu u_{in} (d/h_{eq}^2)} \cdot [h^*]^{-2} \quad (2.5)$$

Equation 2.5 shows that  $\tilde{\tau}_{w,max}$  is the combination of a new expression for dimensionless maximum shear and  $h^*$ , but  $h^*$  is one of the dependent nondimensional variables. To eliminate this redundancy,  $\tilde{\tau}_{w,max}$  is replaced by  $\tau_{w,max}^*$ , which is defined as follows:

$$\tau_{w,max}^* = \frac{\tau_{w,max}}{\mu u_{in} (d/h_{eq}^2)} \quad (2.6)$$

The set of dimensionless parameters in (2.2) can now be modified to:

$$\tilde{W}_{in} = \frac{\dot{W}_{in}}{\mu u_{in}^2 d}, \quad h^* = \frac{h_{eq}}{d}, \quad \tau_{w,max}^* = \frac{\tau_{w,max}}{\mu u_{in} (d/h_{eq}^2)}, \quad D^* = \frac{D}{d}, \quad Re_{in} = \frac{\rho u_{in} d}{\mu} \quad (2.7)$$

This set of parameters reduces the physical system to three dimensionless functions of the form:

$$\tilde{W}_{in} = \Phi(D^*, Re_{in}), \quad h^* = \Gamma(D^*, Re_{in}), \quad \tau_{w,max}^* = \Psi(D^*, Re_{in}) \quad (2.8)$$

The dimensionless system described by (2.8) has two independent variables ( $D^*$  and  $Re_{in}$ ) as opposed to the five independent variables ( $\mu, u_{in}, D, d, \rho$ ) of the dimensional system in (2.1). While there are no analytical solutions available to determine the exact form of the relationships in (2.8), it is possible to use regression analysis to determine how the independent variables predict the dependent variables. Figure 2.6 suggests that the inlet power  $\tilde{W}_{in}$  is linearly related to the maximum shear stress  $\tau_{w,max}$  in a log-log space. This suggests that the relationships in (2.8) are also linear in a log-log space:

$$\ln \tilde{W}_{in} = C_{11} \ln D^* + C_{12} \ln Re_{in} + C_{13} \quad (2.9a)$$

$$\ln h^* = C_{21} \ln D^* + C_{22} \ln Re_{in} + C_{23} \quad (2.9b)$$

$$\ln \tau_{w,max}^* = C_{31} \ln D^* + C_{32} \ln Re_{in} + C_{33} \quad (2.9c)$$

Equations (2.9a), (2.9b) and (2.9c) can be used to eliminate  $D^*$  and  $Re_{in}$  and obtain the relationship between the dependent variables:

$$\ln \tilde{W}_{in} = \kappa_1 \ln h^* + \kappa_2 \ln \tau_{w,max}^* + \kappa_3 \quad (2.10)$$

where the coefficients  $\kappa_1$ ,  $\kappa_2$  and  $\kappa_3$  can be obtained using the relations

$$\kappa_1 = \frac{C_{12}C_{31} - C_{11}C_{32}}{C_{22}C_{31} - C_{21}C_{32}} \quad (2.11a)$$

$$\kappa_2 = \frac{C_{11}C_{22} - C_{12}C_{21}}{C_{22}C_{31} - C_{21}C_{32}} \quad (2.11b)$$

$$\kappa_3 = \frac{C_{13}C_{22}C_{31} - C_{12}C_{23}C_{31} - C_{13}C_{21}C_{32} + C_{11}C_{23}C_{32} + C_{12}C_{21}C_{33} - C_{11}C_{22}C_{33}}{C_{22}C_{31} - C_{21}C_{32}} \quad (2.11c)$$

If the assumption of linearity in log-log space is true, the linear model in (2.10) can also be used for a *direct fit* to the data, and the resulting values of the coefficients  $\kappa_i$ ,  $i = 1, 2, 3$ , should be consistent with the values determined from equations (2.11a), (2.11b) and (2.11c). This latter approach can be viewed as the *indirect fit*.

## 2.4 Results

A direct fit of the linear model in (2.10) to the CFD data results in the following values of the coefficients:

$$\begin{bmatrix} \kappa_1 & \kappa_2 & \kappa_3 \end{bmatrix} = \begin{bmatrix} -1.9683 & 2.3416 & 0.1115 \end{bmatrix} \quad (2.12)$$

These coefficient values can be substituted in (2.10) to obtain the following power-law expression:

$$\tilde{W}_{in} = 1.1180 [\tau_{w,max}^*]^{2.3416} [h^*]^{-1.9683} \quad (2.13)$$

The power-law obtained in (2.13) collapses the data on a straight line in a log-log plane - this is shown in Figure 2.8.

By fitting equations (2.9a), (2.9b) and (2.9c) to the CFD data, we get the following results for the matrix of coefficients  $\mathbb{C} = [C_{ij}]$ ,  $i, j = 1, 2, 3$ ; the coefficients can then be computed indirectly as follows:

$$\mathbb{C} = \begin{bmatrix} -1.4703 & 2.1924 & -5.9854 \\ 0.8564 & -0.7021 & 1.9268 \\ 0.0867 & 0.3477 & -0.9874 \end{bmatrix} \Rightarrow \begin{bmatrix} \kappa_1 & \kappa_2 & \kappa_3 \end{bmatrix} = \begin{bmatrix} -1.9554 & 2.3568 & 0.1094 \end{bmatrix} \quad (2.14)$$

A comparison of the results in (2.12) and (2.13), obtained through direct and indirect fit of the data, indicates that  $\kappa_1$  and  $\kappa_2$  differ by 0.65%, the results for  $\kappa_3$  differ by 1.9%. A goodness-of-fit analysis of the direct fit was conducted via calculation of the relation coefficient and an Anderson-Darling normality test (Stephens, Stephens (1974); D'Agostino et al., D'Agostino and Stephens (1986)).

The direct fit exhibits a relation coefficient of  $R^2 = 0.9951$ , which suggests an adequate goodness-of-fit. But the Anderson-Darling normality test (Stephens, Stephens (1974); D'Agostino et al., D'Agostino and Stephens (1986)) is a stronger descriptor because it determines if the error between the model and the data is random and normally distributed. If the model fails the test, it indicates that the model is likely excluding higher-order terms. The null hypothesis,  $H_0$ , states that if the data comes from a normal distribution. To test  $H_0$ , one needs the standardized residuals of the experimental measurements  $\varepsilon_i$ . These are the differences between the computed (using

the coefficients obtained with the direct fit) and experimental values of  $\ln \tilde{W}$ , normalized by their unbiased standard deviation:

$$\varepsilon_i = \frac{\ln(\tilde{W}_i) - [\kappa_1 \ln(h_i^*) + \kappa_2 \ln(\tau_i^*) + \kappa_3]}{\sqrt{\frac{\sum_{j=1}^N \left\{ \ln(\tilde{W}_j) - [\kappa_1 \ln(h_j^*) + \kappa_2 \ln(\tau_j^*) + \kappa_3] \right\}^2}{N-1}}} \quad (2.15)$$

where  $N = 45$  is the number of CFD data points. The following test statistic is used to assess  $H_0$ :

$$A^2 = -N - \sum_{i=1}^N \frac{2i-1}{N} \left\{ \ln F(\varepsilon_i) + \ln [1 - F(\varepsilon_{N+1-i})] \right\} \quad (2.16)$$

where  $F(\varepsilon_i)$  is the Empirical Cumulative Distribution Function (ECDF) and is defined as:

$$F(\varepsilon_i) = \sum_{\varepsilon_i \leq \varepsilon} p(\varepsilon_i) \quad (2.17)$$

Equation (2.17) will be used in equation (2.16) to calculate  $A^2$ , which will provide a quantitative test of  $H_0$ . Considering a significance level of  $\alpha = 0.05$ ,  $A^2$  has a critical value of 0.7385 (D'Agostino et al., 1986), which means that  $H_0$  should be rejected if  $A^2 > 0.7385$  when calculated with the experimental data. For the current data set,  $A^2 = 0.3352 < 0.7385$ , showing that the standardized error follows a normal distribution. Hence, the linear model in (2.10) is adequate to describe the data. A graphical verification of this result is provided in Figure 2.7 where the ECDF is plotted together with the Normal Cumulative Distribution Function (NCDF), which is defined as:

$$F(\varepsilon) = \frac{1}{\sigma\sqrt{2\pi}} \int_{-\infty}^{\varepsilon} e^{-\frac{1}{2}\eta^2} d\eta \quad (2.18)$$

In the study by Kamensky et al. Kamensky et al. (2019),  $\dot{W}_{in}$  was non-dimensionalized as follows:

$$\dot{W}_{in}^* = \frac{\dot{W}_{in}}{\mu u_{in}^2 D(D/d)} \quad (2.19)$$

To put the current results in context with that study,  $\tilde{W}_{in}$  can be shown to be equal to  $\dot{W}_{in}^* D^{*2}$ .

Therefore, we get from (2.13)

$$\dot{W}_{in}^* = 1.1180 [\tau_{w,max}^*]^{2.3416} [h^*]^{-1.9683} [D^*]^{-2} \quad (2.20)$$

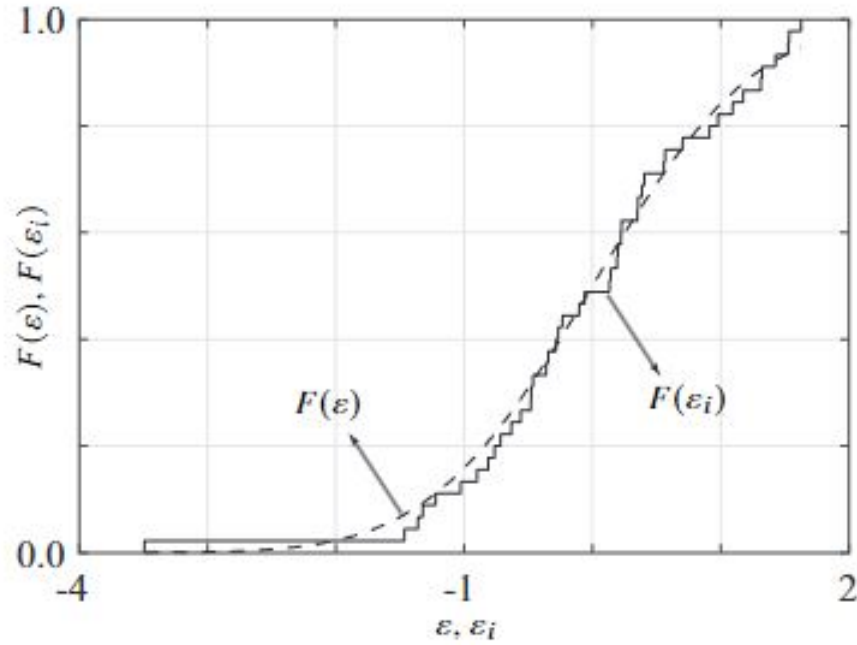


Figure 2.7 Plot showing the ECDF  $\varepsilon_i$  and the NCDF  $\varepsilon$

Based on theoretical grounds, Kamensky et al. Kamensky et al. (2019) proposed a proportionality of the form:  $\dot{W}_{in}^* \propto [h^*]^{-3}$ , which was near to the scaling observed in that work. But equation (2.20) suggests a proportionality closer to:  $\dot{W}_{in}^* \propto [h^*]^{-2}$ . These results are different because they describe different phenomena. While the former is based on the global effect of inlet fluid power on equilibrium height, the latter focuses on the local effects (where the shear stress is maximum) that relate fluid power with maximum shear stress and equilibrium height.

## 2.5 Discussion

### 2.5.1 Relationship between maximum shear stress and inlet Reynolds number

The location of the maximum shear stress is just beyond the location of the corner,  $r \approx d/2$ ; this short development length indicates a laminar boundary layer over the range of flow speeds examined here. The shear stress for a large number of laminar flows takes the form  $\tau \propto \rho U^2 Re^n \Lambda$ , where  $U$  is the flow velocity and  $\Lambda$  is a flow-dependent length scale. The value  $n = -1/2$  has been found for pure boundary layers with zero and non-zero pressure gradients (White White (1974)). This value of  $n$  was also found for the developed portion of the flow under a Bernoulli pad by (Guo

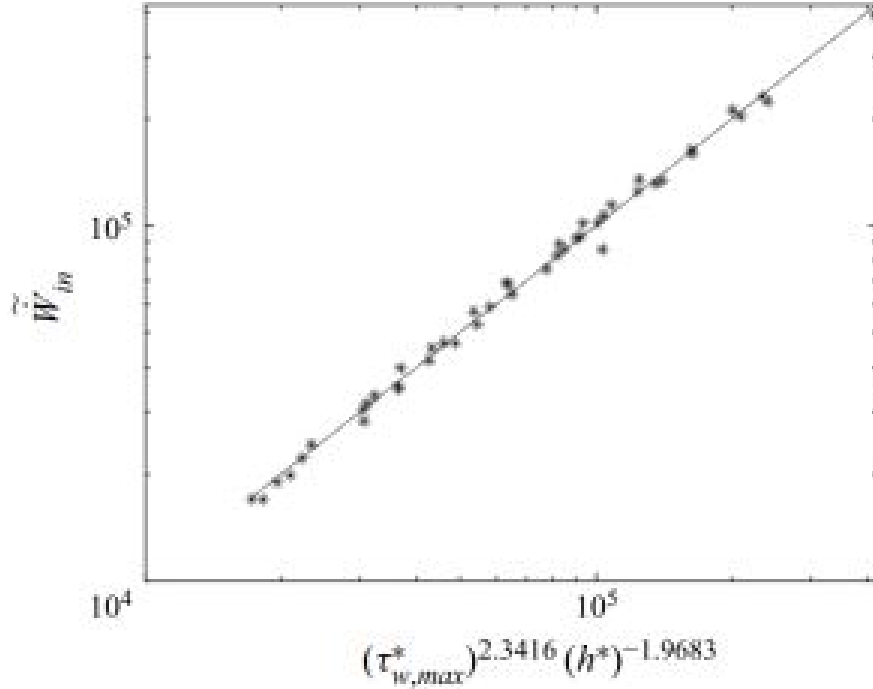


Figure 2.8 Plot showing CFD data collapsing on a straight line corresponding to the power-law in (2.13)

et al. Guo et al. (2017)). The same is true for the maximum wall shear produced by both the planar and axisymmetric wall jet, which is an unconfined analog of the developing region of the Bernoulli pad flow (Phares et al. Phares et al. (2000)).

The latter work uses laminar boundary layer theory to yield (in our nomenclature) the expression  $\tau_{w,max} \propto \rho u_{in}^2 Re_{in}^n [h^*]^{-2}$  for the maximum shear stress. The use of the gap height arises in the wall jet because of the development of the shear layer at the edge of the jet. Using our scaling relationships, this expression predicts that

$$\tau_{w,max}^* = \frac{\tau_{w,max}}{\mu u_{in} d / h_{eq}^2} \propto \frac{\rho u_{in}^2}{\mu u_{in} d / h_{eq}^2} Re_{in}^n [h^*]^{-2} = \left( \frac{\rho u_{in} d}{\mu} \right) \left( \frac{h_{eq}^2}{d^2} \right) Re_{in}^n [h^*]^{-2} = Re_{in}^{n+1}$$

$$\Rightarrow \tau_{w,max}^* \propto Re_{in}^{n+1}$$

(2.21)

that is, the non-dimensional shear stress is not dependent on any length scale other than the one appearing in the Reynolds number. We have found this to be the case (see Figure 2.9), where the

value  $n + 1 = 0.42$ , or  $n = -0.58$ , is broadly in line with the findings for other flow fields. We can write equation (2.13) as a proportionality in terms of  $Re_{in}$  and  $h^*$

$$\tilde{W}_{in} \propto [Re_{in}^{0.42}]^{2.3416} [h^*]^{-1.9683} = [Re_{in}]^{0.98} [h^*]^{-1.9683} \quad (2.22)$$

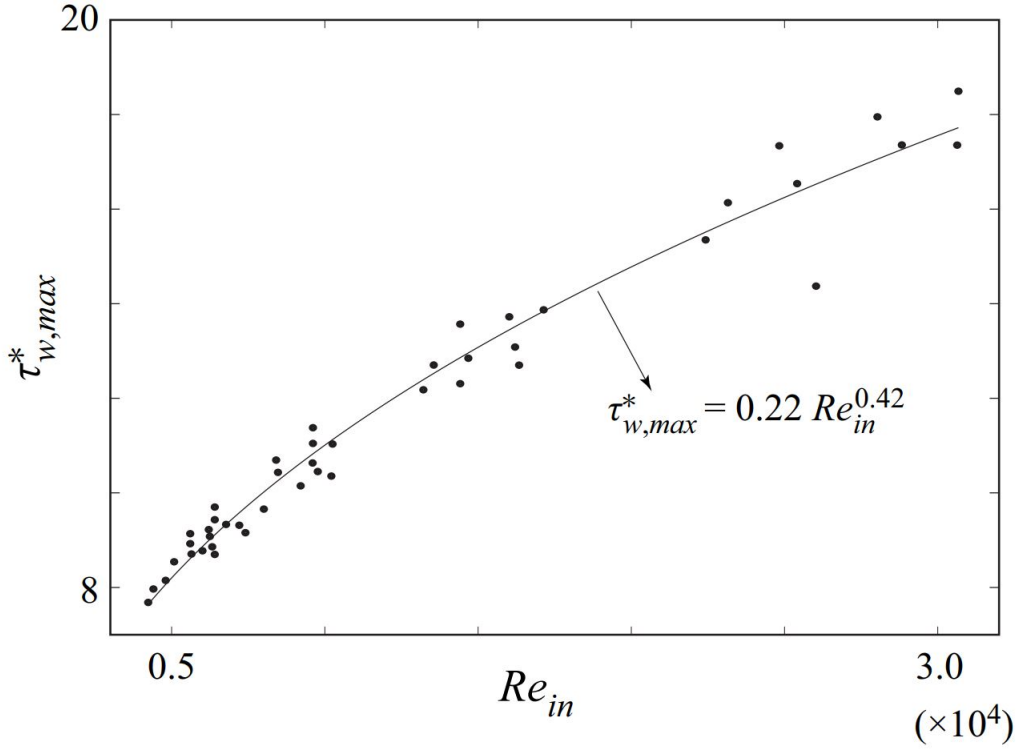


Figure 2.9 Best fit of CFD data showing power law relationship between  $\tau_{w,max}^*$  and  $Re_{in}$

The exponents which appear in Eq.(2.22) are enticingly near to round numbers but we have not been able to predict them using analytical methods. This statement also holds for expressions presented in the following section. We therefore present these relationships as implications of the data rather than derivations.

### 2.5.2 Implications of the observed scaling relationship

We can write the power  $\dot{W}_{in}$  required to operate the pad in terms of the shear stress

$$\dot{W}_{in} \propto \int_0^{2\pi} \int_0^{D/2} \tau_w(r) U(r) r dr d\theta \propto \int_0^{r_w} \tau_{w,max} U(r) r dr \quad (2.23)$$

where  $r_w$  is a radial location which characterizes an area over which we have to integrate the shear stress, and  $U(r)$  is the mean radial component of the velocity in the gap. There are two critical assumptions being made. The first assumption is that the power required to operate the system is well-characterized by the integral of the wall shear over the entire pad area; this is consistent with a low fraction of the inlet power being used to provide kinetic energy to the fluid (Kamensky Kamensky et al. (2019)). The second assumption is that the integral of the wall shear over the entire pad area can be characterized using the maximum shear stress, integrated over a much smaller area. We justify this partially on the basis of the mean radial velocity  $U(r) \propto r^{-1}$ . Because  $\tau_w(r) \propto [U(r)]^2$ ,  $\tau_w(r) U(r)r \propto r^{-2}$ , and therefore most of the power used to overcome wall shear is expended at small  $r$ . This assumption is further justified by the observed empirical form, in which the outer diameter  $D$  does not explicitly appear. We now manipulate the integrand, using the result from mass conservation:

$$U(r) \propto \frac{u_{in}d}{h^*r} \quad \Rightarrow \quad \tau_{w,max} U(r)r \propto \tau_{w,max}^* \left( \frac{\mu u_{in}}{d[h^*]^2} \right) \left( \frac{u_{in}d}{h^*r} \right) r \propto \mu u_{in}^2 \tau_{w,max}^* [h^*]^{-3}$$

Placing this form into equation (2.23) and making the result non-dimensional, yields

$$\dot{W}_{in} \propto \int_0^{r_w} \mu u_{in}^2 \tau_{w,max}^* [h^*]^{-3} dr \Rightarrow \tilde{W}_{in} \propto \frac{1}{\mu u_{in}^2 d} \int_0^{r_w} \mu u_{in}^2 \tau_{w,max}^* [h^*]^{-3} dr = \tau_{w,max}^* [h^*]^{-3} \left( \frac{r_w}{d} \right) \quad (2.24)$$

The empirical relationship in equation (2.13) has the form  $[\tau_{w,max}^*]^m [h^*]^{-2}$ , where  $m = 2.34$ . A comparison between this form and the above relationship, and substitution of equation (2.21) along with the value of the observed constant  $n = -0.58$ , yields

$$\frac{r_w}{d} \propto [\tau_{w,max}^*]^{m-1} h^* \quad \Rightarrow \quad \frac{r_w}{h_{eq}} \propto Re_{in}^{(m-1)(n+1)} \approx Re_{in}^{0.56} \quad (2.25)$$

This indicates that the length scale in the problem which best represents the power dissipated by wall shear is the equilibrium gap height  $h_{eq}$ , but with a non-trivial dependence on the inlet Reynolds number. The reason for this Reynolds number dependence is likely related to both the growth of

the boundary layer on the wall, and the scale of the recirculation bubble on the pad (Nakabayashi Nakabayashi et al. (2002)).

As a final comment, we note that the “entrance length” of a pipe or channel is defined as a region with wall shear substantially above the value in the fully developed flow (White White (1974)). This is analogous to our definition of  $r_w$  within the gap between the pad and the wall. For planar channels, the dimensionless entrance length scales with  $Re^{1.0}$ . Equation (2.25) indicates that the entrance length to a radial outflow scales instead with  $Re_{in}^{0.56}$ , notably reduced from the planar case.

### 2.5.3 Hydraulic roughness

The roughness used in our simulations follows the model of monodisperse sand grain (Nikuradse Nikuradse (1950)). That source uses the roughness Reynolds number to define the wall as hydraulically smooth for  $\varepsilon^+ \lesssim 5$ , transitionally rough for  $5 < \varepsilon^+ < 70$ , and rough for  $\varepsilon^+ \gtrsim 70$ , where

$$\varepsilon^+ \triangleq \varepsilon u_\tau \rho / \mu, \quad u_\tau \triangleq \sqrt{\tau_w / \rho}$$

Although the present study was not undertaken in a zero-pressure gradient boundary layer, we can use these values to provide context for the material roughness employed in the simulations by defining a local value for  $\varepsilon^+$  based on the local value of  $u_\tau$ .

The flow was hydraulically smooth predominantly over most of the of the pad’s surface in all simulations. The worst case was observed for the nominal pad:  $d = 31.75$  mm,  $D = 200$  mm,  $h_{eq} = 1.5$  mm,  $\varepsilon_p = \varepsilon_w = 0.04$  mm, which showed  $\varepsilon^+ \approx 8.096$  at the point of maximum shear stress. For this worst case, there was a mild transitionally rough behavior around the region of maximum shear.

A full examination of the roughness in the context of the proposed biofouling removal application would probably require a more detailed description of the roughness, to include material properties and inhomogeneities. For the present work, we have restricted ourselves to a real material for which we have experimental data, and with a roughness which is small with respect to the gap height.

## 2.6 Concluding Remarks

A computational study of Bernoulli pads has been performed in order to determine a relationship between the input power required to maintain stable equilibrium and the maximum shear stress. The scaling law presented collapses the power and shear stress results of a large number of pad geometries and operating conditions onto a single curve. This collapse is extremely robust over the range of parameters examined. Because the inlet power is computed using a combination of the pressure and velocity at the inlet, it is not obvious *a priori* that the inlet power would be so well-described by the maximum value of shear stress. Kamensky et al. Kamensky et al. (2019), indicated that the fluid power scaled with “worst’ case” choices of characteristic parameters: largest velocity, largest gradient, and largest area. Although the largest velocity and gradient occur near the location of maximum shear stress, this position is much nearer to the jet exit  $d$  than the outer diameter  $D$ . These findings are not inconsistent, since the outer diameter is being used in Eq.(2.8) to scale the power, equilibrium height, and shear stress. It appears that (per the arguments made in the Discussion) the power expended to overcome wall shear over the entire pad is proportional to the maximum value.

Unusually, this work has used water as the working fluid in its simulations of the Bernoulli pad flow field. This is consistent with our proposed application, which is to use a Bernoulli pad to groom underwater surfaces without contact. This choice of working fluid introduces a great deal of potential richness - particularly cavitation - which has been ignored in the present work. Because cavitation occurs when the local pressure is below the vapor pressure, bubble formation tends to happen where the local velocity is large - precisely where we observe the highest wall shear stress. The design of alternate flow geometries which create sufficiently high levels of shear stress to groom surfaces while controlling cavitation will be examined in future work. Although it is unlikely that the scaling laws proposed here will work “off-the-shelf” on these new geometries, we anticipate that the techniques used here will be employed.

## CHAPTER 3

### FLOW PHYSICS OF A ROTATING BERNOULLI PAD

#### 3.1 Introduction

In the last chapter, the power-law relationship obtained for a Bernoulli pad suggests that there is a direct relationship between the fluid power delivered to the system and the losses due to shear in the radial direction. It is important to maximize shear forces in applications such as non-contact biofouling mitigation Kamensky et al. (2020); Tomar et al. (2022). To this end, it is important to consider other methods of delivering power to the system. As shown in Figure 3.1, we can envision rotating the pad about its axis, whereby mechanical power is provided in addition to fluid power. The additional power delivered to the system through rotation will increase losses due to shear, but the shear forces will now act in both radial and tangential directions. It is interesting to note that shear forces in the radial direction decrease with an increase in radial distance, whereas shear forces in the tangential direction increase with the increase in radial distance.

In the absence of a prime mover, a rotating pad produces attractive forces for all gap heights and does not produce a stable equilibrium configuration with the workpiece. The generation of attractive forces (or subatmospheric pressure) through the action of rotation (mechanical power) was first demonstrated experimentally by Demour in 1730 Houghtalen et al. (1996) using a T-shaped pipe; here it is demonstrated using simulations in Section 3.3. Interestingly, the addition of fluid power

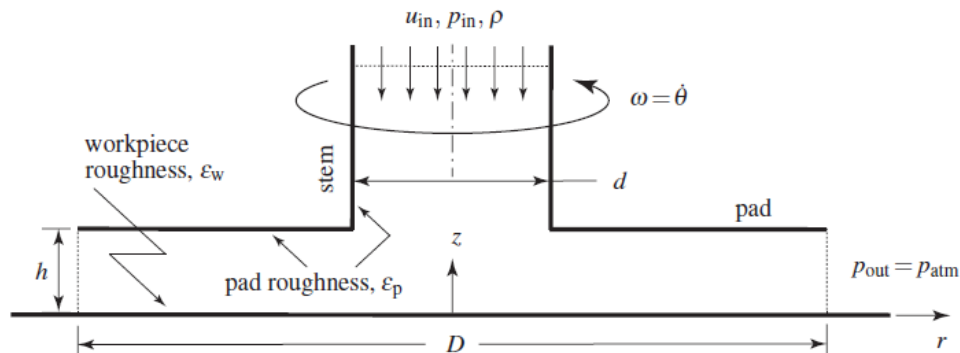


Figure 3.1 A schematic diagram of a Bernoulli pad provided with the additional capability of rotation.

to the rotating pad changes the nature of equilibria from unstable to stable and results in a rotating Bernoulli pad; this is presented in Section 3.4. A rotating Bernoulli pad has a unique property that is not observed with the standard non-rotating Bernoulli pad, namely the ability to produce a stable equilibrium configuration for two different mass flow rates; the attractive force is the same for both mass flow rates. The ability to produce the same force with two different flow rates can also be observed with a standard non-rotating Bernoulli pad but only in the repulsive regime; this has not been discussed in the literature, potentially because of its limited range of applications. Another important observation is that for the same level of inlet fluid power, a rotating Bernoulli pad generates a higher level of maximum shear stress compared to the standard non-rotating Bernoulli pad; this is discussed in Section 3.6.

The additional shear forces produced by a rotating Bernoulli pad increase the efficacy of grooming surfaces subjected to biofouling. "Grooming" Tribou and Swain (2010) is the gentle and frequent mechanical maintenance of a ship's hull to keep it clear of fouling organisms. This is an alternative to a less-frequent high-intensity "cleaning" procedure to avoid damaging coatings on the hull. These coatings are the first line of defense against biofouling and fall largely into two categories: antifouling (AF) and fouling-release (FR). AF coatings are biocidal, while FR coatings are slippery to fouling organisms. This allows shear forces to clean the ship while in motion Donnelly et al. (2022), but some level of preventative maintenance is also required Tribou and Swain (2010); Yeginbayeva and Atlar (2018), depending on coating type, local fouling pressure, time of year, and length of time in port. The in-water mechanical grooming tools are shear-based, whether by direct contact like brushes Dahlgren et al. (2022) or using fluid forces like water jets Oliveira and Granhag (2020), cavitating jets Song and Cui (2020), ultrasonics Trickey et al. (2022), bubbles Menesses et al. (2017), or a standard Bernoulli pad Kamensky et al. (2020); the standard Bernoulli pad can be augmented by rotation, which we describe in the present work.

In this work, we use a computational approach to examine the features of rotating pads and rotating Bernoulli pads. The computational approach is described and validated by our published data Tomar et al. (2022) in Section 3.2. Rotating pads act as centrifugal pumps and produce only

unstable equilibria; in contrast, rotating Bernoulli pads produce stable and unstable equilibria. We provide findings on the stiffness of the rotating systems, energy balance, and improvements to the normal force and maximum shear stress resulting from the addition of rotation.

## 3.2 Approach

### 3.2.1 Computational Domain

A rotating Bernoulli pad is shown in Figure 3.1;  $d$  and  $D$  denote the inner and outer diameter,  $h$  denotes the gap between the pad and the workpiece,  $\varepsilon_p$  and  $\varepsilon_w$  denote the height of the roughness of the pad and the workpiece surfaces,  $\rho$  denotes the density of the fluid,  $u_{in}$  represents the fluid velocity at the inlet,  $p_{in}$  represents the pressure at the inlet, and the angular speed of rotation of the pad is denoted by  $\omega = \dot{\theta}$ . The pressure at the outlet of the flow is atmospheric, *i.e.*,  $p_{out} = p_{atm}$ .

The values of the parameters used for the Computational Fluid Dynamics (CFD) simulations are provided in Table 3.1; these values match those used in our previous investigation Tomar et al. (2022) with the exception of the value of  $d$ . A larger value of  $d$  is used here to ensure that a stable equilibrium can be achieved with a zero net normal force on the workpiece Kamensky et al. (2019) for a reasonable mass flow rate. The working fluid is water, and the surface roughness values used here are consistent with the material of the pad and workpiece used in the experiments Tomar et al. (2022); Kamensky (2020) *i.e.*, structural steel.

The investigation method used in this work is CFD simulations carried out using ANSYS Fluent. A 2-D steady-state incompressible Navier-Stokes equation is solved using a coupled scheme, which provides a robust and efficient steady-state solution compared to other segregated

Table 3.1 Parameter values used in CFD simulations

$\omega$ [rad/s]	$\dot{m}_{in}$ [kg/s]
$d$	63.5 mm
$D$	200 mm
$h$	1.5 mm
$\varepsilon_p = \varepsilon_w$	0.04 mm
$\rho$	998.2 kg/m <sup>3</sup>
$\mu$	0.001 Ns/m <sup>2</sup>

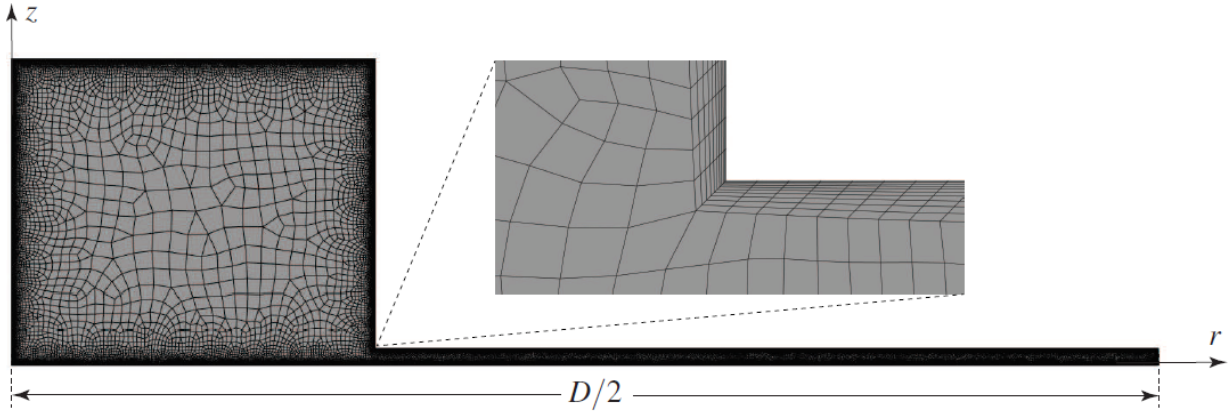


Figure 3.2 Axisymmetric flow domain of the rotating Bernoulli pad with hybrid mesh.

schemes ANSYS (2022). Because the geometry and boundary conditions are axisymmetric, we used a 2-D axisymmetric solver to reduce run time. The pad rotation  $\omega$  about the  $z$ -axis is imposed using an axisymmetric swirl module, which assumes zero gradient but non-zero velocity in the circumferential direction  $\theta$ . At the inlet of the computational domain, we impose a mass flux boundary condition  $\dot{m}_{in}$ . At the outlet, the gauge pressure is zero, *i.e.*,  $p_{atm} = 0$ . The workpiece is kept stationary with a no-slip boundary condition at a gap height  $h$  from the rotating pad.

The pressure is discretized using the PRESTO (PREssure STaggering Option) since it is well suited for steep pressure gradients generated by the flow impinging on the workpiece Islam et al. (2020). The Reynolds Stress Model (RSM) is used to model turbulence, which is widely used for studies involving swirling motion Gibson et al. (2017) and vortices Neto et al. (2011). The RSM is well suited to the severe streamline curvature caused by the swirling motion of the pad Jawarneh and Vatistas (2006). The spatial terms for momentum, swirl velocity, and Reynolds stresses are discretized using a second-order upwind scheme. The mesh of the computational domain is shown in Figure 3.2; a magnified view of the mesh at the neck of the Bernoulli pad is shown inset. The mesh is hybrid and is comprised of quadrilateral (dominant) and triangular elements.

### 3.2.2 Experimental Validation

The numerical methods are compared with the results from a Particle Tracking Velocimetry (PTV) experiment Kamensky (2020) to gain confidence in the numerical solver and discretization

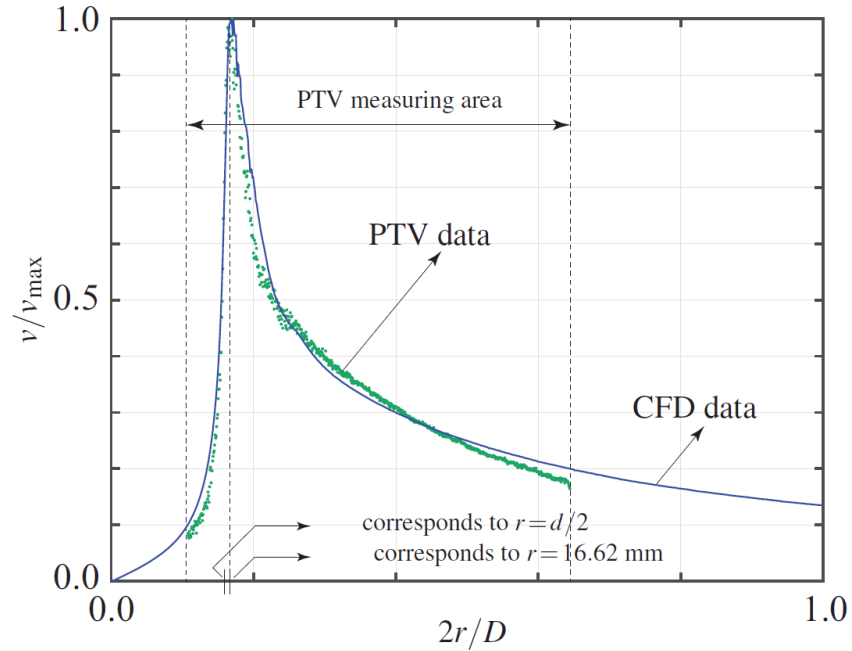


Figure 3.3 Comparison of PTV (data taken from Tomar et al. (2022)) and CFD data: plot of the nondimensional radial velocity at  $z = h/2$  with respect to the nondimensional radial position.

schemes. The experimental work Kamensky (2020) used a different set of parameters ( $d = 15.875$  mm,  $D = 100$  mm,  $h = 1.275$  mm); these values were used in the numerical simulation for comparison. The pad was not rotating ( $\omega = 0$ ), and the value of the mass flow rate was  $\dot{m}_{in} = 0.59$  kg/s. If  $v$  denotes the radial velocity at the middle of the gap ( $z = h/2$ ), the non-dimensional radial velocity is defined as  $v^* = v/v_{max}$ , where  $v_{max}$  is the maximum value of the radial velocity. Similarly, the non-dimensional radial position is defined as  $r^* = 2r/D$ . The non-dimensional radial velocity for the numerical solution and the experiment are plotted as a function of the non-dimensional radial position in Figure 3.3. The velocity profile shows good agreement between the numerical simulation and PTV experiments. In particular, both cases show  $v_{max}$  at nearly the same location ( $r \approx 16.62$  mm), very close to the neck, where the fluid enters the gap in the radial direction. This indicates that the numerical model captures the recirculation just downstream of the neck in a satisfactory manner.

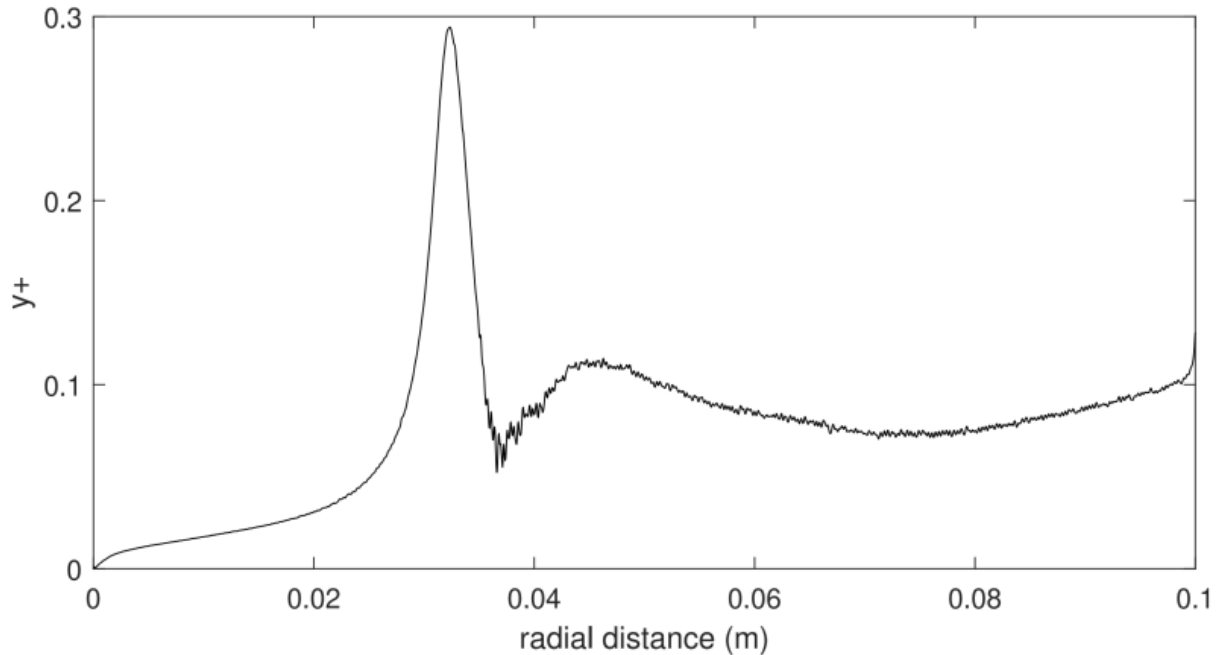


Figure 3.4 Variation of  $y^+$  values over the workpiece in the radial direction.

### 3.2.3 Grid Independence Study

The CFD simulations are carried out using an element size of  $4 \times 10^{-5}$  m, which resulted in 94,547 elements and a maximum  $y^+$  value of 0.27 over the entire range of the workpiece as shown in Figure 3.4. A smaller element size of  $3 \times 10^{-5}$  m resulted in 127,189 elements, but the percentage change in the values of the variables of interest, namely, the normal force and the maximum shear stress on the workpiece, were found to be 1.09 % and 0.54 %, respectively, and did not justify the additional computational cost.

### 3.2.4 Comparison of axisymmetric swirl module with three-dimensional domain

We have carried out a numerical simulation of a three-dimensional computational domain with identical dimensions used in Table 3.1. The domain is provided with a mass flow rate of 0.5 kg/s and a rotational speed of 10 rad/s. The results obtained with the three-dimensional simulations are used to compare the results obtained with the axisymmetric swirl module. A comparison of wall shear stress generated on the workpiece and radial velocity at the center of the gap height is shown in Figure 3.5 and Figure 3.6. The qualitative nature of the variation of wall shear stress and

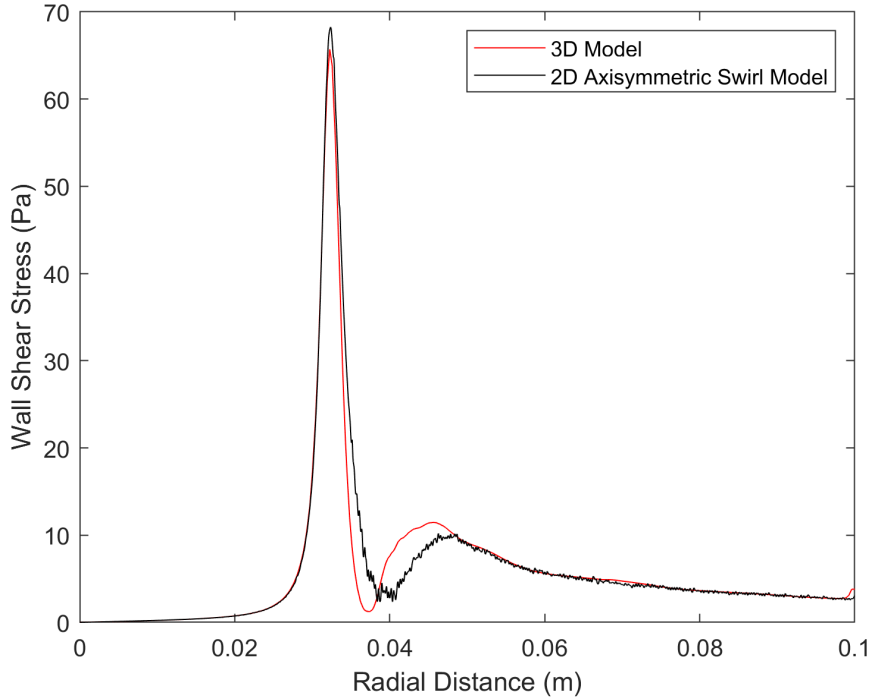


Figure 3.5 Variation of wall shear stress over the workpiece in the radial direction for 3D and axisymmetric swirl module.

radial velocity is captured well in both cases. The error between the maximum value of wall shear stress and radial velocity is also small, which provides us with confidence in the axisymmetric swirl module of the solver. The difference in the magnitude of the maximum velocity can be attributed to the coarser mesh used in the axisymmetric domain and it can be avoided by further refining the mesh but it is out of the scope for this kind of work.

### 3.3 Flow physics of a rotating pad

A Bernoulli pad involves a prime mover that pumps fluid through the inlet - see Figure 3.1. To understand the effect of rotation of the Bernoulli pad on the flow physics, we first consider a rotating pad with the inlet exposed to atmospheric pressure, *i.e.*,  $p_{in} = p_{atm}$ . Numerical simulations are carried out to simulate the flow physics of a rotating pad for the parameter values in Table 3.1 and the set of angular speeds  $\omega \in \{10, 20, 30, 40, 50, 60\}$  rad/s. The rotating pad can be considered to be a centrifugal pump.

For the rotating pad, numerical computation of the flow is challenging since both the inlet and

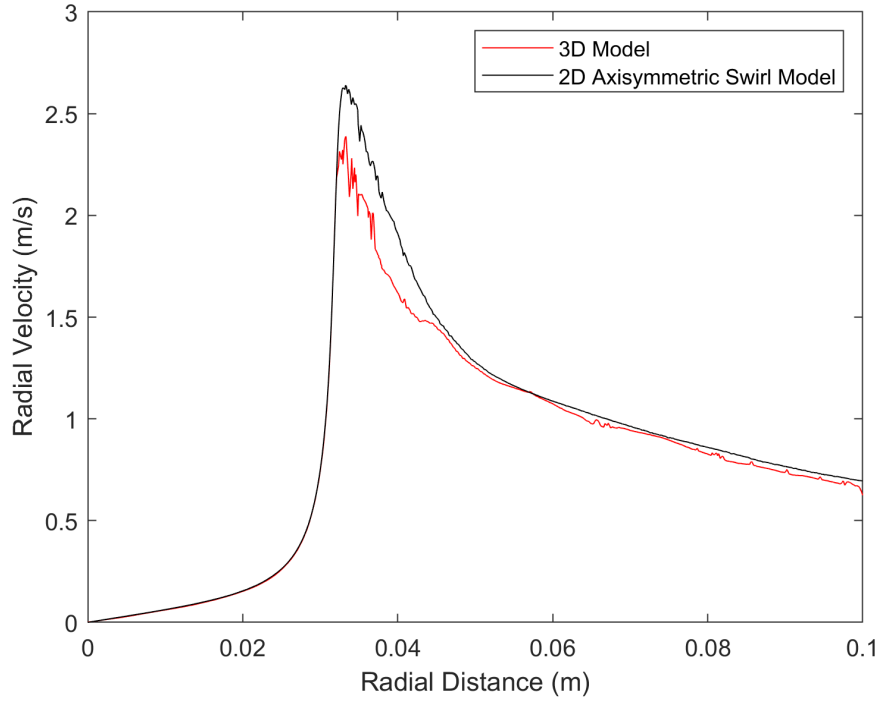


Figure 3.6 Variation of radial velocity at  $h = h/2$  over the workpiece in the radial direction for 3D and axisymmetric swirl module.

Table 3.2  $\dot{m}_{in}$  required to achieve  $p_{in} = p_{atm}$  for different  $\omega$

$\omega$ [rad/s]	$\dot{m}_{in}$ [kg/s]
10	0.0520
20	0.1100
30	0.1700
40	0.2280
50	0.2830
60	0.3389

the outlet have the same pressure boundary conditions, namely,  $p_{in} = p_{out} = p_{atm}$ . To address this challenge, the pressure boundary condition is imposed at the outlet, and the inlet mass flow rate  $\dot{m}_{in}$  is varied iteratively till the condition  $p_{in} = p_{atm}$  is satisfied; this condition corresponds to zero static pressure at the inlet. The  $\dot{m}_{in}$  required to satisfy the pressure boundary conditions for the chosen set of angular velocities is provided in Table 3.2.

The pressure  $p$  on the workpiece surface is presented in Figure 3.7 for the set  $\omega \in \{10, 20, 30, 40, 50, 60\}$

rad/s. It is equal to the stagnation pressure in the region below the inlet; it is small but different for different rotational speeds. The difference in the stagnation pressure can be attributed to the difference in the mass flow rates at the inlet  $\dot{m}_{in}$  - see Table 3.2. A higher speed of rotation results in a higher value of  $\dot{m}_{in}$  and a higher value of stagnation pressure at the workpiece. The pressure on the workpiece at the neck, where the axial flow becomes radial, drops rapidly due to the large increase in the radial velocity owing to the constriction of the flow - see Figure 3.8.

For a given pad and rotational speed, the gap between the pad and the workpiece dictates the normal force generated on the workpiece. The normal force  $F$ , which is obtained by integrating the pressure on the workpiece (see Figure 3.7), is negative and hence attractive (attempts to pull the pad and the workpiece closer). An external force, equal and opposite to the normal force, can maintain equilibrium, but the nature of this equilibrium (stable or unstable) will depend on the stiffness of the flow field in the  $z$  direction - see Figure 3.1. The stiffness can be computed from the change in

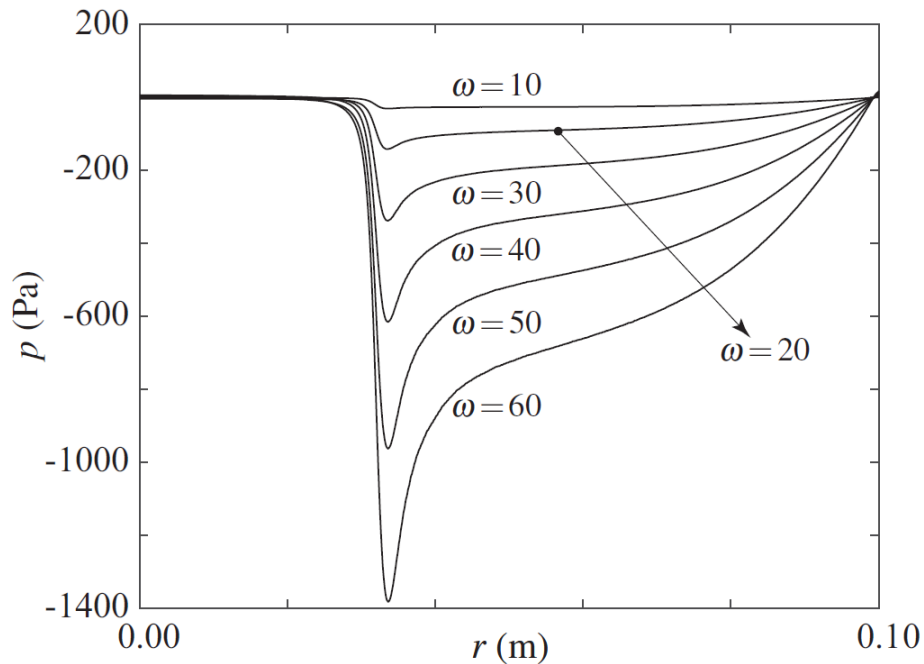


Figure 3.7 Rotating pad with parameters in Table 3.1: Pressure on the workpiece surface as a function of the radial position for different angular speeds.

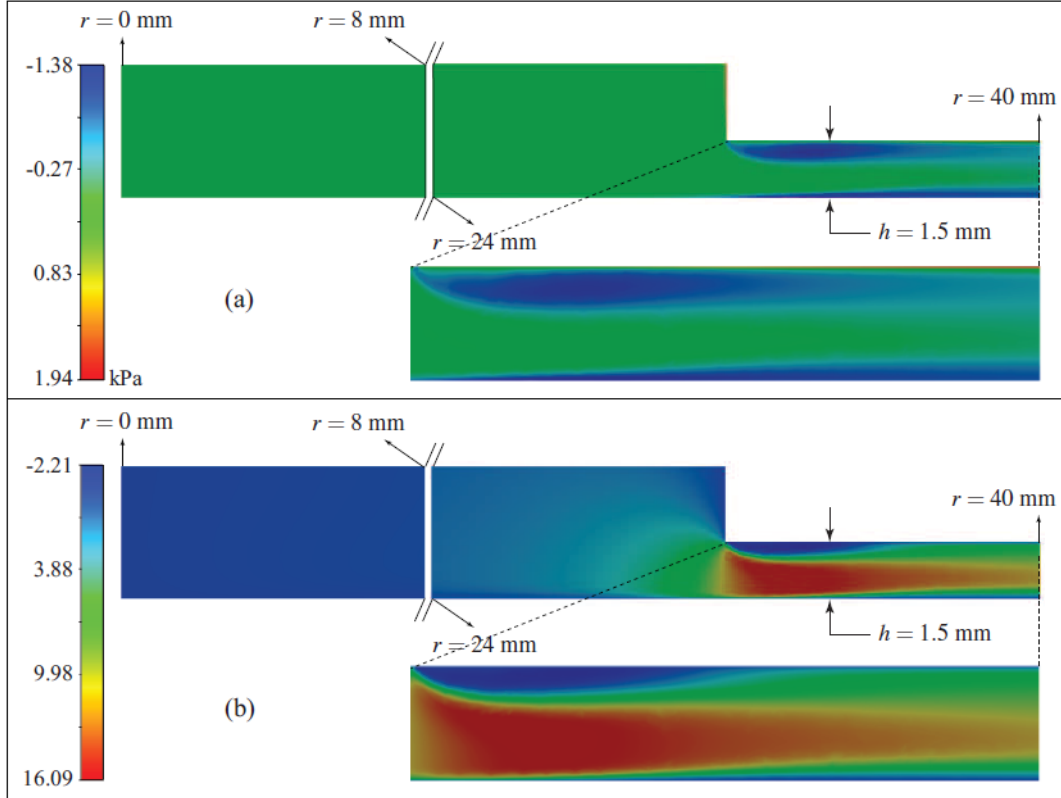


Figure 3.8 Contours of (a) pressure and (b) nondimensional radial velocity ( $v/u_{in}$ ) for a rotating pad. A portion of the stagnation region  $r \in [0, 8]$  mm and the neck region of the pad  $r \in [24, 40]$  mm are provided along with a magnified view of the neck region.

the normal force  $F$  due to a change in the gap, as follows:

$$k = -\frac{\Delta F}{\Delta h} \quad (3.1)$$

where  $\Delta F$  is the change in the normal force and  $\Delta h$  is the change in the gap. The stiffness of the flow field is shown in Figure 3.9 for different angular speeds about the nominal gap of  $h = 1.5$  mm. The negative value of the stiffness indicates that a bias force can be used to generate an equilibrium, but the nature of the equilibrium is unstable for all  $\omega$ .

### 3.4 Flow physics of a rotating Bernoulli Pad

We now consider a rotating Bernoulli pad, where a prime mover does non-negative work to pump the fluid through the inlet, and the pad has an angular speed  $\omega$ . Similar to the rotating pad, the inlet boundary condition is the mass flux  $\dot{m}_{in}$ , but the mass flux is not iterated to find an inlet

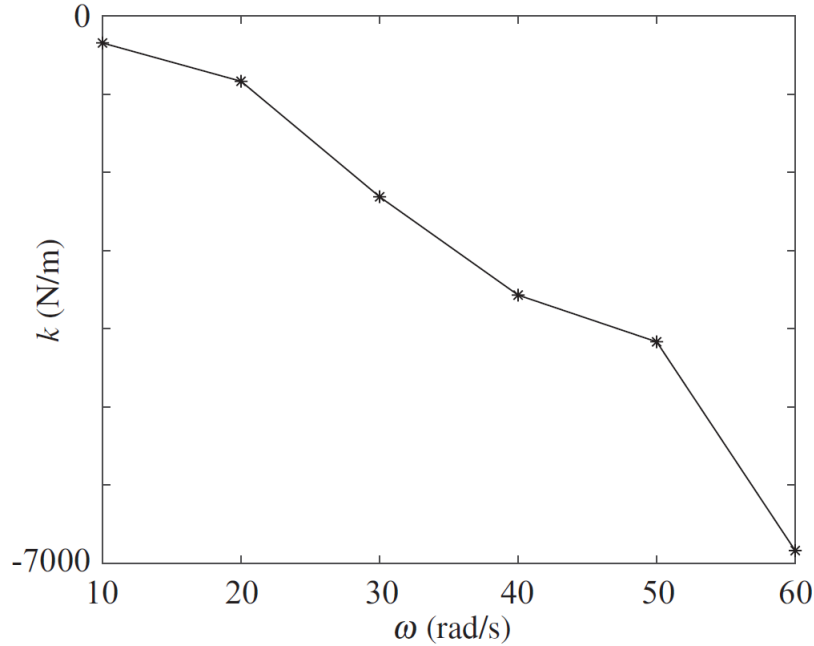


Figure 3.9 Stiffness of the flow field generated by the rotating pad at  $h = 1.5$  mm for  $\omega \in \{10, 20, 30, 40, 50, 60\}$  rad/s.

pressure of zero; *i.e.*,  $p_{in} \neq p_{atm}$ . The force on the workpiece produced by varying the mass flow rate is provided in Figure 3.10 for  $\omega \in \{0, 20, 40, 60\}$ . It can be seen that the lowest value of  $\dot{m}_{in}$  is different for each curve corresponding to  $\omega$ ; these different  $\dot{m}_{in}$  values correspond to the boundary condition  $p_{in} = p_{atm}$ , provided in Table 3.2. The motivation to use these  $\dot{m}_{in}$  values as the starting point is to ensure that the work done by the prime mover is not negative.

In Figure 3.10, the  $\omega = 0$  curve corresponds to the standard non-rotating Bernoulli pad. The variation in the normal force  $F$  with increasing mass flow rate  $\dot{m}_{in}$  is in agreement with results in the literature Li and Kagawa (2014): as  $\dot{m}_{in}$  is increased,  $F$  initially increases and becomes positive (repulsive), reaches a maximum value, then decreases and becomes negative (attractive). When the pad is provided an angular speed, the concave-downward trend in the variation of  $F$  with  $\dot{m}_{in}$  remains unchanged, but the values of the normal force uniformly decrease. The decrease in the normal force is proportional to the increase in the angular speed; this is in agreement with our discussion in Section 3.3.

The rotating Bernoulli pad can be viewed as a modification of the standard non-rotating Bernoulli

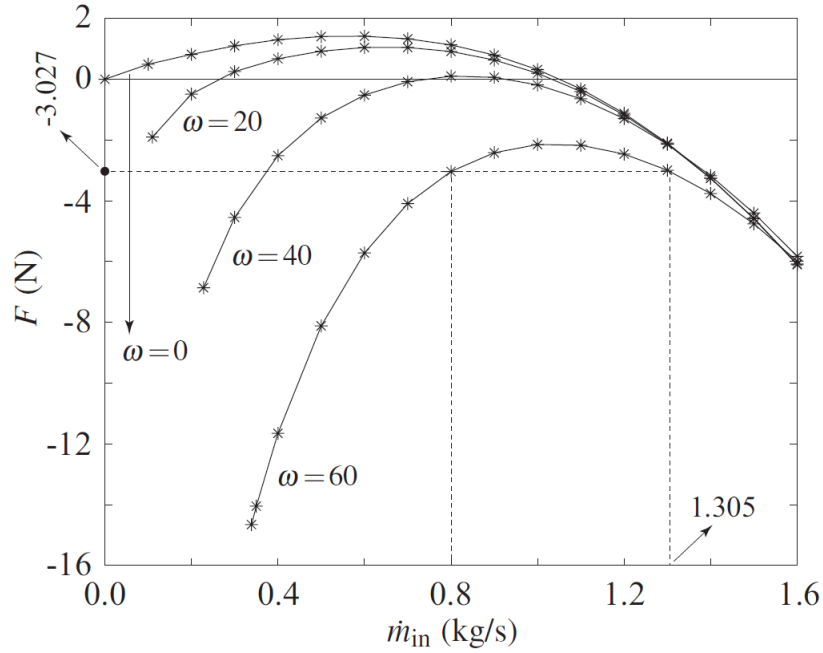


Figure 3.10 Bernoulli pad with parameters in Table 3.1: Normal force on the workpiece as a function of the mass flow rate for  $\dot{m}_{in}$

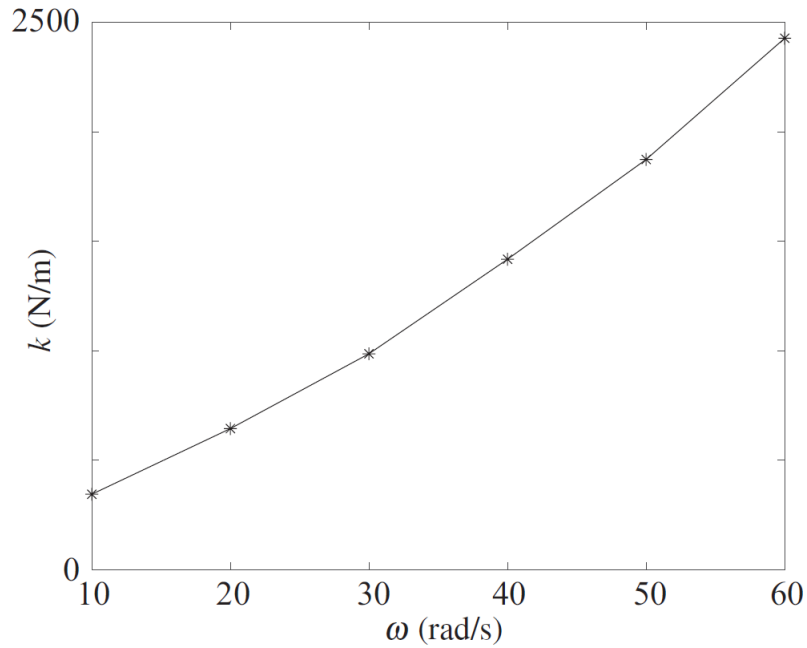


Figure 3.11 Stiffness of the flow field generated by the rotating Bernoulli pad at  $h = 1.5$  mm and  $\dot{m}_{in} = 0.5$  kg/s, for  $\omega \in \{10, 20, 30, 40, 50, 60\}$  rad/s.

pad where the radial velocity in the gap is primarily due to the fluid power provided at the inlet, and the tangential velocity in the gap is due to pad rotation. Therefore, as  $\dot{m}_{in}$  is increased, the effect of the radial velocity becomes prominent compared to that of the tangential velocity, and the curves for nonzero  $\omega$  in Figure 3.10 sequentially converge to the curve corresponding to the standard non-rotating Bernoulli pad with  $\omega = 0$ . The convergence of the curves corresponding to  $\omega = 0$  and  $\omega = 20$  is observed for a lower mass flow rate compared to that for convergence of the curves corresponding to  $\omega = 0$ ,  $\omega = 20$  and  $\omega = 40$ . All the curves converge together for the mass flow rate of  $\dot{m}_{in} \approx 1.6$  kg/s.

Figure 3.11 shows the stiffness of the flow field generated by the rotating Bernoulli pad as a function of  $\omega$  at  $h = 1.5$  mm and for  $\dot{m}_{in} = 0.5$  kg/s. Unlike the rotating pad, the stiffness is positive for all  $\omega$ , which indicates that an equilibrium configuration of the pad will be stable. This may be reconciled with the flow physics of the rotating pad discussed in Section 3.3. As the mass flow rate increases due to work done by a prime mover, the pressure at the inlet increases, and this provides a repulsive normal force on the workpiece for small values of  $r$ .

The repulsive force balances the attractive force generated by the flow in the gap, which now includes a significant radial component compared to the rotating pad and yields a stable equilibrium. Thus, the mass flow rate provided by a prime mover converts a rotating pad into a rotating Bernoulli pad and an unstable equilibrium configuration into a stable equilibrium configuration. Although the results in Figure 3.11 pertain to  $\dot{m}_{in} = 0.5$  kg/s, all points on the four curves in Figure 3.10, except the starting point on each curve which do not require a prime mover, results in stable equilibrium configurations.

Another important observation that can be made from Figure 3.10 is that for a specific angular velocity, a horizontal line will provide the same force values at two different mass flow rates. For example, mass flow rates of  $\dot{m}_{in} = 0.8$  kg/s and  $\dot{m}_{in} = 1.305$  kg/s generate the same normal force of  $F = -3.027$  N when the Bernoulli pad is rotating with  $\omega = 60$  rad/s. Therefore, with a bias force of  $+3.027$  N, it is possible to have an equilibrium configuration with two different mass flow rates. The variation of the pressure on the workpiece for these two mass flow rates is presented in Figure

3.12. The integral of the area for both these curves represents the normal force  $F$  generated on the workpiece and turns out to be equal in this case.

The stiffness values corresponding to these mass flow rates are, however, different, equal to  $k = 16,412 \text{ N/m}$  for  $\dot{m}_{\text{in}} = 0.8 \text{ kg/s}$  and  $k = 31,982 \text{ N/m}$  for  $\dot{m}_{\text{in}} = 1.305 \text{ kg/s}$ . The positive values of the stiffness indicate that the equilibrium configuration will be stable, but the flow field will have a higher stiffness for a higher mass flow rate, and vice versa. This unique phenomenon occurs due to the concave-downward nature of the variation of  $F$  with  $\dot{m}_{\text{in}}$  (see Figure 3.10); therefore, the phenomenon is observed for all angular speeds, including zero angular speed or the standard non-rotating Bernoulli pad. Although a rotating Bernoulli pad has not been investigated in the literature, the phenomenon of a stable equilibrium where the flow field can have two different stiffnesses corresponding to two different mass flow rates has not been discussed in the context of the standard non-rotating Bernoulli pad. Such equilibria will henceforth be referred to as bi-stiffness stable equilibria.

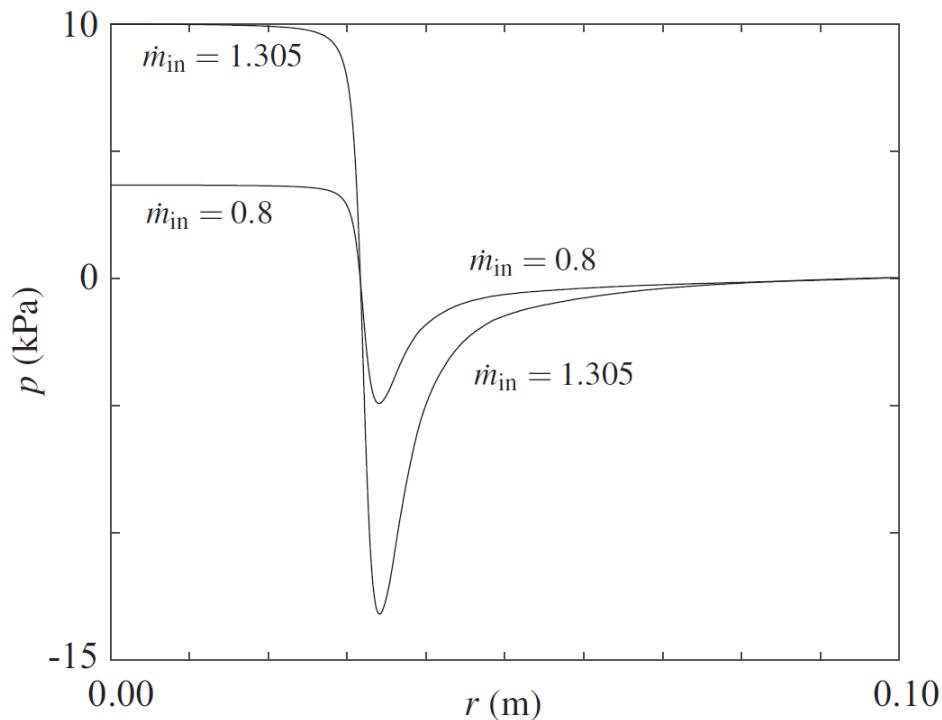


Figure 3.12 Rotating Bernoulli pad with parameters in Table 3.1 and  $\omega = 60 \text{ rad/s}$ : Pressure on the workpiece as a function of radial position for  $\dot{m}_{\text{in}} = 0.8 \text{ kg/s}$  and  $\dot{m}_{\text{in}} = 1.305 \text{ kg/s}$ .

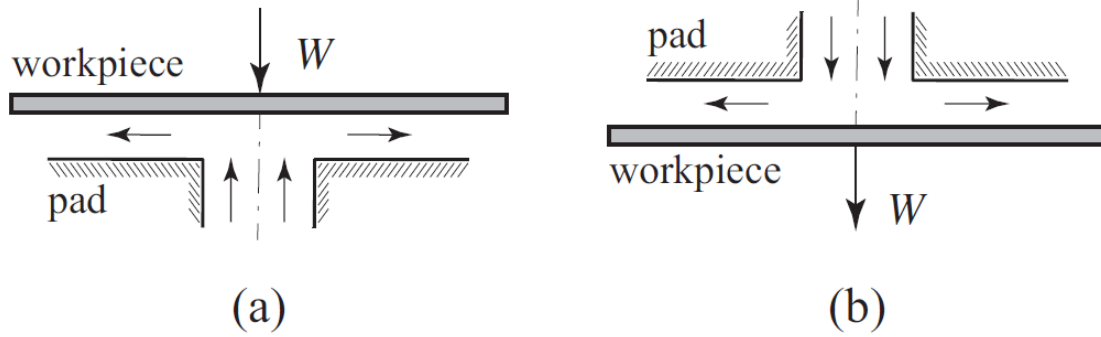


Figure 3.13 A workpiece of weight  $W$  being supported by a Bernoulli pad from (a) below and (b) above.

A horizontal line that intersects the  $\omega = 0$  curve at two points (corresponding to two mass flow rates) in Figure 3.10 results in a positive value of  $F$ , whereas a horizontal line that intersects the  $\omega = 60$  curve results in a negative value of  $F$ . This implies that a standard non-rotating Bernoulli pad can support a workpiece in a bi-stiffness stable equilibrium configuration only from below - see Figure 3.13 (a). In contrast, the Bernoulli pad rotating with  $\omega = 60$  rad/s can support a workpiece in a bi-stiffness stable equilibrium configuration only from above - see Figure 3.13 (b). In industry applications, a standard non-rotating Bernoulli pad is typically used to support a workpiece from above ( $\dot{m}_{in}$  is chosen such that  $F$  is negative in Figure 3.10; this produces a stable equilibrium configuration); this may explain why bi-stiffness stable equilibria have not been discussed in the literature.

The concept of bi-stiffness equilibria is not limited to a specific pair of mass flow rate curves. In fact, the production of bi-stiffness equilibria is observed for any arbitrary choice of mass flow rate values in the CFD simulations. The effect of rotational speed on the normal suction force is presented in Figure 3.14 for a range of mass flow rate values. The value of normal suction force increases rapidly with the rotational speed for lower mass flow rate values. Hence, every single curve in Figure 3.14 will intersect with another curve at a unique location. This unique location represents a pad with fixed gap height at which the system has the same normal suction force for a given rotational speed.

A magnified view of the Figure 3.14 is shown in Figure 3.15. The legends in this figure for

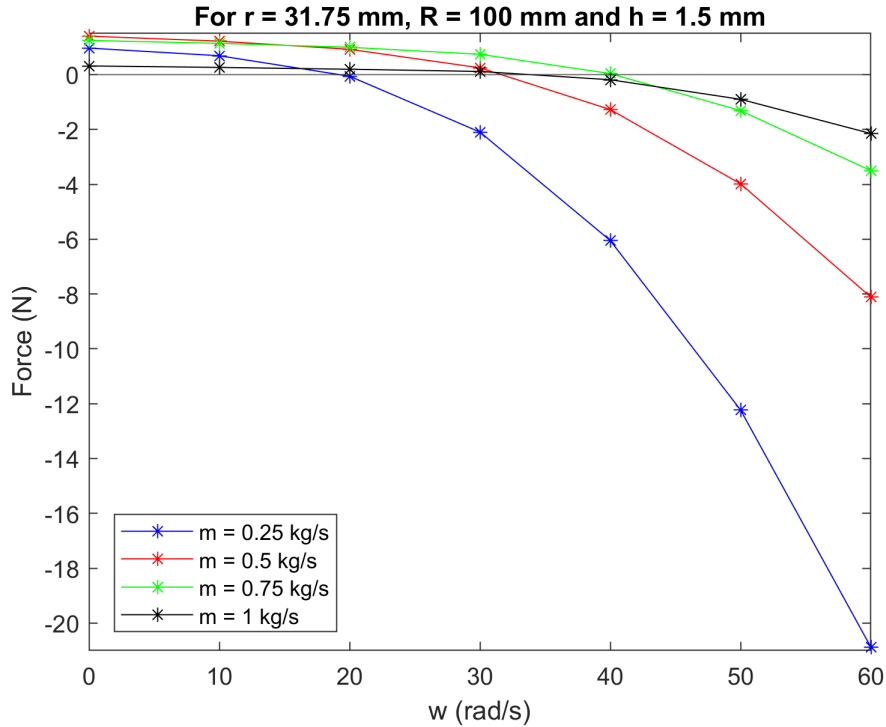


Figure 3.14 Variation of force with angular speed for different  $\dot{m}_{in}$

different mass flow rates are similar to those in Figure 3.14. In Figure 3.15, data on the y-axis is clipped to the positive value of the forces. The  $\dot{m}_{in} = 0.5$  kg/s curve intersect with the  $\dot{m}_{in} = 0.75$  kg/s curve at  $\omega \approx 15$  rad/s and  $\dot{m}_{in} = 1$  kg/s at  $\omega \approx 32$  rad/s. The  $\dot{m}_{in} = 0.5$  kg/s curve will not intersect the  $\dot{m}_{in} = 0.25$  kg/s curve because the effect of rotation is higher on the smaller mass flow rate curves and, therefore, the suction force generation is rapid.

### 3.5 Rotating Bernoulli Pad: Variation of Normal Force with Gap Height

The normal force generated by a standard non-rotating Bernoulli pad strongly depends upon the gap height. The variation of the force with the gap height is well explained in the literature, Li and Kagawa (2014). The sudden contraction of the fluid at the neck results in a pressure less than the atmospheric pressure, thereby producing attractive forces. Here, we present CFD simulation results to compare the pressure profile on the workpiece for rotating and non-rotating Bernoulli pads with parameters in Table 3.1; the results are shown in Figure 3.16 for  $\omega = 0$  rad/s and  $\omega = 60$  rad/s. For both cases, the inlet boundary condition was  $\dot{m}_{in} = 0.5$  kg/s. The normal force  $F$ , obtained by

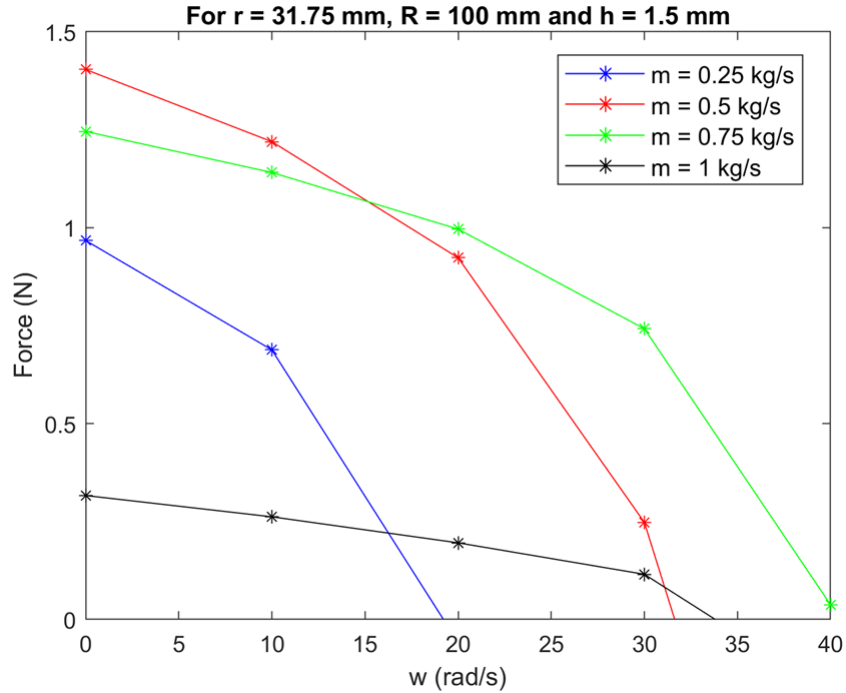


Figure 3.15 A magnified view of the variation of force with angular speed for different  $\dot{m}_{in}$  with the legends similar to Figure 3.14

integrating the pressure curves in Figure 3.16, is equal to 1.4037 N for  $\omega = 0$  rad/s and  $-8.1153$  N for  $\omega = 60$  rad/s. This is expected as the pressure curve for  $\omega = 60$  rad/s uniformly lies below the pressure curve for  $\omega = 0$  rad/s. The decrease in the value of  $F$  from a positive to a negative number (or from a repulsive to attractive force) is due to the effect of rotation. These forces are shown in Figure 3.17, which will be discussed next.

The effect of rotation on the variation of the normal force on the workpiece with gap height is shown in Figure 3.17 for a mass flow rate of  $\dot{m}_{in} = 0.5$  kg/s. Every design point in the figure, with the addition of a suitable bias force, corresponds to a stable equilibrium configuration; this can be verified from the uniformly negative slope of the curves corresponding to each angular speed  $\omega$ . It can be seen that an increase in the angular speed uniformly lowers the value of the normal force  $F$ . This observation, made earlier for  $h = 1.5$  mm, is found to be true for all gap heights, implying that a rotating Bernoulli pad can lift or support more weight than a non-rotating Bernoulli pad for a given mass flow rate.

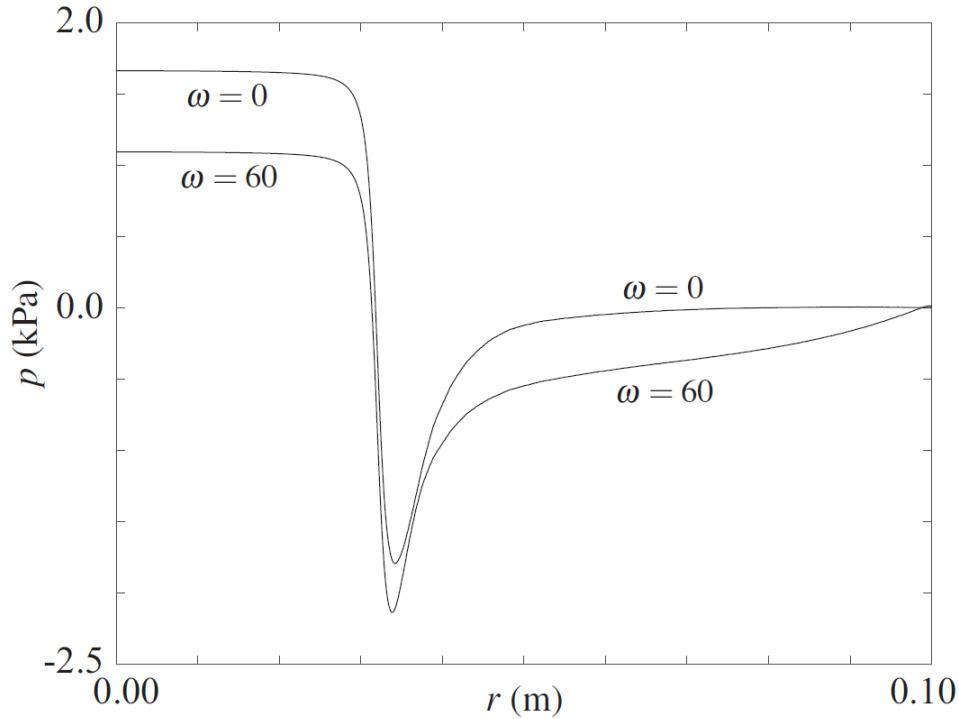


Figure 3.16 Rotating Bernoulli pad with parameters in Table 3.1 and  $\dot{m}_{in} = 0.5$  kg/s: Pressure on the workpiece as a function of radial position for  $\omega = 0$  rad/s and  $\omega = 60$  rad/s.

A similar trend is observed for smaller values of mass flow rate and rotational rate. The effect of lower rotational speed for a mass flow rate of  $\dot{m}_{in} = 0.1$  kg/s and  $\dot{m}_{in} = 1.045$  kg/s is shown in Figure 3.18 and Figure 3.19 respectively. All the design points on these plots correspond to the stable equilibrium; this can be verified from the uniformly negative slope of the curves corresponding to each angular speed  $\omega \in \{0, 5, 10, 15\}$  rad/s. For a particular value of gap height, the addition of rotation speed results in an increase of normal suction force (or a decrease in the normal repulsive force). The effect of rotation on the Bernoulli pad is negligible for the design points with higher values of mass flow rate, as shown in Figure 3.19. In this case, the suction flow physics of the Bernoulli pad is dominated by the power available at the inlet.

The  $\omega = 10$  rad/s curve from the Figure 3.18 and Figure 3.19 is taken out and plotted against each other in Figure 3.20. The curves corresponding to two different mass flow rates intersect each other at  $h = 1.5$  mm, and the normal suction force corresponding to this orientation is zero. In fact, these mass flow rate values were initially chosen to make sure that they correspond to the stable

equilibrium configuration with zero force. The figure also shows the difference in the stiffness value for the same configuration at stable equilibrium. For the smaller value of stiffness, the stiffness value is also small, which in turn means that a very small value of external force is required to pull this configuration out of the stable equilibrium.

On the other hand, the external force required to disturb the equilibrium for  $\dot{m}_{in} = 1.045$  kg/s is higher. This bi-stiffness equilibria is not limited to one rotational speed. Numerical simulations are extended to obtain the zero normal force stable equilibrium configuration for  $\omega = 5$  rad/s and  $\omega = 20$  rad/s. For  $\omega = 5$  rad/s, the mass flow rate values  $\dot{m}_{in} = 0.037$  kg/s and  $\dot{m}_{in} = 1.05$  kg/s results in zero normal force stable equilibrium configuration as shown in the Figure 3.21 and for  $\omega = 20$  rad/s, the mass flow rate values  $\dot{m}_{in} = 0.257$  kg/s and  $\dot{m}_{in} = 1.036$  kg/s results in zero normal force stable equilibrium configuration as shown in the Figure 3.22. A similar behavior with bi-stiffness equilibria is observed in both figures.

The variation of total pressure for the mass flow rate values plotted in the Figure 3.20 are shown

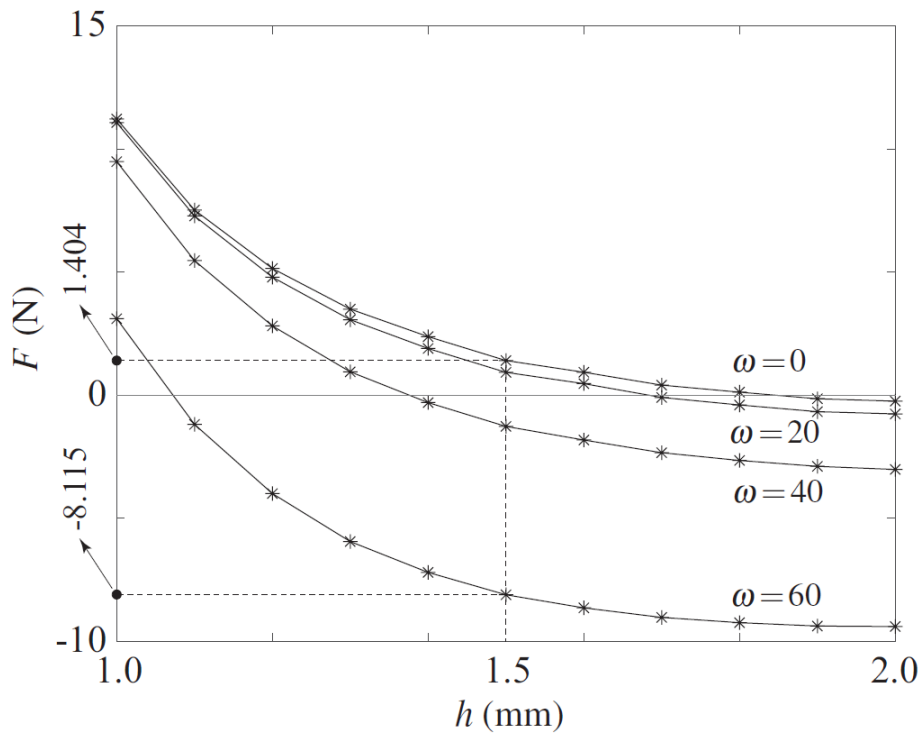


Figure 3.17 Bernoulli pad with parameters in Table 3.1, except  $h$ : Normal force on the workpiece as a function of the gap height for  $\dot{m}_{in} = 0.5$  kg/s and  $\omega \in \{0, 20, 40, 60\}$  rad/s.

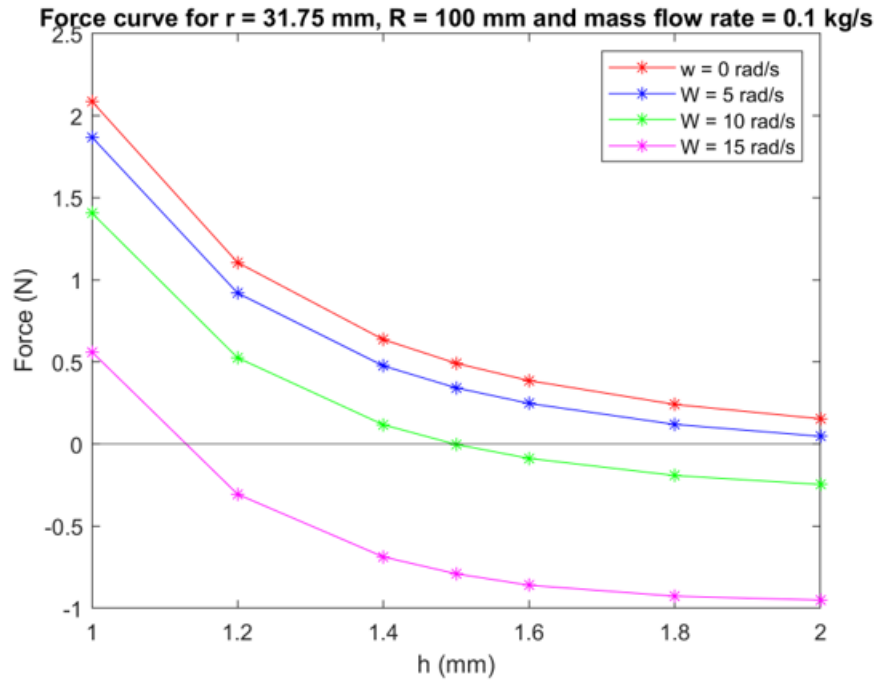


Figure 3.18 Normal force on the workpiece as a function of the gap height for  $\dot{m}_{in} = 0.1$  kg/s.

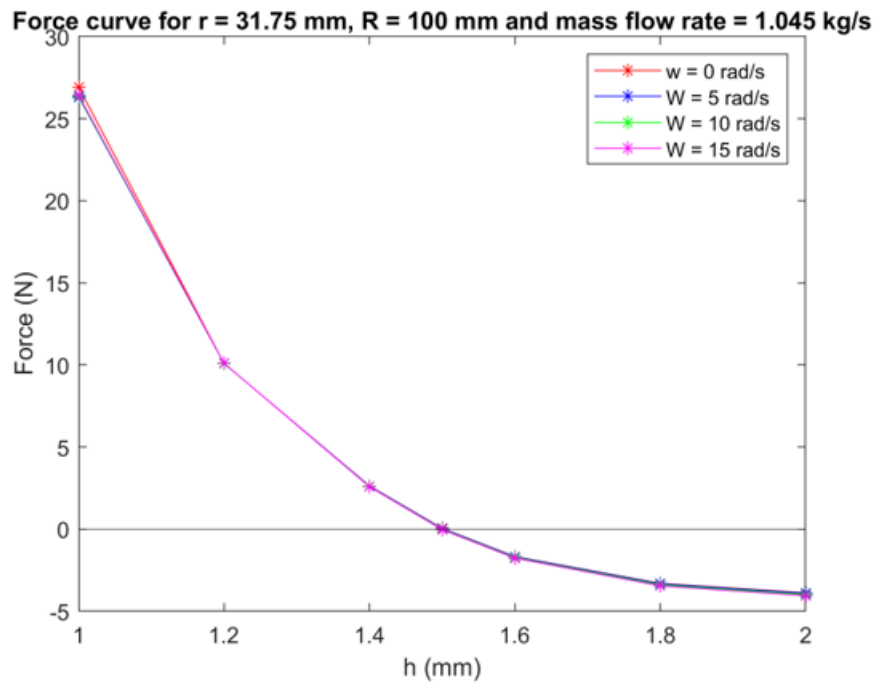


Figure 3.19 Normal force on the workpiece as a function of the gap height for  $\dot{m}_{in} = 1.045$  kg/s.

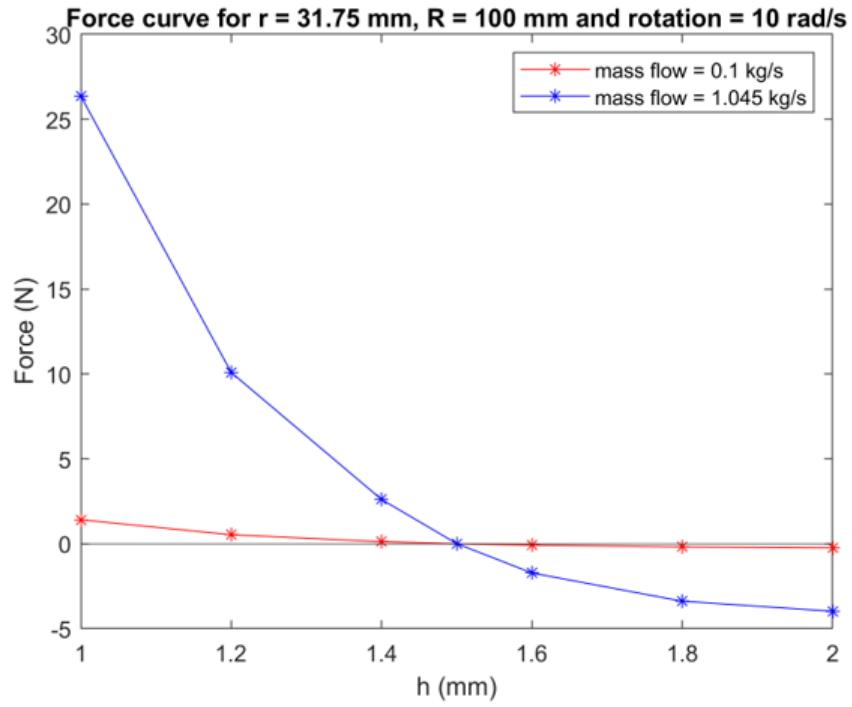


Figure 3.20 Force curve to obtain bi-stiffness equilibria for  $\omega = 10$  rad/s.

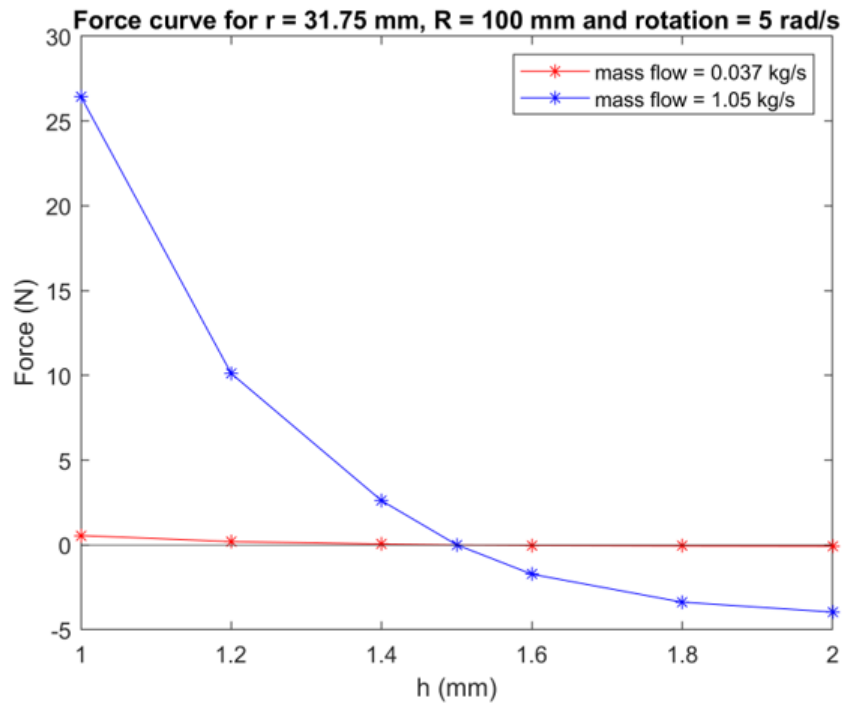


Figure 3.21 Force curve to obtain bi-stiffness equilibria for  $\omega = 5$  rad/s.

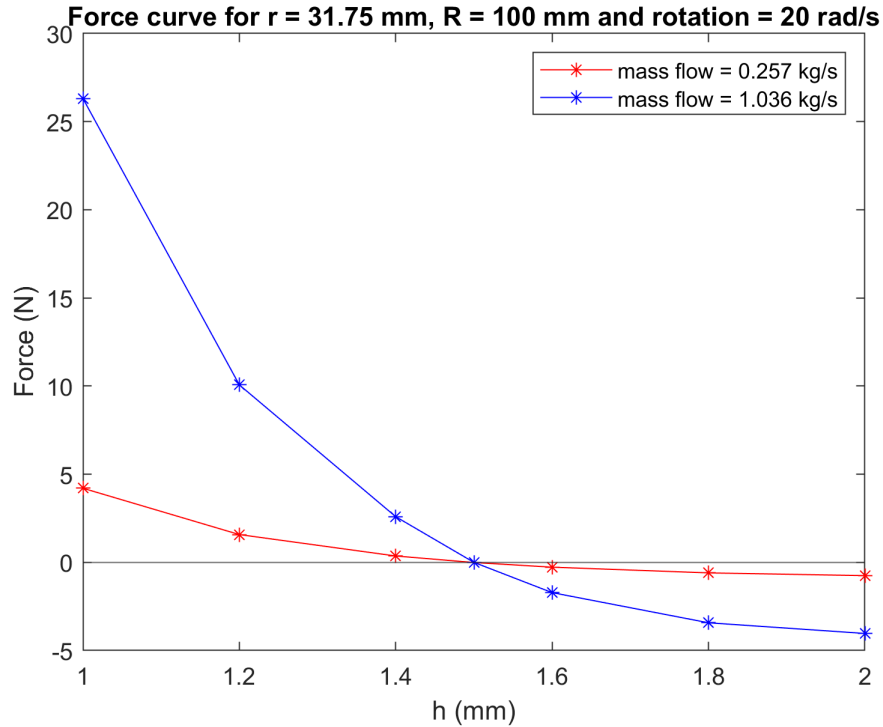


Figure 3.22 Force curve to obtain bi-stiffness equilibria for  $\omega = 20$  rad/s.

in the Figure 3.23, Figure 3.21 in Figure 3.24 and the variation of total pressure for the mass flow rate values plotted in the Figure 3.22 are shown in the Figure 3.25. The integral of the area for both the curves in Figure 3.23, Figure 3.24 and Figure 3.25 represents the normal force  $F$  generated on the workpiece and turns out to be zero for all the cases. The total pressure scales for the plots are drastically different because of the difference in mass flow rate values, and therefore, the plots have different y axis ranges for the different mass flow rate curves.

### 3.6 Rotating Bernoulli Pad: Energy Balance and Advantages

#### 3.6.1 Energy Balance

Consider the fluid control volume shown by the dotted lines in Figure 3.1. For this control volume, the energy balance equation will be comprised of the following terms:

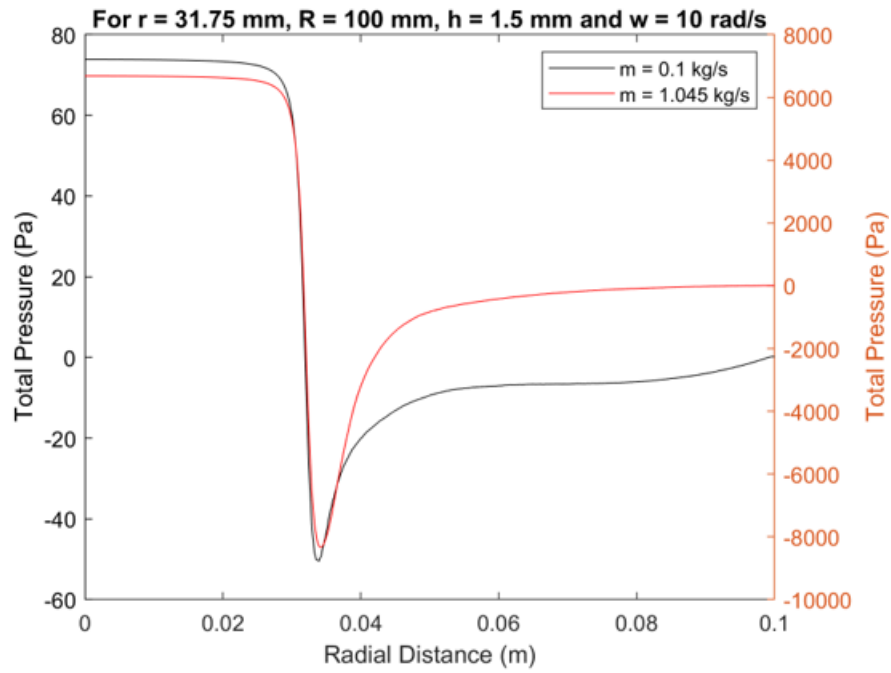


Figure 3.23 Variation of total pressure for  $\dot{m}_{in}$  in Figure 3.20.

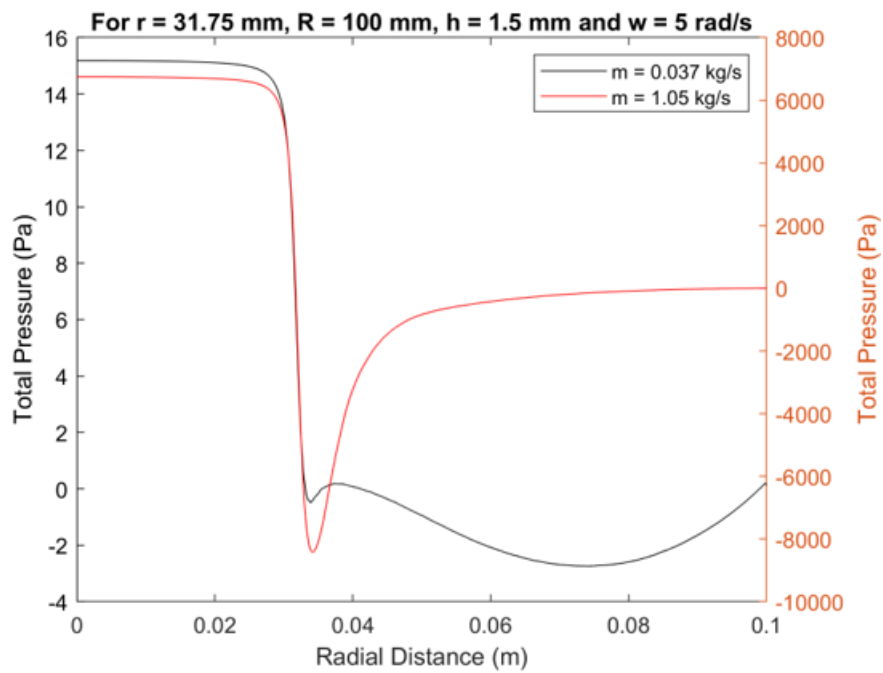


Figure 3.24 Variation of total pressure for  $\dot{m}_{in}$  in Figure 3.21.

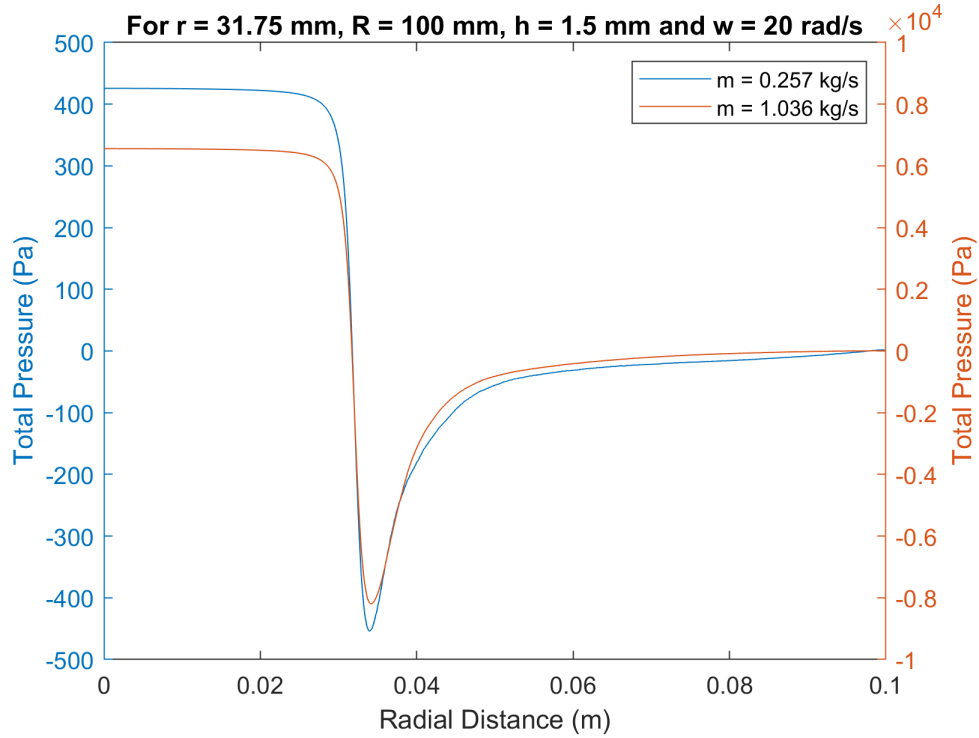


Figure 3.25 Variation of total pressure for  $\dot{m}_{in}$  in Figure 3.22.

1. Inlet Fluid Power: The power associated with the flow at the inlet is:

$$\dot{W}_{in} = \frac{\pi d^2}{4} p_{total} u_{in} \quad (3.2)$$

where  $p_{total}$  is the total pressure, comprised of the static and dynamic pressures. For the rotating pad and the rotating Bernoulli pad,  $p_{total}$  is given by the relations:

$$p_{total} = \begin{cases} \frac{1}{2} \rho u_{in}^2 & : \text{rotating pad} \\ \frac{1}{2} \rho u_{in}^2 + p_{in} & : \text{rotating Bernoulli pad} \end{cases} \quad (3.3)$$

2. Outlet Fluid Power: The power associated with the flow at the outlet is:

$$\dot{W}_{out} = \frac{\pi d^2}{8} \rho u_{out}^3, \quad u_{out} \triangleq \frac{d^2}{8Dh} u_{in} \quad (3.4)$$

where  $u_{out}$  is the velocity of the fluid at the outlet.

3. Mechanical Power: The mechanical power required to rotate the pad is given by the expression:

$$\dot{W}_{\text{mech}} = 2\pi\omega \int_{d/2}^{D/2} \mu \frac{\partial u_{\theta}}{\partial z} r^2 dr \quad (3.5)$$

4. Losses: The losses will be given by the expression:

$$\dot{W}_{\text{loss}} = \begin{cases} \dot{W}_{\text{mech}} - \dot{W}_{\text{in}} - \dot{W}_{\text{out}} & : \text{rotating pad} \\ \dot{W}_{\text{mech}} + \dot{W}_{\text{in}} - \dot{W}_{\text{out}} & : \text{rotating Bernoulli pad} \end{cases} \quad (3.6)$$

and can be explained as follows. For a rotating pad, the inlet fluid power  $\dot{W}_{\text{in}}$  is the result of the mechanical power expended in rotating the pad  $\dot{W}_{\text{mech}}$ . The losses are, therefore, computed by subtracting the inlet and outlet fluid power from the mechanical power added to the system. In contrast to the rotating pad, the rotating Bernoulli pad uses a prime mover to provide the inlet fluid power, and hence, the losses for the system are computed by subtracting the outlet fluid power from the sum of the mechanical power and inlet fluid power.

The losses are a measure of the shear stresses on the pad and the workpiece. In the present work, we focus on the shear stress on the workpiece - this is motivated by the application of non-contact shear-based grooming of biofouled surfaces Kamensky et al. (2020); Tomar et al. (2022).

### 3.6.1.1 Work analysis for zero static pressure at the inlet

The flow physics involving the rotating pad without an inlet pump (Static pressure = 0) is explained in detail in section 3 of this chapter. In the Figure 3.26, the corresponding power available at the outlet and the mechanical power required to rotate the pad are presented. The mass flow rate at the inlet getting sucked in increases with an increase in the angular speed of the pad. Since the pressure available at the inlet consists of the dynamic pressure, the power available at the inlet is very small in magnitude.

In the present control volume, the energy given to the system is in the form of mechanical energy to rotate the Bernoulli pad. The pad acts as a centrifugal pump and sucks the water from the inlet. Therefore, the work available at the inlet (dynamic pressure) is a byproduct of the mechanical

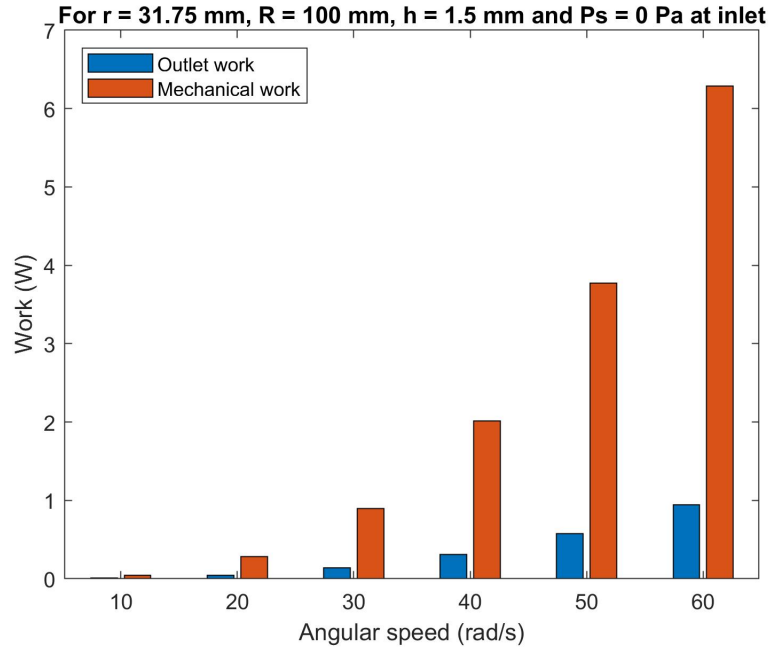


Figure 3.26 Outlet fluid power and mechanical power required for rotation

work. The losses in the system account for the rest of the energy provided to the system. These losses can be expressed as:

$$W_l = W_{mech} - (W_i + W_o)$$

### 3.6.1.2 Work analysis for mass flow rate = 0.5 kg/s

The addition of the inlet pump provides the static pressure head at the inlet. The combined effect of rotation and inlet fluid power provides a stable equilibrium to the configuration. Numerical simulations are carried out for mass flow rate,  $m = 0.5 \text{ kg/s}$ , and the work available at the inlet, mechanical work for the rotation, and the work available at the outlet are presented in the Figure 3.27.

In addition to the mechanical work for rotation, inlet fluid power is also added to the system. The contribution of mechanical power to the inlet fluid is negligible (refer to Table 3.2). Therefore, the losses in the system in this configuration are estimated as:

$$W_l = (W_{mech} + W_i) - W_o$$

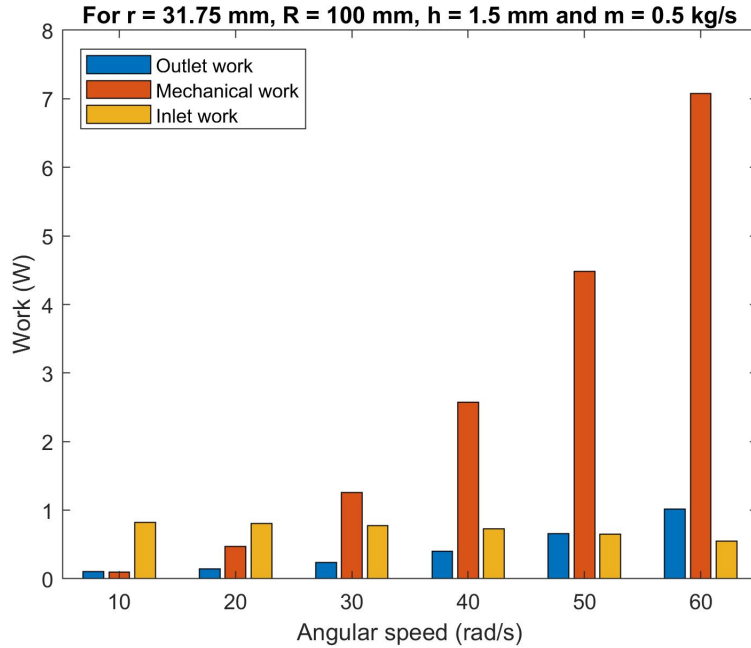


Figure 3.27 Inlet fluid power, outlet fluid power, and mechanical power required for rotation

$\omega$ (rad/s)	$\dot{m}$ (kg/s)	$W_{in}$ (W)	$W_o$ (W)	$W_{mech}$ (W)	Losses (W)
10	1	6.1394	0.7101	0.1571	5.5864
20	1	6.1237	0.7500	0.6780	6.0517
30	1	6.0882	0.8400	1.6800	6.9282
40	1	6.0335	0.9968	3.2840	8.3207
50	1	5.9558	1.2343	5.6000	10.3215
60	1	5.8515	1.5701	8.7456	13.027

Table 3.3 Work analysis for a mass flow rate of 1 kg/s

### 3.6.1.3 Work analysis for mass flow rate = 1 kg/s

Numerical simulations are carried out for mass flow rate,  $m = 1$  kg/s, and the work available at the inlet, mechanical work for the rotation, and the work available at the outlet are tabulated in Table 3.3. The inlet fluid power added to the system reduces with an increase in rotation. The contribution of mechanical power to the inlet fluid is again neglected. The losses in the system in this configuration are estimated as:

$$W_l = (W_{mech} + W_i) - W_o$$

$\dot{m}$ (kg/s)	$W_{in}$ (W)	$W_o$ (W)	$W_{mech}$ (W)
0.5	0.8304	0.0956	0
1	6.1447	0.7003	0

Table 3.4 Work analysis without rotation

### 3.6.1.4 Work analysis without rotation

To understand the computational domain without any rotation, numerical simulations are carried out with inlet fluid power alone. The work available at the inlet and the outlet is tabulated in the Table 3.4. This data from the table also gives a perspective about the magnitude of inlet fluid power added to the system when compared to the cases with a rotating pad.

### 3.6.2 Improvement in Normal Force and Maximum Shear Stress for a Given Inlet Fluid Power

The normal force  $F$  and the maximum shear stress  $\tau_{\max}$  are important for the application of biofouling mitigation through non-contact shear-based grooming. The normal force (attractive) will be used to adhere to the surface, and the maximum shear stress will define the grooming efficacy. The normal force  $F$  has been discussed at length in Sections 3.4 and 3.5; therefore, we present some discussion on the shear stress  $\tau$  on the workpiece before presenting the main results. For the same inlet fluid power  $\dot{W}_{in}$ , the radial variation of the shear stress on the workpiece is shown in Figure 3.28 for a Bernoulli pad with  $\omega = 0$  and  $\omega = 60$  rad/s.

The maximum shear stress on the workpiece  $\tau_{\max}$  is observed at a location close to the entrance of the gap (neck) of the Bernoulli pad - see the figure inset, which shows a magnified view of the region where the flow turns from the axial direction to the radial direction. The axial flow from the inlet strikes the workpiece and passes radially through the gap between the pad and the workpiece. At the neck, the sharp change in the flow direction does not allow the fluid to immediately attach to the pad surface; this produces a recirculating flow in the separation and reattachment regions Shi and Li (2016). This, in turn, reduces the effective area of the flow between the pad and the workpiece.

A sudden rise in velocity in this region is observed, which results in higher velocity gradients on the workpiece. Since the recirculating flow is located close to the neck, the location of the maximum

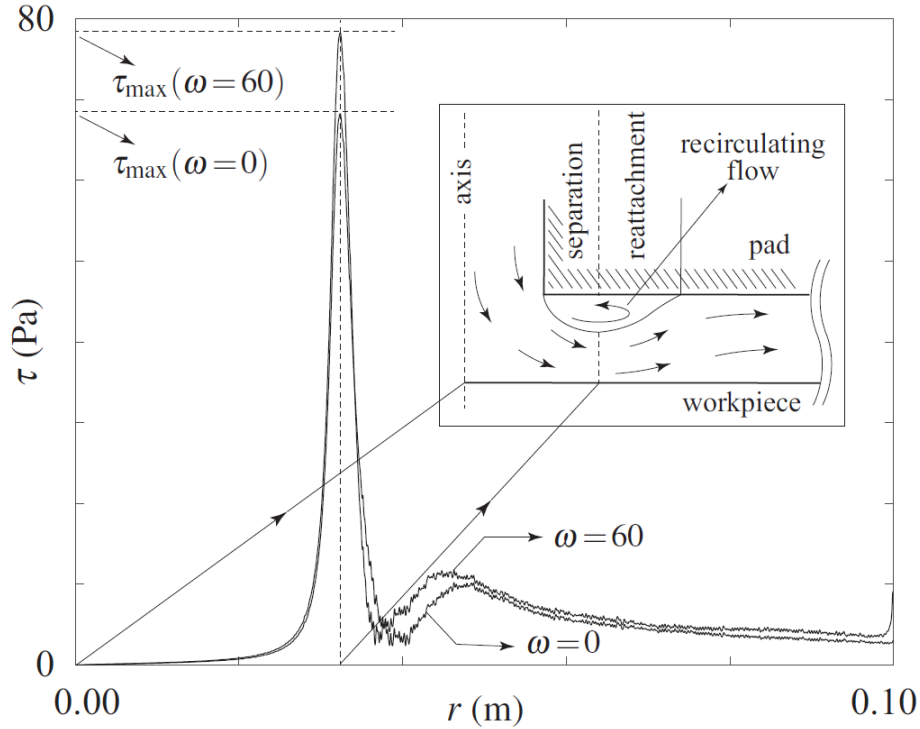


Figure 3.28 Radial variation of the shear stress  $\tau$  for the Bernoulli pad with parameters in Table 3.1, for  $\omega = 0$  and  $\omega = 60$  rad/s with the same  $\dot{W}_{in}$ : the maximum value  $\tau_{max}$  occurs below the recirculating flow, at the boundary of the separation and reattachment regions - see the figure inset, taken from Shi and Li (2016).

shear stress is independent of the speed of rotation. The velocity gradients below the recirculating flow are also proportional to the stagnation pressure associated with the fluid entering the gap. The addition of rotation affects the stagnation pressure and, therefore, changes the magnitude of shear stress on the workpiece.

We present simulation results to illustrate the effect of rotation on the normal force  $F$  and maximum shear stress  $\tau_{max}$  on the workpiece for the same level of inlet fluid power,  $\dot{W}_{in} \approx 0.83$  W - see Figure 3.29. For a given angular speed, the mass flow rate at the inlet is changed to make sure that the inlet fluid power remains the same: the mass flow rate is equal to  $\dot{m}_{in} = 0.5$  kg/s at  $\omega = 0$  rad/s and  $\dot{m}_{in} = 0.555$  kg/s at  $\omega = 60$  rad/s. The increase in rotational speed from  $\omega = 0$  rad/s to  $\omega = 60$  rad/s results in a 14.93% rise in the value of the maximum shear stress; the normal force changes from +1.4037 N (repulsive) to -6.6827 N (attractive). The increase in the maximum shear stress value will result in better grooming of the surface, and an increase in the attractive normal

force will enable the Bernoulli pad to adhere strongly to the workpiece.

### 3.7 Conclusion

A standard non-rotating Bernoulli pad uses a prime mover, such as a blower or pump, to produce its radial outflow. The axial jet provided by the prime mover at  $r \leq d/2$  is turned by the workpiece to move the flow in the radial direction. For a given mass flow rate, the Bernoulli pad produces a stable equilibrium configuration within a certain range of gap heights. In this configuration, which is characterized by positive stiffness of the flow field, the repulsive force between the workpiece and the pad due to the high pressure of the axial jet and the attractive force due to the subatmospheric pressure in the region  $d/2 \leq r \leq D/2$ , balance each other. The equilibrium configuration is associated with a specific mass flow rate, and a change in the mass flow rate causes the equilibrium gap height to change.

A rotating pad, in contrast, does not use a separate prime mover. The shear imposed by the

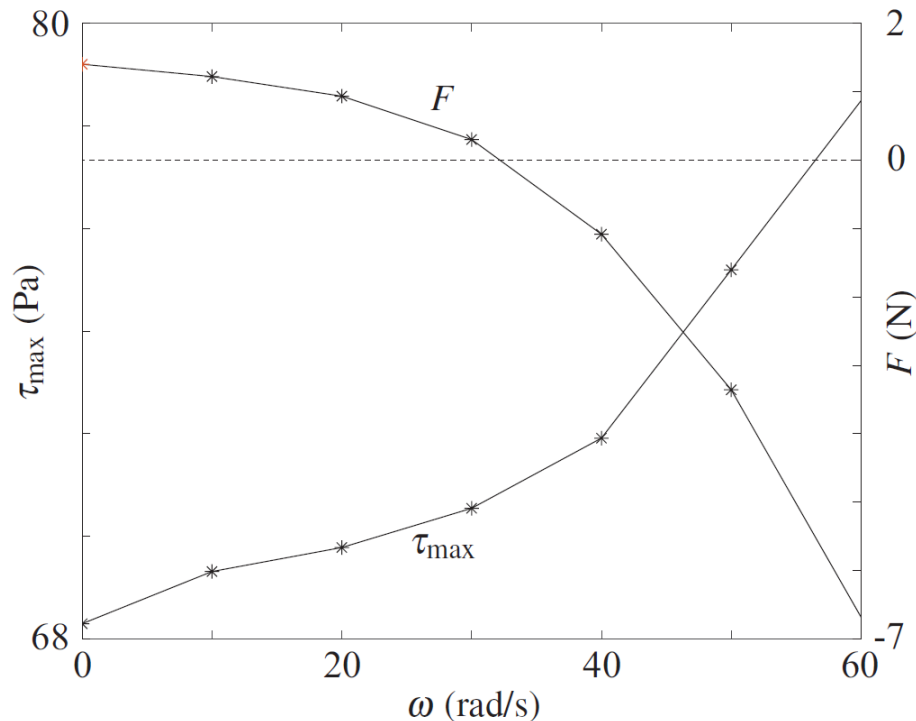


Figure 3.29 Variation in the normal force and maximum shear stress on the workpiece with angular speed for a fixed inlet fluid power  $\dot{W}_{\text{in}} \approx 0.83$  W; this power results in a mass flow rate of  $\dot{m}_{\text{in}} = 0.5$  kg/s at  $\omega = 0$  rad/s.

rotating pad drives a tangential flow within the gap, which is accelerated in the radial direction. The mass flux produced by this radial flow enters the flow field through the inlet; the rotating pad is its own prime mover, essentially a bladeless centrifugal pump. Because the inlet velocity is small compared to the tangential velocity, the pressure of the axial jet is small, and this flow field produces a strong, attractive force between the pad and the workpiece. Unlike the standard non-rotating Bernoulli pad, the flow field produced by the rotating pad has negative stiffness and hence no stable equilibrium configuration, meaning that the attractive force between the pad and the workpiece becomes stronger as they get closer.

A rotating Bernoulli pad uses a combination of fluid power provided by a prime-mover and mechanical power for pad rotation. Similar to the standard non-rotating Bernoulli pad, this system also exhibits stable equilibrium configurations. A unique characteristic of this system is that a given stable equilibrium configuration is associated with two different stiffnesses corresponding to two different mass flow rates for a given speed of rotation. The standard non-rotating Bernoulli pad is a special case of the rotating Bernoulli pad and also exhibits this property, not reported in the literature heretofore.

The rotating flow in the gap adds additional normal force between the pad and workpiece and drives a small amount of additional mass flux at the same inlet pressure. This allows the balance between the impinging pressure of the axial jet and low pressure within the gap to balance at an additional value of mass flow rate. The pad rotation also increases the shear experienced by the workpiece at constant inlet power, both by increasing the mass flux and by providing a tangential velocity component. This additional shear, which comes at the cost of additional mechanical power, can be used to improve grooming efficacy in biofouling mitigation.

For a specific pad with the same inlet fluid power, an increase in the rotational speed by 60 rad/s resulted in the maximum wall shear stress increasing by  $\approx 15\%$  and the normal force changing from +1.4 N (repulsive) to -6.6 N (attractive). This work is intended as an overview of some of the many rich features of this flow field; we expect that many of these results can be extended and generalized in future work.

## CHAPTER 4

### WALL SHEAR MEASUREMENT: HOT-FILM ANEMOMETRY AND MODEL TESTING

#### 4.1 Introduction

A large part of this chapter is submitted for publication as an article in the Experiments in Fluid journal. In Chapter 2 and 3, we have obtained an estimation of the wall shear stress generated by the Bernoulli pad on the opposing workpiece.

The abrupt change in the flow direction introduces separation and recirculation near the neck of the pad Shi and Li (2016). The separation and constriction of the flow results in a large magnitude of shear stresses on the workpiece, which is an important parameter for the application of bio-fouling mitigation. In our previous work Tomar et al. (2022), we have used computational fluid dynamics simulations to develop a better understanding of the flow physics, including the location and magnitude of the maximum shear stress. It was found that the magnitude of wall shear stress is maximum at the belly of the recirculation region. Resolving the region of flow separation is computationally expensive, which makes it challenging to predict the wall shear stress accurately. The numerical results need validation, and for the first time in this work, a constant temperature hot-film anemometer is used with water as the working fluid to measure the wall shear stress.

Over the last few decades, various methods for wall shear stress measurements have been developed and reviewed in the literature Winter (1979); Fernholz et al. (1996); Sheplak et al. (2006). The popular methods among researchers include the use of laser Doppler anemometer, floating element sensor, Preston or Stanton tubes, hot wire or hot-film, etc. Hot-film sensors have been used to detect flow separation and detection of transition from laminar to turbulent flow - see Bellhouse and Schultz (1966); Owen (1970); Jiang et al. (2000), for example. In the present work, we use a flush-mounted hot-film sensor for the measurement of wall shear stress generated by a Bernoulli pad.

The main principle behind this technique is to correlate heat transfer from the sensor with wall shear stress. To this end, the sensor needs to be calibrated under known wall shear conditions. There are two main challenges associated with these experiments. First, velocity gradients are

measured at the wall using typical wall shear measurement techniques. The measurement of these velocity gradients is not possible since the sensor is a flush-mounted sensor, and hence, the sensor has to be calibrated against the wall shear stress itself. Second, sensor measurements are highly dependent on ambient conditions, and therefore, calibration must be performed in situ.

Experimental investigations with Bernoulli pads have been reported in the literature. Li and Kagawa Li and Kagawa (2014), for example, conducted experiments to understand the various factors that affect the wall normal forces. A majority of the investigations in the literature have focused on wall-normal forces and used air as the working fluid. To the best of our knowledge, the only work with water as the working fluid was reported by Kamensky Kamensky (2020); in this work, Particle Tracking Velocimetry (PTV) experiments were conducted to measure the velocity components of the flow field. PTV experiments do not provide reliable measurements close to the wall and cannot be used to accurately measure wall shear stress. Hence, the wall shear measurements presented in this work fill an important gap in the literature.

This chapter is organized as follows. A brief review of the working principle of hot-film sensors is provided in Section 4.2. The calibration of the hot-film sensor is carried out using fully-developed channel flow; an analytical solution for wall shear in channel flow is presented in Section 4.2 and the procedure for calibration of the hot-film sensor is presented in Section 4.3. The experimental setup for wall shear measurements is described in Section 4.4. Section 4.5 provides experimental results and compares them with results obtained from numerical simulations. Concluding remarks are provided in Section 4.6.

## **4.2 Background**

### **4.2.1 Analytical solution for wall shear in channel flow**

For two-dimensional steady-state fully developed channel flow - see Figure 4.1, the Navier-Stokes equation for the streamwise velocity becomes:

$$\mu \frac{d^2 u}{dy^2} = \frac{dp}{dx}$$

where  $p = p(x)$  is the pressure,  $u = u(y)$  is the streamwise velocity, and  $\mu$  denotes the dynamic

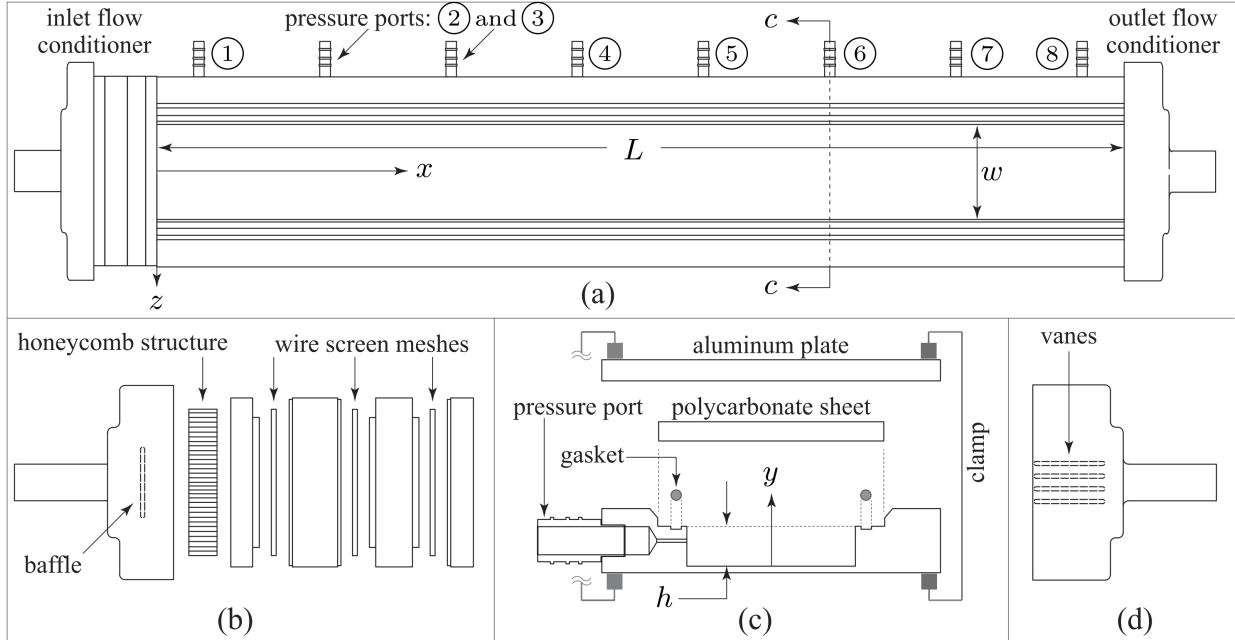


Figure 4.1 Channel setup used for calibration of the hot-film sensor; figures are not drawn to scale: (a) top-view of the channel showing the eight pressure ports, (b) exploded view of the inlet flow conditioner, (c) exploded view of section c-c of channel with gasket, polycarbonate sheet, aluminum plate, and clamps (d) outlet flow conditioner showing internal vanes.

viscosity. On integrating the above equation with respect to  $y$  once, and substituting the symmetry condition  $du/dy = 0$  at  $y = h/2$ , we get:

$$\mu \frac{du}{dy} = \left( y - \frac{h}{2} \right) \frac{dp}{dx} \quad (4.1)$$

Note that  $h$  is the channel's height. This result does not assume any particular flow regime, laminar or turbulent. From the above result, the shear stress  $\tau$  can be written as:

$$\tau \triangleq \mu \frac{du}{dy} = \left( y - \frac{h}{2} \right) \frac{dp}{dx}$$

At the wall, where  $y = 0$ , the wall shear stress  $\tau_w$  is then given by:

$$\tau_w = -\frac{h}{2} \frac{dp}{dx} \quad (4.2)$$

Therefore, the wall shear stress in channel flow can be determined by measuring the pressure gradient.

#### 4.2.2 Working principle of hot-film anemometry

Hot-film anemometry is used to measure the velocity and turbulence properties of fluid flows. The hot-film sensor used in our experiments is shown in Figure 4.2. The H-shaped film at the tip of the sensor is a very thin electrical resistor. The main principle behind a hot-film anemometer is that the heat generated by electric current through the film is dissipated via thermal convection. The heat transfer rate from the film into the fluid varies with flow velocity according to King's law (King, 1914):

$$q_{\text{conv}} = a + bu^n, \quad (4.3)$$

and the heat generated by electric current is:

$$q_{\text{gen}} = \frac{E_a^2}{R_f} \quad (4.4)$$

In (4.3) and (4.4),  $a$ ,  $b$ , and  $n$  are constants,  $u$  is the characteristic velocity around the hot-film,  $E_a$  is the voltage applied across the film, and  $R_f$  is the film's electrical resistance. To satisfy energy conservation,  $q_{\text{conv}} = q_{\text{gen}}$ . Hence, from equations (4.3) and (4.4):

$$E_a^2 = aR_f + (bR_f)u^n \quad (4.5)$$

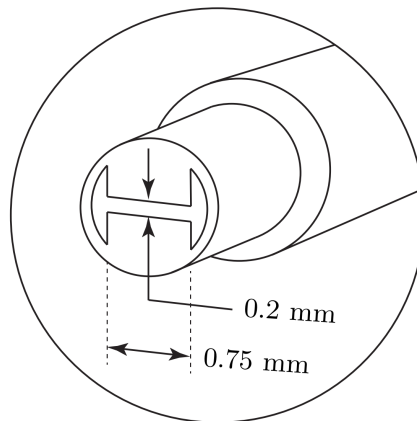


Figure 4.2 A schematic of the hot-film sensor 55R46 by Dantec Dynamics Dantec Dynamics (2023).

Since the hot-film anemometer will be calibrated with fully developed channel flow, (4.1) can be integrated with respect to  $y$ , using the non-slip boundary condition  $u = 0$  at  $y = 0$ , to obtain an expression for  $u$ :

$$\mu u = (y^2 - hy) \frac{1}{2} \frac{dp}{dx}$$

Very near the wall, for  $y = \delta_{nw} \ll 1$ , the linear term dominates and the second order term becomes negligible. In turbulent boundary layers,  $\delta_{nw}$  is equal or less than the thickness of the laminar sublayer. Under these conditions, the last result simplifies to:

$$\mu u \approx -\frac{dp}{dx} \frac{h}{2} \delta_l$$

From (4.2), we get:

$$u \approx \frac{\tau_w}{\mu} \delta_{nw} \quad (4.6)$$

Using (4.6), (4.5) can now be expressed in terms of the wall shear stress:

$$E_a^2 = aR_f + bR_f \left( \frac{\delta_{nw}}{\mu} \right)^n \tau_w^n \quad (4.7)$$

$R_f$  is maintained constant when the sensor is operated with a Constant Temperature Anemometer (CTA). To this end, the hot-film is implemented within a Wheatstone bridge to constantly monitor and correct changes in its resistance due to cooling. The main compensation is achieved by changing the electric current through the film in order to maintaining its temperature constant. Therefore, the coefficients of equation (4.7) can be absorbed into two calibration constants as follows:

$$E_a^2 = A + B\tau_w^n, \quad (4.8)$$

These constants are determined by correlating the voltage output of the sensor with known wall shear stress in fully-developed channel flow.

Though (4.8) was obtained without assuming any specific flow regime, heat transfer characteristics in laminar flows differ significantly from those of turbulent flows. In laminar flows, heat

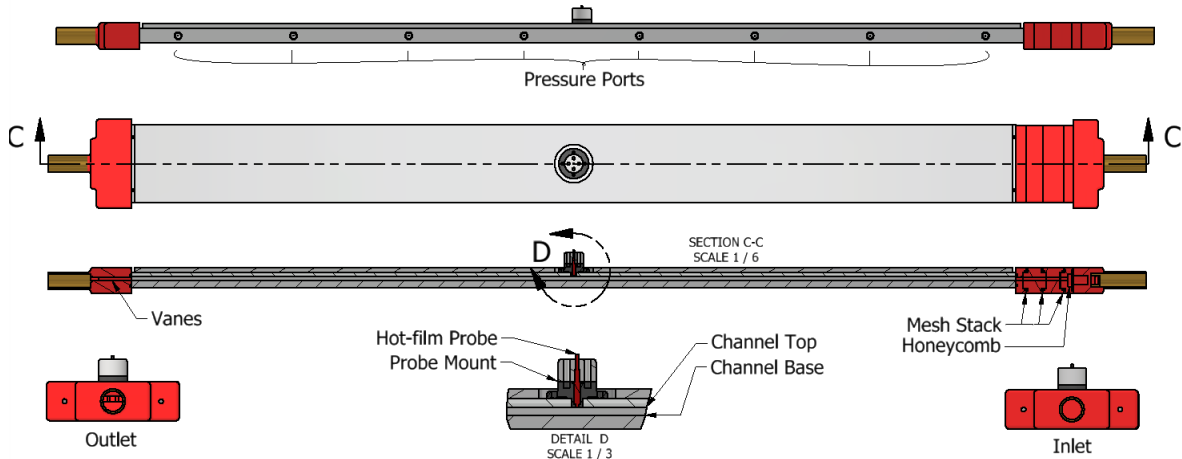


Figure 4.3 A CAD describing the channel used for hot-film probe calibration

transfer is diffusion-dominated, whereas it is advection-dominated in turbulent flows because of transversal motions outside of the laminar sublayer. Therefore, the calibration constants of (4.8) should be different for laminar and turbulent flows.

### 4.3 Calibration of Hot-Film Sensor

#### 4.3.1 Design of channel

The channel used for calibration of the hot-film sensor is motivated by prior work reported in the literature Sun et al. (2018). A schematic of the channel is shown in Figure 4.1(a) and a sectional view through a pressure port is shown in Figure 4.1(c). The channel was fabricated using Aluminum and its cross-section ( $w = 50$  mm,  $h = 5$  mm) was chosen to yield a Reynolds number of  $Re = 10,000$  with the available pump. A CAD model is presented in the Figure 4.3.

The length of the channel was chosen to be  $L = 1,200$  mm to ensure that the flow reaches a state of fully-developed flow under smooth-wall conditions, and remains so for a significant portion of the channel. The top of the channel is covered with a clear polycarbonate sheet and leakage is prevented through the use of a gasket along the length of the channel. An aluminum plate is placed over the polycarbonate sheet and clamps are used to apply uniform pressure on the gasket along the length of the channel to make it leak proof - see Figure 4.1(c) and Figure 4.5(a).

A submersible utility pump was used to circulate water through the channel. The flow rate is controlled with a gate valve installed upstream of the channel's inlet. The flow is conditioned at

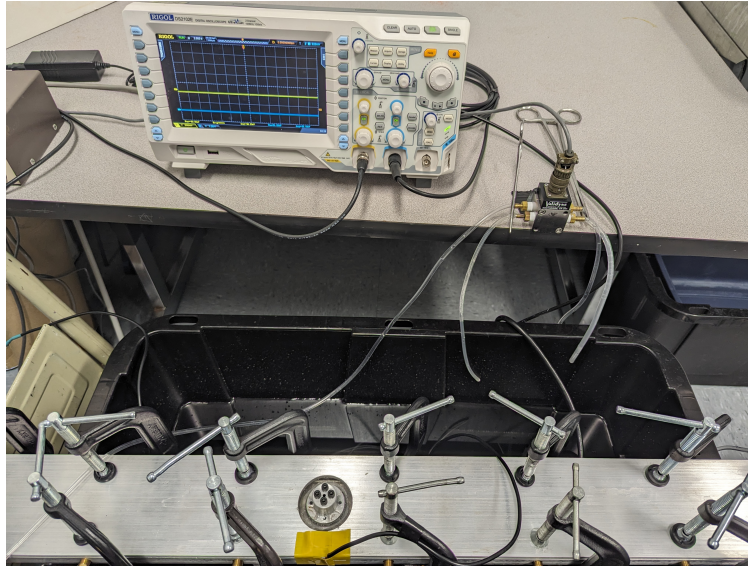


Figure 4.4 Pressure measurement using a DP15 differential pressure transducer

the inlet of the channel with a series of baffles, followed by a honeycomb, and then a series of three meshes of decreasing hole size - see Figure 4.1(b) and Figure 4.5(b). To reduce the developing length, the boundary layer is tripped with a coarse-grit sand paper strip at the inlet of the channel. The outlet of the channel is connected to a flow conditioner with four internal vanes to minimize

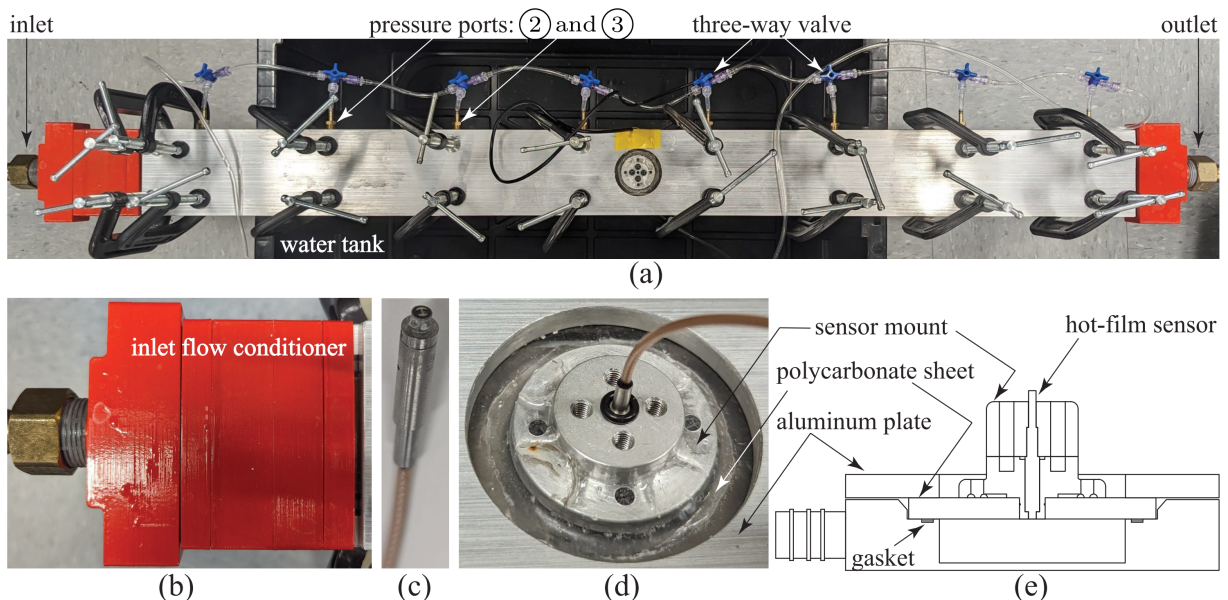


Figure 4.5 Assembled view of the channel setup in Figure 4.1: (a) top-view of the channel showing sensor mount (without sensor) and eight pressure ports (see Figure 4.1) connected via three-way valves, (b) inlet flow conditioner, (c) hot-film sensor, (d) magnified view of sensor mount with sensor, (e) sectional view of channel setup through the sensor mount and sensor.

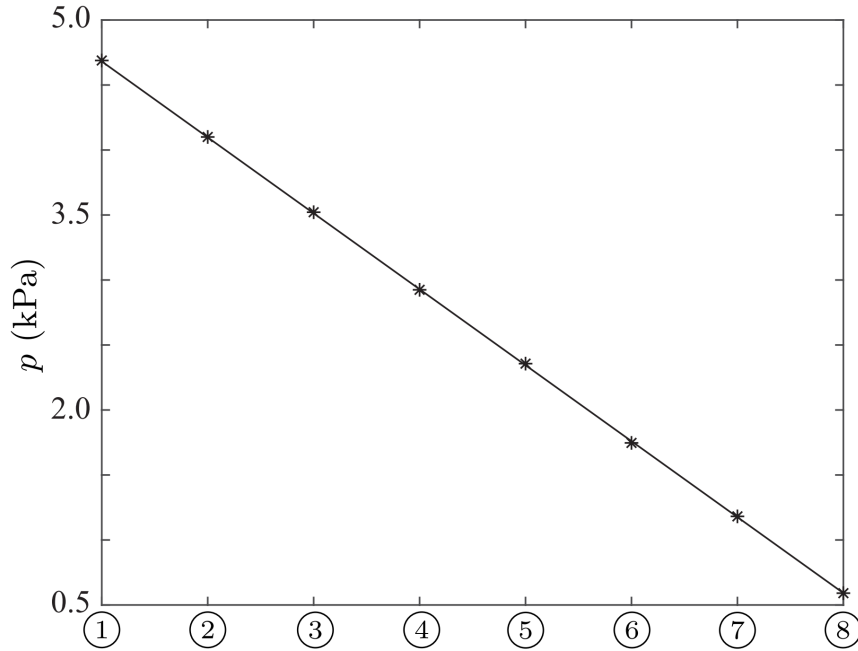


Figure 4.6 Pressure at the eight different ports of the channel (see Figure 4.1), computed based on pressure differential measurements relative to port ① and assignment of an arbitrary pressure to port ⑧. Note that the straight line fit was obtained by using the data from ports ④ though ⑧.

end-effects - see Figure 4.1(d).

To measure pressure along the channel, eight pressure taps are placed on the side of the channel along its length. The ports are drilled with a size of 0.8 mm. The ports are connected by a three-way valve - see Figure 4.5(a), to a DP15 differential pressure transducer (a product of Validyne Engineering VALIDYNE Engineering (2022)), as shown in Figure 4.4. The pressure differential between ports ② through ⑧ relative to ① are recorded at steady state; the data is then used to compute the pressure at all the ports by assigning an arbitrary pressure to port ⑧ - see Figure 4.6. The plot indicates that fully developed flow is achieved early and well ahead of port ①. The hot-film sensor can be mounted anywhere along the length of the channel in which the pressure drop exhibits a linear behavior, because that is the region where the flow is fully developed. We chose to mount the sensor, shown in Figure 4.5(c), between ports ④ and ⑤ on the polycarbonate sheet - see Figure 4.1(a), Figure 4.5(a) and Figure 4.5(d). A sectional view of the assembled channel setup through the sensor mount and sensor is shown in Figure 4.5(e).

### 4.3.2 Calibration procedure

The hot-film sensor 55R46, shown in Figure 4.2 and Figure 4.5(c), was calibrated using the constant temperature anemometer MiniCTA 54T42, also a product of Dantec Dynamics Dantec Dynamics (2023). The sensor is used with water as the working fluid and therefore the jumpers inside the anemometer were adjusted according to the desired value of overheat and sensor resistance. The sensor is flush-mounted on top of the polycarbonate sheet between pressure ports ④ and ⑤, where the flow is fully developed - see our discussion in Section 4.3.1.

The calibration of the sensor was performed using 21 different flow rates through the channel; a gate valve was installed between the prime mover and the inlet of the channel to control the flow rate. For each flow rate, the pressure transducer and hot-film sensor measurements (voltages) were recorded. The pressure measurement (voltage) provides the pressure drop between ports ④ and ⑤; transducer calibration data is used to express it in Pa and the wall shear stress  $\tau_w$  is then computed using Eq.(4.2). The variation of the square of the hot-film sensor voltage ( $E_a^2$ ) with the wall shear stress  $\tau_w$  is plotted in Figure 4.7 with the objective of computing the calibration coefficients in Eq.(4.8). It can be seen that the wall shear stress increases monotonically with increase in the mass flow rate. Also, the variation of  $E_a^2$  with  $\tau_w$  depicts three distinct behaviors corresponding to three distinct flow regimes: turbulent, critical and laminar. In the laminar and turbulent regimes, the data points show a concave downward trend with increase in wall shear stress; the trend is reversed and is concave upward in the critical regime.

The data points corresponding to the laminar and turbulent regimes are used to find a linear fit between  $E_a^2$  and  $\tau_w^n$ , where the value of the exponent  $n$  should lie in the range [0.1,0.5] Cameron Tropea (2007). A linear fit is found by choosing  $n = 0.4$  for the data in the laminar regime and  $n = 0.2$  for the data in the turbulent regime. The plots are provided in Figure 4.8 and the calibration coefficients in Eq.(4.8) are provided in Table 4.1; these coefficient were obtained with an  $R^2$  value of 0.99 and a confidence level of 95%. The calibration coefficients in Table 4.1 will be used to measure the wall shear stress generated by a Bernoulli pad in Section 4.5.

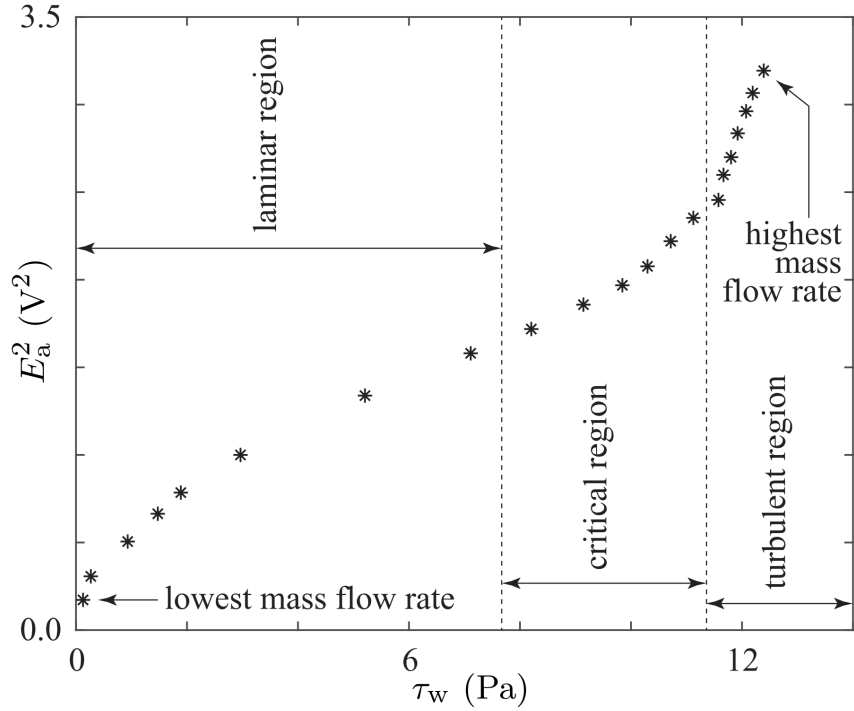


Figure 4.7 Calibration data showing the variation of  $E_a^2$  with  $\tau_w$

Table 4.1 Calibration coefficients and exponent for laminar and turbulent flow regimes

Flow regime	$A$	$B$	$n$
Laminar	-0.216	0.798	0.4
Turbulent	-50.86	32.70	0.2

#### 4.4 Bernoulli Pad Experimental Setup

An experimental setup was developed to measure the wall shear stress generated by a Bernoulli pad. An important component of the setup is the Bernoulli pad assembly, comprised of the stem, pad, and flow conditioning section - see Figure 4.9(a) and (b). The stem is a tube with an inside diameter of  $d = 25.4$  mm (1.0 in), an outside diameter of 31.75 mm (1.25 in), and a length of 88.9 mm (3.5 in). The pad is a circular, flat plate with a diameter of  $D = 203.2$  mm (8.0 in) and a thickness of 6.35 mm (0.25 in). A 25.4 mm (1.0 in) hole is located at the center of the pad along with a 31.75 mm (1.25 in) counterbore to 75% depth in the pad. The stem interfaces with the pad in the counterbore such that there are negligible steps for the fluid to encounter. Cast acrylic was selected as the material for both the stem and the pad; its rigidity is adequate for the current

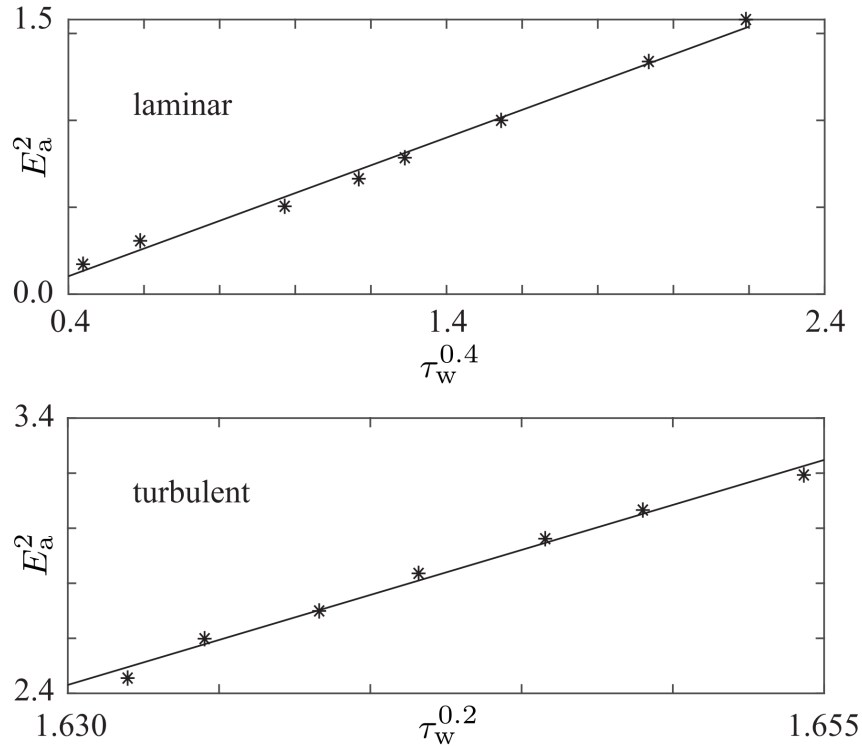


Figure 4.8 Linear calibration curves for laminar and turbulent regimes

purpose and its surface roughness is very low. In particular, polished acrylic sheets typically exhibit a surface roughness within  $0.14 \mu\text{m} < Ra < 0.23 \mu\text{m}$  S et al. (2011), or equivalently,  $0.62 \mu\text{m} < Rz < 0.89 \mu\text{m}$  Stähli (2013). Here, Ra is the arithmetic mean of the deviation from the roughness centerline, and Rz is the mean roughness depth.

The flow conditioning section is used to obtain a low-turbulence-intensity and top-hat velocity profile at the inlet of the stem. It is comprised of the following elements from upstream to downstream order: an inlet piece, a baffle that breaks down the incoming pipe flow, a honeycomb, three wire meshes of decreasing hole size, and a flow contraction - see Figure 4.9(b). A cubic equation was used to design the flow contraction profile Hussain and Ramjee (1976). The components of the flow conditioning section were mated with the stem in a similar fashion as the stem-pad interface to avoid disturbances in the flow. Except the inlet, baffle, honeycomb, and wire meshes, the materials of the components of the flow conditioning section were chosen as cast acrylic and polyurethane-coated 3D prints (fabricated with PLA - polylactic acid) for smooth surface finishes.

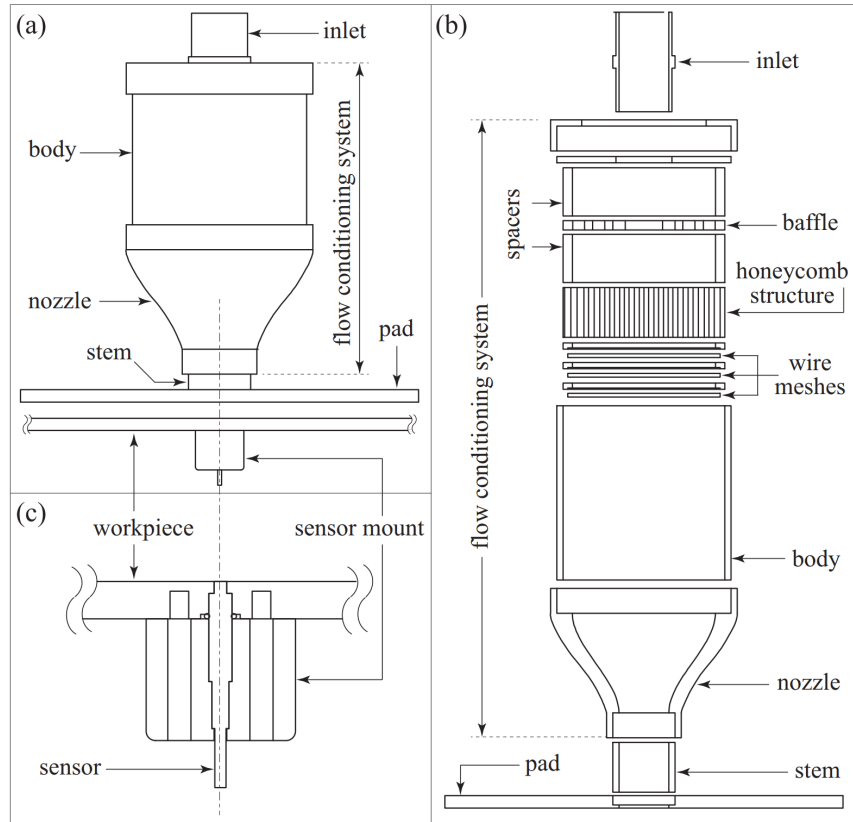


Figure 4.9 (a) Bernoulli pad assembly shown in its nominal configuration over the workpiece (b) exploded view of Bernoulli pad assembly (c) sectional view of flush-mounted sensor in workpiece.

The primary components of the experimental setup are: workpiece, sensor mount (a detailed CAD and a view below the workpiece in Bernoulli pad assembly is provided in Figure 4.10 and Figure 4.11 respectively), linear stage, Bernoulli pad assembly mount and frame. An assembled view of these components, which we will refer to as the Shear Test Station (STS), is shown in Figure 4.12. A rectangular, flat plate of 7075-T6 aluminum was selected as the workpiece because of its rigidity and electrical conductivity. It has dimensions of 406.4 mm  $\times$  304.8 mm  $\times$  6.35 mm, and the surface of the workpiece was sanded and polished to reduce its surface roughness. This process typically results in roughness levels in the range of  $0.1 \mu\text{m} < Ra < 0.4 \mu\text{m}$  or  $0.5 \mu\text{m} < Rz < 1.4 \mu\text{m}$ . Located at the center of the workpiece width and 254 mm down its length is a counterbored hole that allows the hot-film sensor to mate with the workpiece such that the sensing surface of the sensor is flush with the workpiece - see Figure 4.9(c). A grounding

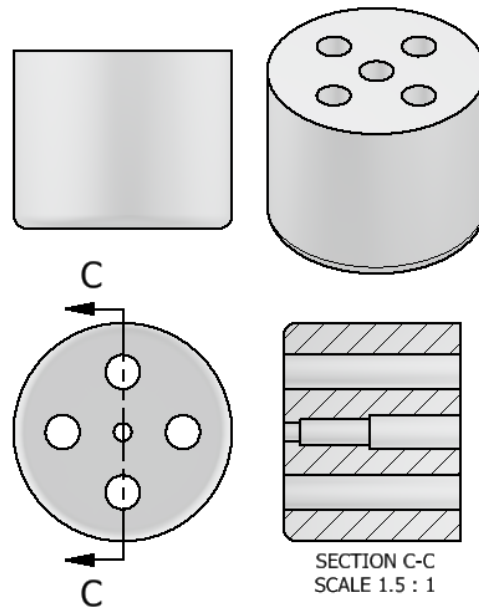


Figure 4.10 A detailed cad of the sensor mount installed in the Bernoulli pad assembly



Figure 4.11 View of the sensor mount installed below the Bernoulli pad assembly

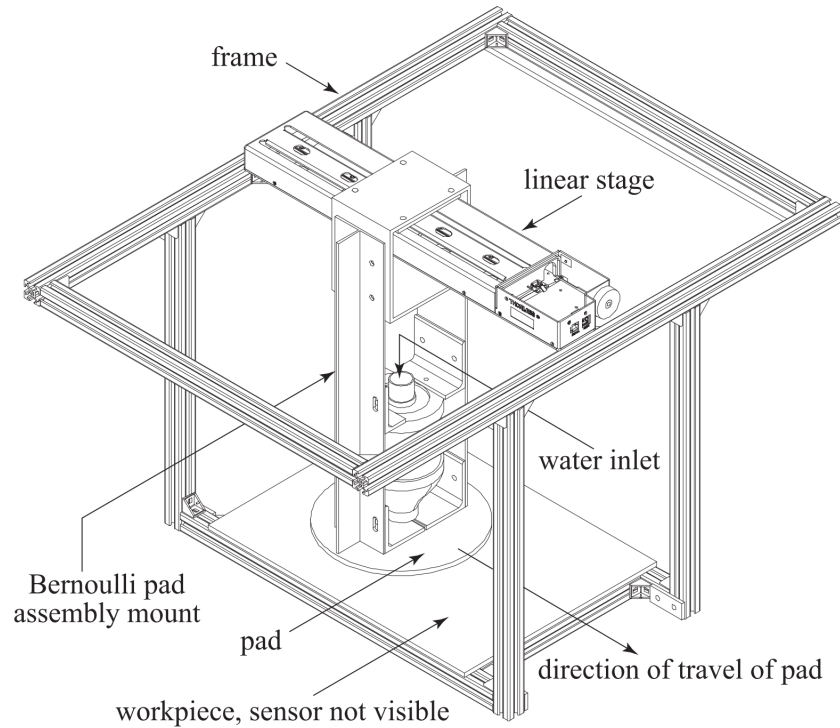


Figure 4.12 An assembled view of the Shear Test Station (STS), comprised of the Bernoulli pad assembly mount, workpiece and linear stage.

lead necessary for the hot-film sensor was permanently fastened to one of the plate's vertical faces. Blind holes allow the sensor mount to be secured to the underside of the workpiece as shown in Figure 4.13. The probe mount in Figure 4.13, contains steps in its internal geometry that constrain the hot-film probe when it is fastened to the underside of the work surface.

A LTS300 linear translation stage manufactured by THORLABS (THORLABS (2023)) was used to move the Bernoulli pad over the length of the workpiece such that the hot-film sensor can measure the wall shear stress along the radial direction. The LTS300 has an absolute accuracy of  $50 \mu\text{m}$  and a repeatability of  $2 \mu\text{m}$ . The Bernoulli pad assembly mount, shown in Figure 4.12, is a series of structural aluminum members that interface the Bernoulli pad assembly in Figure 4.9(a) to the linear stage. The joints of the Bernoulli pad assembly mount are comprised of slots and threaded fasteners that allow for setting a uniform gap between the pad and the workpiece. Structural aluminum extrusions form a frame that allows the workpiece to be positioned below the Bernoulli pad assembly mount and ensure that the pad and the workpiece remain parallel with

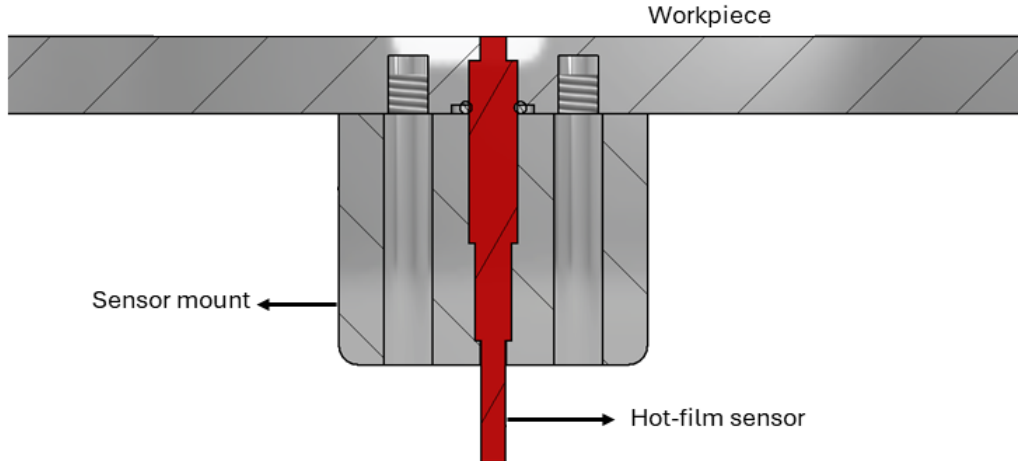


Figure 4.13 The work surface, hot-film probe, and probe mount

travel of the linear stage. The fluid power assembly consists of a 250 W submersible pump, rubber hoses, and a gate valve for flow rate control.

## 4.5 Wall Shear Stress Measurement

### 4.5.1 Procedure

The gap height between the pad and the workpiece was chosen to be  $H = 1.3$  mm for our experiments. Shims were placed in the gap to ensure that the gap height was uniform; they were removed after ensuring uniform desired gap height. The Shear Test Station (STS) was then placed into a water tank with dimensions of 2120 mm  $\times$  749 mm  $\times$  762 mm - see Figure 4.14. The frame suspended the workpiece in the center of the tank footprint and 356 mm from the bottom. The dimensions of the tank and the location of the workpiece were chosen to ensure that the radial outflow between the pad and workpiece was not affected by the water splashing from the tank walls. Shims were placed between the frame and tank to level the STS before it was secured to the tank with clamps. The fluid power assembly was connected, and the mass flow rate was set to  $\dot{m} = 0.046$  kg/s. The mass flow rate was chosen such that the maximum wall shear stress was within the range of the calibration setup. Sufficient water was added to the tank without submerging the workpiece and the water was allowed to adjust to the ambient temperature (17.25° C) before data collection began. The density and viscosity of water at this temperature are  $\rho = 998.87$  kg/m<sup>3</sup> and

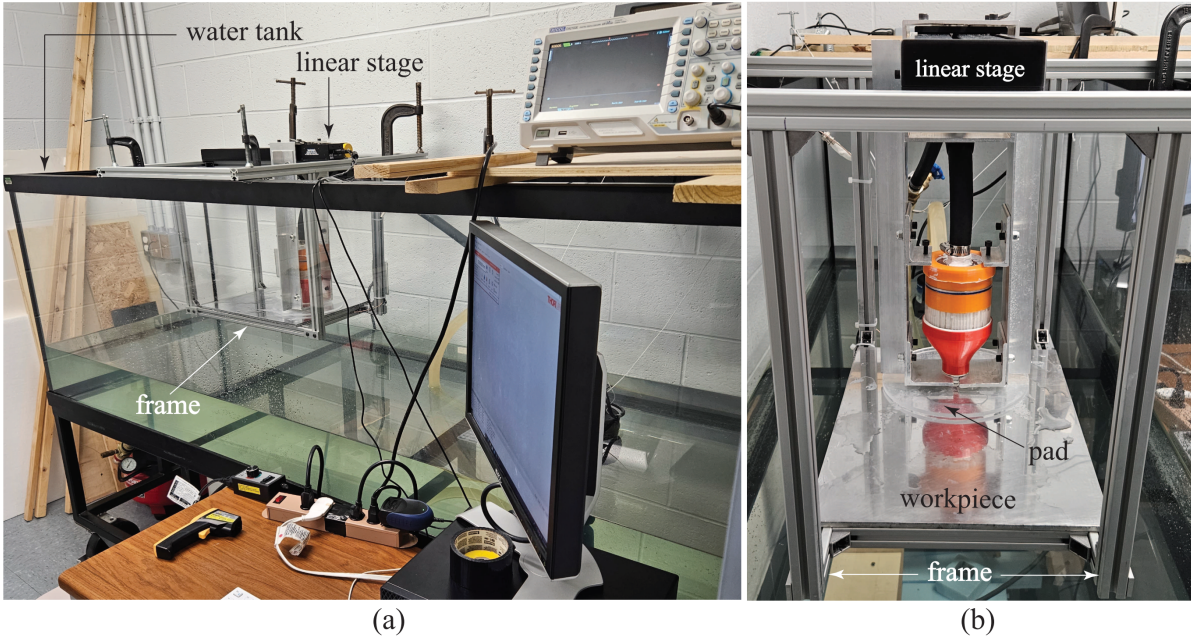


Figure 4.14 (a) A perspective view of the experimental setup (b) a side view showing the STS

$\mu = 0.001073 \text{ Pa s}$ .

The pump was powered on, and the system was allowed to reach steady-state. The linear stage was used to move the Bernoulli pad from its nominal position, shown in Figure 4.9(a), in steps with an average size of 5 mm, which is approximately twice the diameter of the hot-film sensor. The step size was reduced to 1.0-2.0 mm close to the neck of the Bernoulli pad, where large variations in the shear stress are expected. The total distance of travel was approximately  $\ell = 83.0 \text{ mm}$ ; this ensured that the sensor was never exposed to air. After each step, the sensor was powered on, and the hot-film sensor output was obtained using an oscilloscope. After recording the data, the sensor was powered off to avoid unnecessary heating. A view of the Bernoulli pad assembly during the data collection is provided in the Figure 4.15.

The voltage outputs from the hot-film sensor were first corrected for temperature difference between calibration and wall shear stress measurement conditions. In particular, we used the following relation for temperature correction:

$$E_{\text{corr}} = \left( \frac{T_f - T_0}{T_f - T_a} \right)^{0.5} E_a$$

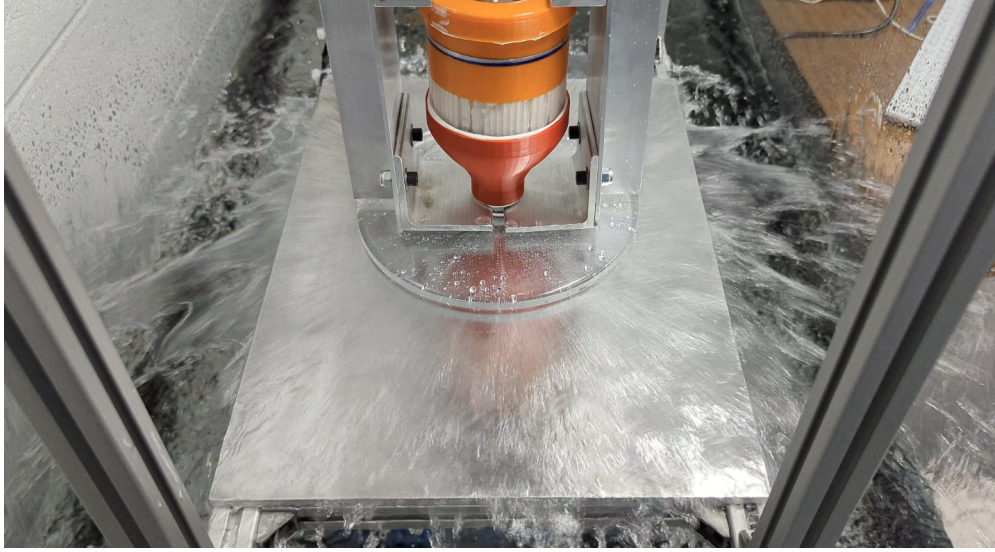


Figure 4.15 A side view showing the STS during the data collection process

where,  $E_{\text{corr}}$  is the corrected voltage,  $T_0 = 25.49^\circ\text{C}$  is the water temperature during calibration,  $T_f = 40^\circ\text{C}$  is the film temperature, and  $T_a = 17.25^\circ\text{C}$  is the water temperature during data acquisition. The corrected voltage values were used to obtain the wall shear stress values using Eq.(4.8) with the calibration coefficients provided in Table 4.1.

#### 4.5.2 Comparison with numerical results

Numerical simulations were carried out using five different turbulence models, namely, Spalart-Allmaras,  $\kappa$ - $\epsilon$ ,  $\kappa$ - $\omega$ , Transition-SST, and RSM. These simulations were carried out for identical flow domain and boundary conditions in the experiments - see Figure 4.16. The domain is axially symmetric without variations in the azimuthal directions. Therefore, we used a two-dimensional axisymmetric model to reduce computational time. Assuming incompressible flow, we imposed a mass flow rate of  $\dot{m} = 0.046 \text{ kg/s}$  at the inlet, and exit pressure  $p = p_{\text{atm}}$  at the pad's outlet. Non-slip conditions were imposed on all solid walls.

Turbulence models implemented in commercial software require us to prescribe surface roughness level in solid walls. The choice of surface roughness level could be very relevant in fully rough flow, moderately important in transitionally rough flow, or completely unimportant in hydraulically smooth flow. The maximum wall shear stress measured in the current experiments was  $\tau_{w, \text{max}} =$

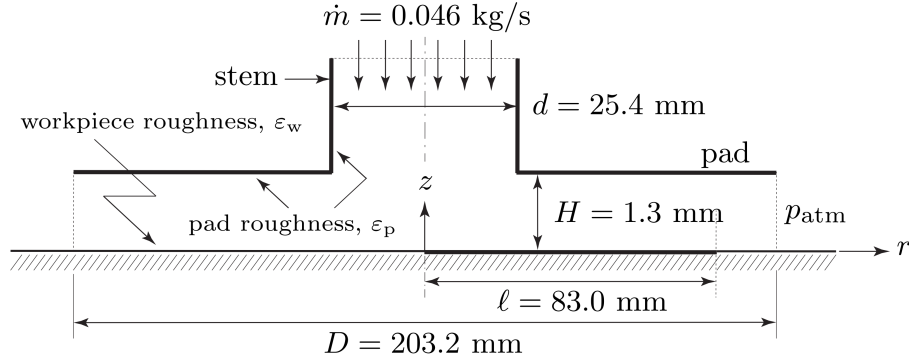


Figure 4.16 A schematic of the Bernoulli pad used in simulations.

10.19 Pa. Hence, the maximum friction velocity was  $u_{\tau_{\max}} \triangleq \sqrt{\tau_{w,\max}/\rho} = 0.1$  m/s. Given that the thickness of the laminar sublayer in a turbulent boundary layer is  $\delta_l^+ \triangleq \rho\delta_l u_\tau / \mu = 5$ , our flow would be hydraulically smooth if its surface roughness' representative height  $\varepsilon_w < \delta_l = \delta_l^+ \mu / (\rho u_\tau) = 49.5$   $\mu\text{m}$ . As mentioned before, the roughness level in polished aluminum goes typically up to  $Rz = 1.4$   $\mu\text{m}$ . Therefore, the flow through the pad's gap is hydraulically smooth. For the simulations, any choice of roughness height for which  $\varepsilon^+ < 5$  will have no roughness effects. With this in mind, the surface roughness of the pad and the workpiece were assumed to be  $\varepsilon_p = \varepsilon_w = 1$   $\mu\text{m}$  to ensure hydraulically smooth conditions as in the experiments.

In our experiments, the hot-film sensor voltage is obtained for the measurement region of length  $\ell = 83.0$  mm shown in Figure 4.16. A comparison of these voltages with the voltage values in Figure 4.7 indicate that the flow is laminar for  $r \in [0, 12] \cup [14, 83]$  and turbulent for  $r \in [12, 14]$ , where the units are in mm. The change from laminar to turbulent flow close to the neck of the pad is expected due to the constriction of the flow and the formation of a recirculation region due to flow separation upon change in the direction of flow from axial to radial around a sharp corner. To obtain the wall shear stress, we use the calibration coefficients in Table 4.1: the exponent and coefficient for laminar flow are used for  $r \in [0, 12] \cup [14, 83]$  and those for turbulent flow are used for  $r \in [12, 14]$ . The wall shear stress and radial distance are non-dimensionalized using the expressions in Anshul (Tomar et al. (2022)):

$$\bar{\tau}_w = \left( \frac{\pi \rho d^3}{4 \dot{m} \mu} \right) \tau_w, \quad \bar{r} = \left( \frac{2}{D} \right) r \quad (4.9)$$

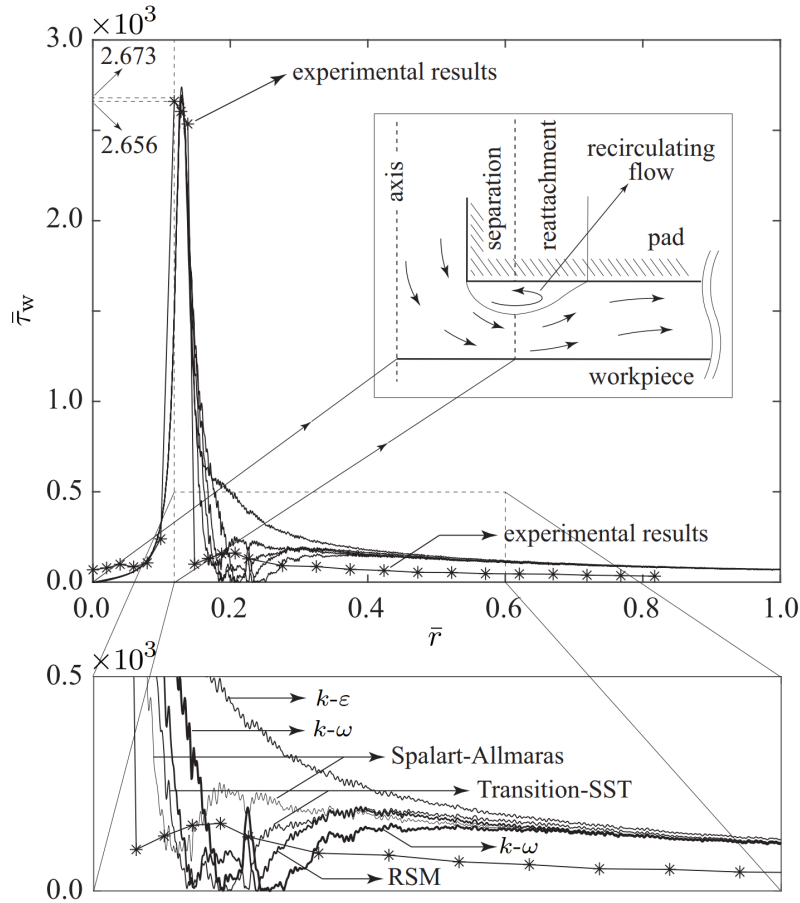


Figure 4.17 Variation of  $\bar{\tau}_w$  with  $\bar{r}$ : a comparison of simulation and experimental results. The experimental results, which were obtained at discrete values of  $\bar{r}$ , are shown using \* marks. The top figure shows the recirculation region and the flow around it Shi and Li (2016) - see figure inset. A magnified view of the dotted portion of the top figure is shown in the bottom figure for comparison of the five different turbulence models with experimental results.

The variation in the non-dimensional wall shear stress  $\bar{\tau}_w$  with non-dimensional radial distance  $\bar{r}$  is shown in Figure 4.17. No error bars are shown in these experimental results as the uncertainty associated with the measurements was found to be negligible (the extent of the error bars is less than the line thickness in the plot). For the purpose of model testing, the numerical simulation results from the five different turbulence models are also presented in Figure 4.17. All models coincide with each other for  $0 \leq \bar{r} \lesssim 0.14$  and  $0.5 \lesssim \bar{r} \leq 1.0$ , but differ significantly from each other in the reattachment region.

Overall, all models follow the qualitative behavior of the experimentally determined wall shear stress after the reattachment region. Nevertheless, all five turbulence models over-predict the wall

Table 4.2 Dimensionless maximum wall shear stress values obtained from experiment, numerical models, and power law Tomar et al. (2022)

Experiment	Spalart-Almaras	$\kappa\text{-}\varepsilon$	$\kappa\text{-}\omega$	Transition-SST	RSM	Power Law
2656.1	2673.1	2741.4	2692.5	2676.3	2696.9	2548.6

shear stress values in this region. This is consistent with the experimental results from Tomar et al. (2022). All numerical simulations predict both the magnitude and location of the maximum wall shear stress adequately, suggesting that all of them are able to capture the recirculation region reasonably well. The maximum non-dimensional wall shear stress  $\tau_{w,\max}$  for all cases, including a power law estimation from Tomar et al. (2022), is shown in Table 4.2. The simulation results and the power-law prediction exhibit good agreement with the experimental results.

The experimental measurements show a secondary peak in wall shear stress right after the sharp drop from the maximum wall shear stress. This secondary peak is followed by a gradual decay in wall shear stress. This gradual decay in wall shear stress is easily explained by the  $1/r$  proportional decay in radial velocity as the cross-sectional area of the pad gap increases with radius Guo et al. (2017). The secondary peak on the other hand is the result of reattachment phenomena. That is, the flow initially “squeezes” underneath the separation bubble forming a *vena contracta* and thinning the boundary layer. At the vena contracta, the flow is the fastest and the boundary layer is the thinnest, inducing the highest level of wall shear stress. The flow expands relatively rapidly toward the pad as it flows past the separation bubble. In this region, there is a localized change of direction as shown in the inset of Figure 4.17. Here, part of the linear momentum transfers from the radial direction to the wall-normal direction, with a resulting reduction in radial momentum. This results in the sharp drop of wall shear stress right after the vena contracta. But shortly after that, the momentum recovers its purely radial direction, and since the boundary layer is still very thin, the shear stress experiences a small boost. This is likely what causes the secondary peak in wall shear stress. Right after that, the boundary layer starts growing and the cross-section continues to grow with radius, causing the subsequent gradual reduction on wall shear stress.

Most of the models fail to capture the wall shear behavior in the reattachment region. The Spalart-Almaras model is the only scheme that exhibits the same qualitative behavior as the

experimentally measured wall shear stress, though the secondary peak is located slightly further downstream than that in experiments. This result suggests that, in this model, the simulated streamwise extent of the separation bubble downstream of the vena contracta is larger than that in experiments. That the Spalart-Almaras performs better than the other models in the reattachment region is likely because this model performs well in wall-bounded flows at moderate to low Reynolds numbers under adverse pressure gradients.

All five turbulence models slightly over-predict the wall shear stress values for large values of  $\bar{r}$ . This is consistent with the comparison between simulations and Particle Tracking Velocimetry measurements in Tomar et al. (2022). A better turbulence scheme, such as LES or DNS, may provide a better match for the entire domain of  $\bar{r}$ ; however, this will require significantly higher computational effort and lies in the scope of future research. The most important aspect of a Bernoulli pad for grooming applications is its maximum wall shear stress; the details of the reattachment region are of relatively low importance. Henceforth, the results shown in Figure 4.17 suggest that our numerical solvers are appropriate to capture the most relevant features of flow through a Bernoulli pad, with the Spalart-Almaras scheme exhibiting a slight advantage over the others. It is then adequate to use this numerical model to optimize Bernoulli pad designs for improving grooming efficacy in non-contact biofouling mitigation.

## **4.6 Conclusion**

The experimental work presented here uses a constant temperature anemometer with a hot-film sensor to quantify the wall shear stress generated by the action of Bernoulli pad over a proximally located workpiece. An experimental setup, consisting of a rectangular channel, is designed to calibrate the wall shear stress. The calibration of the sensor is carried out separately for laminar and turbulent regimes. These calibration relations are subsequently used to measure the wall shear stress generated by a Bernoulli pad. It should be mentioned that this experimental effort, which quantifies the wall shear stress generated by a Bernoulli pad with water as the working fluid, is the first of its kind.

Except for the reattachment region, numerical simulations exhibit good agreement with hot-

film wall shear measurements. The position of the maximum wall shear stress is found to be very close to the neck of the Bernoulli pad, right below the belly of recirculation region. The predicted position and magnitude of the maximum wall shear stress are very close to the measured values. All tested computational models match each other beyond the reattachment region and capture the general trend of the wall shear stress, albeit slightly overestimating its value. The Spalart-Almaras model reasonably captures the wall shear-stress behavior in the reattachment region, while the rest of the models fail to do so.

## CHAPTER 5

### SUMMARY AND FUTURE WORK

#### 5.1 Summary

Numerical simulations have been carried out to develop a better understanding of the flow physics of the Bernoulli gripper. The objective of the work is to employ the Bernoulli pad as a shear-based grooming tool. Computational Fluid Dynamics, CFD simulations are carried out for a range of parameters in the domain to achieve this. A power-law is obtained between the inlet fluid power and maximum wall shear stress obtained at the workpiece. The power-law collapses the data from all the parameter space on a single curve.

The data also indicate a power-law between the non-dimensional maximum shear stress and inlet Reynolds number as:  $\tau_{w,max}^* \propto Re_{in}^{n+1}$ . The value of  $n$  obtained from a direct fit into the CFD data is broadly consistent with the value of  $n$  found in the literature. Near the area where the maximum shear stress occurs, the velocity and gradient are highest, and this spot is closer to the jet exit  $d$  rather than the outer diameter  $D$  of the pad. According to the discussion, the power required to counteract wall shear across the entire pad seems directly related to its maximum value.

The direct relationship between the inlet fluid power and maximum wall shear stress motivated us to explore other ways of delivering the power to the system. For the first time in this work, the Bernoulli pad is provided with rotation to increase the wall shear stress and the normal force. The effect of rotation on the pad is first analyzed without inlet fluid power. The addition of inlet fluid power, along with the rotation, results in stable equilibrium configurations. It was noticed that there are two mass flow rate values for which the force generated on the workpiece is the same for a given equilibrium height. Therefore, two equilibrium configurations exist, which in this work has been referred to as bi-stiffness equilibria. The stiffness values at these equilibrium points are different; the stiffness is higher for the higher mass flow rates and vice versa.

The addition of rotation to the Bernoulli pad results in an increase in suction force. The work analysis was carried out, and it was found that for the same inlet fluid power, the increase in rotational speed from 0 rad/s to 60 rad/s results in a 14.93 % rise in the value of maximum wall

shear stress and a 13.85 % rise in the value of average wall shear stress. Similarly, for the same inlet fluid power, the normal force increases from 1.4037 N (repulsive and stable) to -6.6827 N (attractive and stable).

The numerical solver used in the present work is validated using the hot-film experiments. A setup is designed to calibrate the hot-film sensor with a Constant Temperature Anemometer, CTA. The calibration setup consists of a channel with flow conditioning parts installed at the inlet and outlet. Flow conditioning parts are used to make sure that the flow is fully developed in the channel. A fully developed flow in the channel ensures that a simplified analytical expression can be used to calibrate the hot-film sensor. The calibration curve obtained using the channel depicts three distinct regions: laminar, transition, and turbulent. Calibration coefficients are obtained for laminar and turbulent regions.

The calibrated sensor is used to obtain wall shear stress in a Bernoulli pad assembly on a shear stress station. The experimental setup, which consisted of a Bernoulli pad assembly and a shear stress station, was designed to ensure that the flow at the inlet of the stem had a low-turbulence intensity with a top-hat velocity profile. The wall shear stress obtained from the experiments is compared with the results obtained through CFD simulations for different turbulence models. The results from the experiments and numerical simulations show a very good match for the peak shear stress value. This suggests that all the numerical models are able to capture the recirculation region really well. It was also observed that most of the models are unable to capture the wall shear behavior in the reattachment region. Among all the turbulence models, the Spalart-Almaras model performs better than the other turbulence models.

## **5.2 Future Scope**

In this study, water was selected as the working fluid to simulate the flow field of the Bernoulli pad. This choice aligns with the intended application, which involves utilizing the Bernoulli pad to groom underwater surfaces without physical contact. By opting for water as the working fluid, the study aimed to replicate real-world conditions accurately. However, it's worth noting that the decision to use water as the working fluid introduces potential complexities, particularly regarding

cavitation effects. Cavitation occurs when local pressure drops below the vapor pressure, leading to the formation of vapor bubbles. These bubbles tend to form in regions where local velocity is high, precisely where the highest wall-shear stress is observed. If not avoided, cavitation can potentially harm the workpiece to be cleaned by resulting in erosion and pitting. The study did not explore cavitation effects, but it acknowledges the importance of addressing them in future research. Specifically, future work will focus on designing alternative flow geometries that can generate sufficiently high levels of shear stress to groom surfaces effectively while also avoiding cavitation. This aspect opens up avenues for further investigation and optimization of Bernoulli pad applications in underwater surface grooming.

In the present work, we have designed an experimental setup to measure the wall shear stress for a standard non-rotating Bernoulli pad and the numerical model is validated with five different turbulence models. In the future, an experimental setup needs to be designed to measure the wall shear stress for rotating Bernoulli pad. We expect this to be a challenging experiment as the gap between the rotating pad and the stationary workpiece is very small and a small misalignment could result in pad damaging against the workpiece. The CFD simulations in the present work for rotating pads are limited to a maximum rotational speed,  $\omega = 60$  rad/s. The value of rotational speed was chosen to avoid the convergence issues associated with the steep velocity and pressure gradients in the domain. However, we acknowledge that in future to fully maximize the benefits of the rotating pad, we need to simulate the rotating Bernoulli pad with higher rotational speeds.

## BIBLIOGRAPHY

ANSYS (2022). Ansys fluent: Theory guide 2022 R2 (Section 24.4.3.3. Coupled Algorithm).

Bellhouse, B. J. and Schultz, D. L. (1966). Determination of mean and dynamic skin friction, separation and transition in low-speed flow with a thin-film heated element. *Journal of Fluid Mechanics*, 24(2):379–400.

Brun, X. and Melkote, S. (2009). Analysis of stresses and breakage of crystalline silicon wafers during handling and transport. *Solar Energy Materials and Solar Cells*, 93:1238–1247.

Cameron Tropea, Alexander L. Yarin, J. F. F. (2007). *Springer Handbook of Experimental Fluid Mechanics*. Springer Berlin, Heidelberg.

D'Agostino, R. B. and Stephens, M. A. (1986). *Goodness-of-Fit Techniques*. Marcel Dekker, Inc., USA.

Dahlgren, J., Foy, L., Hunsucker, K., Gardner, H., Swain, G., Stafslie, S. J., Vanderwal, L., Bahr, J., and Webster, D. C. (2022). Grooming of fouling-release coatings to control marine fouling and determining how grooming affects the surface. *Biofouling*, 38(4):384–400.

Dantec Dynamics (2023). Flush-mounted hot-film probe.

Dini, G., Fantoni, G., and Failli, F. (2009). Grasping leather plies by bernoulli grippers. *CIRP Annals*, 58(1):21–24.

Donnelly, B., Sammut, K., and Tang, Y. (2022). Materials selection for antifouling systems in marine structures. *Molecules*, 27(11):3408.

Erturk, S. and Erzincanli, F. (2020). Design and development of a non-contact robotic gripper for tissue manipulation in minimally invasive surgery. *Acta bio-medica : Atenei Parmensis*, 91:e2020071.

Fantoni, G., Santochi, M., Dini, G., Tracht, K., Scholz-Reiter, B., Fleischer, J., Kristoffer Lien, T., Seliger, G., Reinhart, G., Franke, J., Nørgaard Hansen, H., and Verl, A. (2014). Grasping devices and methods in automated production processes. *CIRP Annals*, 63(2):679–701.

Fernholz, H. H., Janke, G., Schober, M., Wagner, P. M., and Warnack, D. (1996). New developments and applications of skin-friction measuring techniques. *Measurement Science and Technology*, 7(10):1396.

Frey, H. (U.S. Patent 5967578, 1999). Tool for the contact-free support of plate-like substrates.

Gibson, L., Galloway, L., Kim, S. i., and Spence, S. (2017). Assessment of turbulence model predictions for a centrifugal compressor simulation. *Journal of the Global Power and Propulsion*

- Society*, 1:142–156.
- Guo, J., Shan, H., Xie, Z., Li, C., Xu, H., and Zhang, J. (2017). Exact solution to Navier-Stokes equation for developed radial flow between parallel disks. *Journal of Engineering Mechanics*, 143(6).
- Houghtalen, R. J., Akan, A. O., and Hwang, N. H. (1996). *Fundamentals of hydraulic engineering systems*. Prentice Hall.
- Hu, P., Xie, Q., Ma, C., and Zhang, G. (2020). Silicone-based fouling-release coatings for marine antifouling. *Langmuir*, 36(9):2170–2183.
- Hussain, A. K. M. F. and Ramjee, V. (1976). Effects of the Axisymmetric Contraction Shape on Incompressible Turbulent Flow. *Journal of Fluids Engineering*, 98(1):58–68.
- Islam, S. M., Khan, M. T., and Ahmed, Z. U. (2020). Effect of design parameters on flow characteristics of an aerodynamic swirl nozzle. *Progress in Computational Fluid Dynamics, an International Journal*, 20(5):249–262.
- Jawarneh, A. M. and Vatistas, G. H. (2006). Reynolds Stress Model in the Prediction of Confined Turbulent Swirling Flows. *Journal of Fluids Engineering*, 128(6):1377–1382.
- Jiang, F., Lee, G.-B., Tai, Y.-C., and Ho, C.-M. (2000). A flexible micromachine-based shear-stress sensor array and its application to separation-point detection. *Sensors and Actuators A: Physical*, 79(3):194–203.
- Kamensky, K., Hellum, A., and Mukherjee, R. (2019). Power scaling of radial outflow: Bernoulli pads in equilibrium. *ASME Journal of Fluids Engineering*, 141.
- Kamensky, K., Hellum, A., Mukherjee, R., Naik, A., and Moisaner, P. (2020). Underwater shear-based grooming of marine biofouling using a non-contact bernoulli pad device. *Biofouling*, 36:951–964.
- Kamensky, K. M. (2020). *A new paradigm for generating surface-normal forces for hull-cleaning robots*. PhD dissertation, Department of Mechanical Engineering, Michigan State University.
- King, L. V. (1914). Xii. on the convection of heat from small cylinders in a stream of fluid: Determination of the convection constants of small platinum wires with applications to hot-wire anemometry. *Philosophical transactions of the royal society of London. series A, containing papers of a mathematical or physical character*, 214(509-522):373–432.
- Li, X. and Kagawa, T. (2014). Theoretical and experimental study of factors affecting the suction force of a bernoulli gripper. *Journal of Engineering Mechanics*, 140:04014066.
- Logue, J. (U.S. Patent No. 3523706, 1970). Apparatus for supporting articles without structural

contact and for positioning the supported articles.

- McIlwraith, L. and Christie, A. (U.S. Patent No. 6601888, 2003). Contactless handling of objects.
- Menesses, M., Belden, J., Dickenson, N., and Bird, J. (2017). Measuring a critical stress for continuous prevention of marine biofouling accumulation with aeration. *Biofouling*, 33(9):703–711.
- Misimi, E., oye, E., Lillienkiold, A., Mathiassen, J., Berg, O. A., Gjerstad, T. B., Buljo, J., and Skotheim, O. (2016). GRIBBOT – Robotic 3D vision-guided harvesting of chicken fillets. *Computers and Electronics in Agriculture*, 121:84–100.
- Nakabayashi, K., Ichikawa, T., and Morinishi, Y. (2002). Size of annular separation bubble around the inlet corner and viscous flow structure between two parallel disks. *Experiments in Fluids*, 32(4):425–433.
- Neto, J. L. V., Martins, A. L., Neto, A. S., Ataíde, C. H., and Barrozo, M. A. S. (2011). CFD applied to turbulent flows in concentric and eccentric annuli with inner shaft rotation. *The Canadian Journal of Chemical Engineering*, 89(4):636–646.
- Nikuradse, J. (1950). Laws of flow in rough pipes, ational advisory commission for aeronautics (naca) technical memorandum 1292, (english translation of "stromungsgesetze in rauhen rohren." vdi-forschungsheft 361, 1933.
- Oliveira, D. R. and Granhag, L. (2020). Ship hull in-water cleaning and its effects on fouling-control coatings. *Biofouling*, 36(3):332–350.
- Olsson, R. G. and Williams, E. C. (U.S. Patent No. 3,438,668, 1969). Contactless lifter.
- Owen, F. K. (1970). Transition experiments on a flat plate at subsonic and supersonic speeds.
- Paivanas, J. A. and Hassan, J. K. (1981). Attraction force characteristics engendered by bounded, radially diverging air flow. *IBM Journal of Research and Development*, 25(3):176–186.
- Phares, D. J., Smedley, G. T., and Flagan, R. C. (2000). The wall shear stress produced by the normal impingement of a jet on a flat surface. *Journal of Fluid Mechanics*, 418(1):351–375.
- S, S., Nair, C. K., and Shetty, J. (2011). Effect of Different Polishing Agents on Surface Finish and Hardness of Denture Base Acrylic Resins: A Comparative Study. *International Journal of Prosthodontics and Restorative Dentistry*, 1(1):7–11.
- Sheplak, M., Cattafesta, L., Nishida, T., and Mcginley, C. (2006). Mems shear stress sensors: Promise and progress. *IUTAM Symposium on Flow Control and MEMS*, pages 67–76.
- Shi, K. and Li, X. (2016). Optimization of outer diameter of Bernoulli gripper. *Experimental*

- Thermal and Fluid Science*, 77:284–294.
- Song, C. and Cui, W. (2020). Review of underwater ship hull cleaning technologies. *Journal of marine science and application*, 19(3):415–429.
- Stähli, A. (2013). The technique of lapping. *Pieterlen/Biel*.
- Stephens, M. A. (1974). EDF statistics for goodness of fit and some comparisons. *Journal of the American Statistical Association*, 69(347):730–737.
- Sun, B., Wang, P., Luo, J., Deng, J., Guo, S., and Ma, B. (2018). A flexible hot-film sensor array for underwater shear stress and transition measurement. *Sensors*, 18(10).
- THORLABS (2023). Lts300: 300 mm linear translation stage with integrated controller, stepper motor.
- Tomar, A. S., Kamensky, K. M., Mejia-Alvarez, R., Hellum, A. M., and Mukherjee, R. (2022). A scaling relationship between power and shear for Bernoulli pads at equilibrium. *Flow*, 2:E29.
- Tribou, M. and Swain, G. (2010). The use of proactive in-water grooming to improve the performance of ship hull antifouling coatings. *Biofouling*, 26(1):47–56.
- Trickey, J. S., Cárdenas-Hinojosa, G., Rojas-Bracho, L., Schorr, G. S., Rone, B. K., Hidalgo-Pla, E., Rice, A., and Baumann-Pickering, S. (2022). Ultrasonic antifouling devices negatively impact Cuvier’s beaked whales near Guadalupe island, México. *Communications Biology*, 5(1):1005.
- VALIDYNE Engineering (2022). Dp15 variable reluctance pressure sensor capable of range changes.
- Wagner, M., Chen, X., Nayerloo, M., Wang, W., and Chase, J. G. (2008). A novel wall climbing robot based on bernoulli effect. In *IEEE/ASME International Conference on Mechatronic and Embedded Systems and Applications*, pages 210–215.
- Wark, C. E. and Foss, J. F. (1984). Forces caused by the radial out-flow between parallel disks. *Journal of Fluids Engineering-transactions of The Asme*, 106:292–297.
- White, F. (1974). *Viscous fluid flow*. NY: McGraw-Hill, New York.
- Winter, K. G. (1979). An outline of the techniques available for the measurement of skin friction in turbulent boundary layers. *Progress in Aerospace Sciences*, 18:1–57.
- Yeginbayeva, I. and Atlar, M. (2018). An experimental investigation into the surface and hydrodynamic characteristics of marine coatings with mimicked hull roughness ranges. *Biofouling*, 34(9):1001–1019.

## APPENDIX

For this analysis, we will assume a system of cylindrical coordinates,  $(r, \theta, z)$ , with the  $z$ -axis coinciding with the stem axis as shown in Figure 1.2, and the  $r - \theta$  plane coinciding with the impingement wall. Further, we will assume that the origin of this coordinate system coincides with the origin of a reference coordinate system,  $(R, \Theta, Z)$ , whose  $Z$ -axis is aligned with and is positive in the opposite direction of gravity. For simplicity, and without loss of generality, the system  $(r, \theta, z)$  is rotated with respect to the system  $(R, \Theta, Z)$  around the reference axis  $(\Theta = 0, Z = 0)$  by an angle  $\alpha$  with respect to the  $Z$ -axis. Finally, the reference axis  $(\theta = 0, z = 0)$  makes an angle  $\phi$  with the reference axis  $(\Theta = 0, Z = 0)$ .

In general, for any angle  $\alpha$  between the  $z$ - and  $Z$ -axes, the gravitational field in the  $(r, \theta, z)$  coordinate system is given by:

$$\mathbf{g} = -g \sin \alpha \sin(\theta + \phi) \hat{\mathbf{r}} - g \sin \alpha \cos(\theta + \phi) \hat{\boldsymbol{\theta}} - g \cos \alpha \hat{\mathbf{z}} \quad (\text{A.1})$$

Note that in our simulations  $\alpha = \pi/2$  and  $\phi = -\pi/2$ . Hence, the gravitational field in the  $(r, \theta, z)$  system is:

$$\mathbf{g} = g \cos \theta \hat{\mathbf{r}} - g \sin \theta \hat{\boldsymbol{\theta}} + 0 \hat{\mathbf{z}} \quad (\text{A.2})$$

All the analysis will be carried out based on the more general form shown in equation (A.1), and then the result will be simplified for the specific case shown in equation (A.2).

### Specific Considerations

Under this condition, the outside hydrostatic pressure would change azimuthally at the pad's discharge due to changes in water depth as  $\theta$  changes. This boundary condition would likely induce a non-zero azimuthal change in the radial velocity component and possibly a non-zero azimuthal velocity component. Nevertheless, our domain of interest is a disk sector defined by  $-4^\circ \leq \theta \leq 4^\circ$ , for which the changes in depth are very small, making the azimuthal changes in pressure and velocity (and hence the azimuthal component of velocity) negligible. In this region, the radial component of velocity dominates.

The flow needs to transition from purely axial to radial near the connection between the inlet pipe and the pad. Near this region, the flow between the pad and wall still has an axial component, but as the flow progresses through the gap, the velocity field gradually becomes purely radial:  $\mathbf{u}(r, z) = u_r(r, z)\hat{\mathbf{r}} + 0\hat{\boldsymbol{\theta}} + 0\hat{\mathbf{z}}$ . Here, we emphasize that the velocity field will asymptotically become axisymmetric and a function of only the radial and axial coordinates. This is due to the fact that the circumferential cross-section increases radially and that the two parallel plates impose non-slip boundary conditions. This is the flow condition that we will use for our analysis.

### Scaling

The following are appropriate dimensionless versions of each physical quantity:

$$r^* = \frac{r}{d}$$

$$\frac{\partial r^*}{\partial r} = \frac{1}{d}$$

$$z^* = \frac{z}{h_{\text{eq}}}$$

$$\frac{\partial z^*}{\partial z} = \frac{1}{h_{\text{eq}}}$$

$$u^* = \frac{u_r}{u_{\text{in}}}$$

$$p^* = \frac{p}{\rho u_{\text{in}}^2}$$

### Conservation Equations

#### Continuity

The general form of the continuity equation in cylindrical coordinates is:

$$\frac{1}{r} \frac{\partial(ru_r)}{\partial r} + \frac{1}{r} \frac{\partial u_\theta}{\partial \theta} + \frac{\partial u_z}{\partial z} = 0$$

For purely radial axisymmetric flow, we assume the conditions  $u_\theta = u_z = 0$ . The continuity equation in cylindrical coordinates for incompressible-steady flow can then be simplified and expanded as follows:

$$r \frac{\partial u_r}{\partial r} + u_r = 0$$

In dimensionless form:

$$r^* u_{in} d \frac{\partial u^*}{\partial r^*} \cdot \frac{\partial r^*}{\partial r} + u_{in} u^* = 0$$

$$r^* u_{in} d \frac{\partial u^*}{\partial r^*} \cdot \frac{1}{d} + u_{in} u^* = 0$$

$$r^* \frac{\partial u^*}{\partial r^*} + u^* = 0 \tag{A.3}$$

Then, partially integrating equation (A.3) gives the following result for the velocity field:

$$\int_{u_o^*(\theta, z^*)}^{u^*} \frac{\partial u^*}{u^*} = - \int_{r_o^*}^{r^*} \frac{\partial r^*}{r^*}$$

$$\ln \left( \frac{u^*}{u_o^*(\theta, z^*)} \right) = - \ln \left( \frac{r^*}{r_o^*} \right)$$

$$u^*(r^*, \theta, z^*) = \frac{r_o^*}{r^*} u_o^*(\theta, z^*) \tag{A.4}$$

Which shows the variation of velocity non-dimensionally.

Dropping the dependence on  $\theta$  and writing the result in vector form, we obtain:

$$\mathbf{u}^*(r^*, z^*) = \frac{r_o^*}{r^*} u_o^*(z^*) \hat{\mathbf{r}}$$

Where  $u_o^*(z^*)$  is the radial component of velocity at the reference radius,  $r_o^*$ . The velocity field  $u_o^*(z^*)$  is a function of  $z^*$  resulting from the non-slip boundary conditions and viscous effects.

### Momentum Equations

The next step in determining the asymptotic behavior for the pressure field is to use Navier-Stokes equations for incompressible-steady flow considering the same simplifications imposed on the continuity equation ( $u_\theta = u_z = 0$ ), plus one simplification related to the azimuthal derivative:  $\partial u_r / \partial \theta = 0$ . This last simplification is imposed due to the narrow range of  $\theta$  used in our simulations.

#### ***r*-momentum equation:**

After simplifications, the *r*-momentum equation becomes:

$$u_r \frac{\partial u_r}{\partial r} = -\frac{1}{\rho} \frac{\partial p}{\partial r} + g_r + \nu \left[ -\frac{1}{r^2} \left( r \frac{\partial u_r}{\partial r} + u_r \right) + \frac{\partial^2 u_r}{\partial z^2} \right] \quad (\text{A.5})$$

Here,  $g_r$  is the component of gravity in the radial direction as defined in equation (A.1). Applying the continuity equation (A.3) in (A.5):

$$-\frac{u_r^2}{r} = -\frac{1}{\rho} \frac{\partial p}{\partial r} + g_r + \nu \frac{\partial^2 u_r}{\partial z^2}$$

In dimensionless form:

$$-\frac{(u^* u_{\text{in}})^2}{r^* d} = -\frac{1}{\rho} \frac{\partial (p^* \rho u_{\text{in}}^2)}{\partial r^*} \cdot \frac{\partial r^*}{\partial r} + g_r + \nu \frac{\partial^2 (u^* u_{\text{in}})}{\partial z^* \partial z^*} \cdot \frac{\partial z^*}{\partial z} \cdot \frac{\partial z^*}{\partial z}$$

$$-\frac{u_{\text{in}}^2}{d} \cdot \frac{u^*}{r^*} = -\frac{u_{\text{in}}^2}{d} \cdot \frac{\partial p^*}{\partial r^*} + g_r + \frac{\nu u_{\text{in}}}{h_{\text{eq}}^2} \cdot \frac{\partial^2 u^*}{\partial z^{*2}}$$

$$\begin{aligned}\frac{\partial p^*}{\partial r^*} &= \frac{g_r d}{u_{\text{in}}^2} + \frac{u^{*2}}{r^*} + \frac{\nu u_{\text{in}}}{h_{\text{eq}}^2} \cdot \frac{d}{u_{\text{in}}^2} \cdot \frac{d}{d} \cdot \frac{\partial^2 u^*}{\partial z^{*2}} \\ \frac{\partial p^*}{\partial r^*} &= - [\sin \alpha \sin(\theta + \phi)] \frac{g d}{u_{\text{in}}^2} + \frac{u^{*2}}{r^*} + \frac{\nu u_{\text{in}}}{h_{\text{eq}}^2} \cdot \frac{d}{u_{\text{in}}^2} \cdot \frac{d}{d} \cdot \frac{\partial^2 u^*}{\partial z^{*2}} \\ \frac{\partial p^*}{\partial r^*} &= - [\sin \alpha \sin(\theta + \phi)] \text{Ri}_{\text{in}} + \frac{u^{*2}}{r^*} + \frac{1}{h^{*2} \text{Re}_{\text{in}}} \cdot \frac{\partial^2 u^*}{\partial z^{*2}}\end{aligned}\quad (\text{A.6})$$

Here,  $\text{Ri}_{\text{in}} = g d / u_{\text{in}}^2$  is the Richardson number based on inlet conditions,  $\text{Re}_{\text{in}} = u_{\text{in}} d / \nu$  is the Reynolds number based on inlet conditions, and  $h^* = h_{\text{eq}} / d$  is the dimensionless equilibrium gap.

**Equation (A.6) suggests that viscous shear is scaled by the product  $h^{*2} \text{Re}_{\text{in}}$ .**

We can now substitute  $u^*$  from equation (A.4) into equation (A.6) (dropping  $\theta$  dependence from  $u^*$  to conform to our experimental conditions):

$$\frac{\partial p^*}{\partial r^*} = - [\sin \alpha \sin(\theta + \phi)] \text{Ri}_{\text{in}} + \frac{r_o^{*2}}{r^{*3}} [u_o^*(z^*)]^2 + \frac{1}{h^{*2} \text{Re}_{\text{in}}} \cdot \frac{r_o^*}{r^*} \cdot \frac{\partial^2 u_o^*(z^*)}{\partial z^{*2}}$$

This equation can be integrated partially:

$$\begin{aligned}\int_{p_o^*(\theta, z^*)}^{p^*} \partial p^* &= - [\sin \alpha \sin(\theta + \phi)] \text{Ri}_{\text{in}} \int_{r_o^*}^{r^*} \partial r^* + r_o^{*2} [u_o^*(z^*)]^2 \int_{r_o^*}^{r^*} \frac{\partial r^*}{r^{*3}} + \frac{r_o^*}{h^{*2} \text{Re}_{\text{in}}} \cdot \frac{\partial^2 u_o^*(z^*)}{\partial z^{*2}} \int_{r_o^*}^{r^*} \frac{\partial r^*}{r^*} \\ p^*(r^*, \theta, z^*) &= - [\sin \alpha \sin(\theta + \phi)] \text{Ri}_{\text{in}} (r^* - r_o^*) + \frac{1}{2} [u_o^*(z^*)]^2 \left(1 - \frac{r_o^{*2}}{r^{*2}}\right) \\ &\quad + \frac{r_o^*}{h^{*2} \text{Re}_{\text{in}}} \cdot \frac{\partial^2 u_o^*(z^*)}{\partial z^{*2}} \ln \left(\frac{r^*}{r_o^*}\right) + p_o^*(\theta, z^*)\end{aligned}\quad (\text{A.7})$$

We consider the case  $\alpha = \pi/2$ . Hence, equation (A.7) can be re-written as:

$$\begin{aligned}p^*(r^*, \theta, z^*) &= - \sin(\theta + \phi) \text{Ri}_{\text{in}} (r^* - r_o^*) + \frac{1}{2} [u_o^*(z^*)]^2 \left(1 - \frac{r_o^{*2}}{r^{*2}}\right) \\ &\quad + \frac{r_o^*}{h^{*2} \text{Re}_{\text{in}}} \cdot \frac{\partial^2 u_o^*(z^*)}{\partial z^{*2}} \ln \left(\frac{r^*}{r_o^*}\right) + p_o^*(\theta, z^*)\end{aligned}\quad (\text{A.8})$$

**$\theta$ -momentum equation:**

After simplifications, the  $\theta$ -momentum equation becomes:

$$-\frac{1}{\rho r} \frac{\partial p}{\partial \theta} + g_\theta = 0 \quad (\text{A.9})$$

In dimensionless form:

$$\frac{\rho u_{\text{in}}^2}{\rho r^* d} \frac{\partial p^*}{\partial \theta} = g_\theta$$

$$\frac{\partial p^*}{\partial \theta} = \frac{g_\theta d}{u_{\text{in}}^2} r^*$$

$$\frac{\partial p^*}{\partial \theta} = - [\sin \alpha \cos(\theta + \phi)] \frac{g d}{\rho u_{\text{in}}^2} r^*$$

$$\frac{\partial p^*}{\partial \theta} = - [\sin \alpha \cos(\theta + \phi)] \text{Ri}_{\text{in}} r^* \quad (\text{A.10})$$

Equation (A.10) can now be integrated partially:

$$\int_{p_o^*(r^*, z^*)}^{p^*} \partial p^* = -\text{Ri}_{\text{in}} r^* \sin \alpha \int_{\theta_o}^{\theta} \cos(\theta + \phi) \partial \theta$$

$$p^*(r^*, \theta, z^*) = -\text{Ri}_{\text{in}} r^* \sin \alpha [\sin(\theta + \phi) - \sin(\theta_o + \phi)] + p_o^*(r^*, z^*) \quad (\text{A.11})$$

We consider the case for  $\alpha = \pi/2$ . Equation (A.11) can then be rewritten as:

$$p^*(r^*, \theta, z^*) = -\text{Ri}_{\text{in}} r^* [\sin(\theta + \phi) - \sin(\theta_o + \phi)] + p_o^*(r^*, z^*) \quad (\text{A.12})$$

In similar way we can obtain a relation with  $z$ -momentum equation. This will help in realizing the flow field in all the three coordinates.

**z-momentum equation:**

After simplifications, the z-momentum equation becomes:

$$\frac{\partial p}{\partial z} = \rho g_z$$

In dimensionless form:

$$\rho u_{\text{in}}^2 \frac{\partial p^*}{\partial z^*} \cdot \frac{\partial z^*}{\partial z} = \rho g_z$$

$$\rho u_{\text{in}}^2 \frac{\partial p^*}{\partial z^*} \cdot \frac{1}{h_{\text{eq}}} = \rho g_z$$

$$\frac{\partial p^*}{\partial z^*} = \frac{\rho (-g \cos \alpha)}{\rho u_{\text{in}}^2} \cdot h_{\text{eq}} \cdot \frac{d}{d}$$

$$\frac{\partial p^*}{\partial z^*} = -(\cos \alpha) \text{Ri}_{\text{in}} h^* \tag{A.13}$$

Equation (A.13) can now be integrated partially:

$$\int_{p_o^*(r^*, \theta)}^{p^*} \partial p^* = -(\cos \alpha) \text{Ri}_{\text{in}} h^* \int_{z_o^*}^{z^*} \partial z^*$$

$$p^*(r^*, \theta, z^*) = -(\cos \alpha) \text{Ri}_{\text{in}} h^* (z^* - z_o^*) + p_o^*(r^*, \theta) \tag{A.14}$$

Considering the case  $\alpha = \pi/2$ , we obtain:

$$p^*(r^*, \theta, z^*) = p_o^*(r^*, \theta) \tag{A.15}$$

Equation (A.15) imposes the condition that  $p^*$  must be independent of  $z^*$  when  $\alpha = \pi/2$ . With this in mind, equations (A.8), (A.12), and (A.15), can be re-written.

The equation obtained will remove the  $z$  coordinate dependency.

$$p^*(r^*, \theta) = -\sin(\theta + \phi) \text{Ri}_{\text{in}} (r^* - r_o^*) + \frac{1}{2} [u_o^*(z^*)]^2 \left(1 - \frac{r_o^{*2}}{r^{*2}}\right) + \frac{r_o^*}{h^{*2} \text{Re}_{\text{in}}} \cdot \frac{\partial^2 u_o^*(z^*)}{\partial z^{*2}} \ln\left(\frac{r^*}{r_o^*}\right) + p_o^*(\theta) \quad (\text{A.16})$$

$$p^*(r^*, \theta) = -\text{Ri}_{\text{in}} r^* [\sin(\theta + \phi) - \sin(\theta_o + \phi)] + p_o^*(r^*) \quad (\text{A.17})$$

$$p^*(r^*, \theta) = p_o^*(r^*, \theta) \quad (\text{A.18})$$

Since all these equations must in principle describe the same pressure field, the results must be compatible and satisfy all the differential equations for conservation of linear momentum. To find the final form of the pressure field, let's first subtract equation (A.17) from (A.16):

$$0 = -\sin(\theta + \phi) \text{Ri}_{\text{in}} (r^* - r_o^*) + \frac{1}{2} [u_o^*(z^*)]^2 \left(1 - \frac{r_o^{*2}}{r^{*2}}\right) + \frac{r_o^*}{h^{*2} \text{Re}_{\text{in}}} \cdot \frac{\partial^2 u_o^*(z^*)}{\partial z^{*2}} \ln\left(\frac{r^*}{r_o^*}\right) + p_o^*(\theta) + \text{Ri}_{\text{in}} r^* [\sin(\theta + \phi) - \sin(\theta_o + \phi)] - p_o^*(r^*)$$

$$0 = \text{Ri}_{\text{in}} r_o^* \sin(\theta + \phi) - \text{Ri}_{\text{in}} r^* \sin(\theta_o + \phi) + \frac{1}{2} [u_o^*(z^*)]^2 \left(1 - \frac{r_o^{*2}}{r^{*2}}\right) + \frac{r_o^*}{h^{*2} \text{Re}_{\text{in}}} \cdot \frac{\partial^2 u_o^*(z^*)}{\partial z^{*2}} \ln\left(\frac{r^*}{r_o^*}\right) + p_o^*(\theta) - p_o^*(r^*) \quad (\text{A.19})$$

For equation (A.19) to be satisfied, all the terms that are functions of  $\theta$  must cancel each other, and all the terms that are functions of  $r^*$  must cancel each other as well:

$$0 = \text{Ri}_{\text{in}} r_o^* \sin(\theta + \phi) + p_o^*(\theta)$$

$$\Rightarrow p_o^*(\theta) = -\text{Ri}_{\text{in}} r_o^* \sin(\theta + \phi) \quad (\text{A.20})$$

$$0 = -\text{Ri}_{\text{in}} r^* \sin(\theta_o + \phi) + \frac{1}{2} [u_o^*(z^*)]^2 \left(1 - \frac{r_o^{*2}}{r^{*2}}\right) + \frac{r_o^*}{h^{*2} \text{Re}_{\text{in}}} \cdot \frac{\partial^2 u_o^*(z^*)}{\partial z^{*2}} \ln\left(\frac{r^*}{r_o^*}\right) - p_o^*(r^*)$$

Further simplifying the above equation we will get,

$$\Rightarrow p_o^*(r^*) = -\text{Ri}_{\text{in}} r^* \sin(\theta_o + \phi) + \frac{1}{2} [u_o^*(z^*)]^2 \left(1 - \frac{r_o^{*2}}{r^{*2}}\right) + \frac{r_o^*}{h^{*2} \text{Re}_{\text{in}}} \cdot \frac{\partial^2 u_o^*(z^*)}{\partial z^{*2}} \ln\left(\frac{r^*}{r_o^*}\right) \quad (\text{A.21})$$

We now add equations (A.16) and (A.17):

$$2p^*(r^*, \theta) = -\sin(\theta + \phi) \text{Ri}_{\text{in}} (r^* - r_o^*) + \frac{1}{2} [u_o^*(z^*)]^2 \left(1 - \frac{r_o^{*2}}{r^{*2}}\right) + \frac{r_o^*}{h^{*2} \text{Re}_{\text{in}}} \cdot \frac{\partial^2 u_o^*(z^*)}{\partial z^{*2}} \ln\left(\frac{r^*}{r_o^*}\right) - \text{Ri}_{\text{in}} r^* [\sin(\theta + \phi) - \sin(\theta_o + \phi)] + p_o^*(\theta) + p_o^*(r^*)$$

Substitute  $p_o^*(\theta)$  and  $p_o^*(r^*)$  from the results (A.20) and (A.21) respectively:

$$2p^*(r^*, \theta) = -\sin(\theta + \phi) \text{Ri}_{\text{in}} (r^* - r_o^*) + \frac{1}{2} [u_o^*(z^*)]^2 \left(1 - \frac{r_o^{*2}}{r^{*2}}\right) + \frac{r_o^*}{h^{*2} \text{Re}_{\text{in}}} \cdot \frac{\partial^2 u_o^*(z^*)}{\partial z^{*2}} \ln\left(\frac{r^*}{r_o^*}\right) - \text{Ri}_{\text{in}} r^* [\sin(\theta + \phi) - \sin(\theta_o + \phi)] - \text{Ri}_{\text{in}} r_o^* \sin(\theta + \phi) - \text{Ri}_{\text{in}} r^* \sin(\theta_o + \phi) + \frac{1}{2} [u_o^*(z^*)]^2 \left(1 - \frac{r_o^{*2}}{r^{*2}}\right) + \frac{r_o^*}{h^{*2} \text{Re}_{\text{in}}} \cdot \frac{\partial^2 u_o^*(z^*)}{\partial z^{*2}} \ln\left(\frac{r^*}{r_o^*}\right) \Rightarrow p^*(r^*, \theta) = -\text{Ri}_{\text{in}} r^* \sin(\theta + \phi) + \frac{1}{2} [u_o^*(z^*)]^2 \left(1 - \frac{r_o^{*2}}{r^{*2}}\right) + \frac{r_o^*}{h^{*2} \text{Re}_{\text{in}}} \cdot \frac{\partial^2 u_o^*(z^*)}{\partial z^{*2}} \ln\left(\frac{r^*}{r_o^*}\right) \quad (\text{A.22})$$

Finally, for condition (A.15) to be satisfied, equation (A.22) must not be a function of  $z^*$ . Which implies:

$$\frac{\partial p^*(r^*, \theta)}{\partial z^*} = 0 \quad (\text{A.23})$$

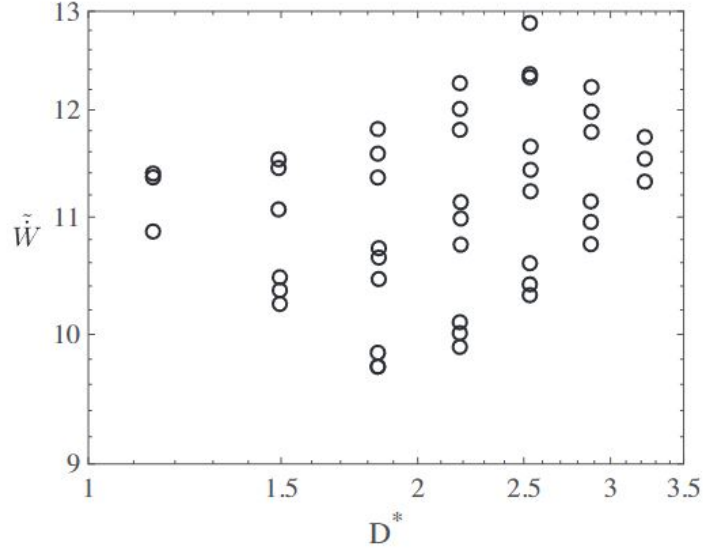


Figure A.1 Scatter plot of  $\tilde{W}$  vs  $D^*$  exhibiting no correlation.

Taking the partial derivative of equation (A.22) and making it equal to zero:

$$0 = \left(1 - \frac{r_o^{*2}}{r^{*2}}\right) u_o^*(z^*) \frac{\partial u_o^*(z^*)}{\partial z^*} + \frac{r_o^*}{h^{*2} \text{Re}_{\text{in}}} \cdot \ln\left(\frac{r^*}{r_o^*}\right) \frac{\partial^3 u_o^*(z^*)}{\partial z^{*3}} \quad (\text{A.24})$$

The solution to equation (A.24) guarantees that condition (A.8) is met, and gives the reference velocity profile inside the Bernoulli pad's gap.

### Observations Related to Scaling Analysis

The dimensional analysis suggests a function of the form:

$$\tilde{W} = \Phi(D^*, h^*, \tilde{\tau}, \text{Re}_{\text{in}}) \quad (\text{A.25})$$

However, as shown in Figure A.1, there is no correlation between  $\tilde{W}$  and  $D^*$ , simplifying the dimensionless function to:

$$\tilde{W} = \Phi(h^*, \tilde{\tau}, \text{Re}_{\text{in}}) \quad (\text{A.26})$$

On the other hand, the third term on the right-hand-side of equation (A.22) represents the effect of viscous resistance on the pressure field. This term can be used to get an insight on how the parameters from equation (A.26) relate to each other.

The equation now becomes:

$$p^*(\theta, z^*) = \dots + \dots + \frac{r_o^*}{h^* \text{Re}_{\text{in}}} \cdot \frac{\partial^2 u_o^*(z^*)}{\partial z^{*2}} \ln \left( \frac{r^*}{r_o^*} \right)$$

$$p^*(\theta, z^*) = \dots + \dots + r_o^* \ln \left( \frac{r^*}{r_o^*} \right) \frac{\partial}{\partial z^*} \left[ \frac{1}{h^* \text{Re}_{\text{in}}} \cdot \frac{\mu}{\mu} \cdot \frac{h_{\text{eq}}}{u_{\text{in}}} \cdot \frac{\partial u_o(z)}{\partial z} \right]$$

$$p^*(\theta, z^*) = \dots + \dots + r_o^* \ln \left( \frac{r^*}{r_o^*} \right) \frac{\partial}{\partial z^*} \left[ \frac{1}{h^* \text{Re}_{\text{in}}} \cdot \frac{1}{\mu} \cdot \frac{h_{\text{eq}}}{u_{\text{in}}} \cdot \frac{d}{d} \cdot \tau_o(z) \right]$$

$$p^*(\theta, z^*) = \dots + \dots + r_o^* \ln \left( \frac{r^*}{r_o^*} \right) \frac{\partial}{\partial z^*} \left[ \frac{1}{h^* \text{Re}_{\text{in}}} \cdot \frac{h_{\text{eq}}}{d} \cdot \frac{\tau_o(z) d}{\mu u_{\text{in}}} \right]$$

$$p^*(\theta, z^*) = \dots + \dots + r_o^* \ln \left( \frac{r^*}{r_o^*} \right) \frac{\partial}{\partial z^*} \left[ \frac{\tau_o^*(z^*)}{h^* \text{Re}_{\text{in}}} \right] \quad (\text{A.27})$$

Equation (A.27) suggests that the local viscous shear,  $\tau_o^*(z^*)$ , scales with  $h^* \text{Re}_{\text{in}}$ . This relation suggest that the maximum shear,  $\tau_{\text{max}}$ , might also be scaled with  $h^* \text{Re}_{\text{in}}$ . With this new insight in mind, the dimensionless function is even simpler:

$$\tilde{W} = \Phi(\tilde{\tau}, h^* \text{Re}_{\text{in}}) \quad (\text{A.28})$$